

1       **Subduction initiation and back-arc opening north of Neo-**  
2       **Tethys: Evidence from the Late Cretaceous Torbat-e-**  
3       **Heydarieh ophiolite of NE Iran**

4  
5       **Hadi Shafaii Moghadam<sup>1,2\*</sup>, R.J. Stern<sup>3</sup>, W.L. Griffin<sup>2</sup>, M.Z. Khedr<sup>4</sup>, M.**  
6       **Kirchenbaur<sup>5</sup>, C.J. Ottley<sup>6</sup>, S. Whattam<sup>7</sup>, J.-I. Kimura<sup>8</sup>, G. Ghorbani<sup>1</sup>, S. Gain<sup>2</sup>,**  
7       **S.Y. O'Reilly<sup>2</sup>, A. Tamura<sup>9</sup>**

8  
9       <sup>1</sup>*School of Earth Sciences, Damghan University, Damghan 36716-41167, Iran*

10  
11       <sup>2</sup>*ARC Centre of Excellence for Core to Crust Fluid Systems and GEMOC ARC National*  
12       *Key Centre, Dept. of Earth and Planetary Sciences, Macquarie University, NSW 2109,*  
13       *Australia*

14  
15       <sup>3</sup>*Geosciences Dept. University of Texas at Dallas, Richardson, TX 75083-0688, USA*

16  
17       <sup>4</sup>*Dept. of Geology, Faculty of Science, Kafrelsheikh University, 33516 Kafr Elsheikh,*  
18       *Egypt*

19  
20       <sup>5</sup>*Universitat zu Koln, 50674 Koln, Germany & Steinmann-Institut, Universitat Bonn,*  
21       *Germany*

22  
23       <sup>6</sup>*Department of Earth Sciences, Northern Centre for Isotopic and Elemental Tracing,*  
24       *University of Durham, Durham, DH1 3LE, UK*

25  
26       <sup>7</sup>*Department of Geosciences, King Fahd University of Petroleum and Minerals, Dhahran*  
27       *31261, Saudi Arabia*

28  
29       <sup>8</sup>*Department of Solid Earth Geochemistry, Japan Agency for Marine-Earth Science and*  
30       *Technology (JAMSTEC), Natsushima-Cho 2-15, Yokosuka, 237-0061, Japan*

31  
32       <sup>9</sup>*Department of Earth Sciences, Kanazawa University, Ishikawa 920-1192, Japan*

33  
34  
35       \*Corresponding author: [hadishafaii@yahoo.com](mailto:hadishafaii@yahoo.com)  
36       Tel: +61, 484637418; Fax: +61, 2 98508943

37

38

39

40

41

42 **ABSTRACT**

43       How new subduction zones form is an ongoing scientific question with key  
44 implications for our understanding of how this process influences the behavior of the  
45 overriding plate. Here we focus on the effects of a Late Cretaceous subduction-initiation  
46 (SI) event in Iran and show how SI caused enough extension to open a back-arc basin in  
47 NE Iran. The Late Cretaceous Torbat-e-Heydarieh ophiolite (THO) is well exposed as  
48 part of the Sabzevar-Torbat-e-Heydarieh ophiolite belt. It is dominated by mantle  
49 peridotite, with a thin crustal sequence. The THO mantle sequence consists of  
50 harzburgite, clinopyroxene-harzburgite, plagioclase lherzolite, impregnated lherzolite and  
51 dunite. Spinel in THO mantle peridotites show variable Cr# (10-63), similar to both  
52 abyssal and fore-arc peridotites. The igneous rocks (gabbros and dikes intruding mantle  
53 peridotite, pillowed and massive lavas, amphibole gabbros, plagiogranites and associated  
54 diorites and diabase dikes) display rare earth element patterns similar to MORB, arc  
55 tholeiite and back-arc basin basalt. Zircons from six samples, including plagiogranites  
56 and dikes within mantle peridotite, yield U-Pb ages of *ca* 99-92 Ma, indicating that the  
57 THO formed during the Late Cretaceous and was magmatically active for ~7 Myr. THO  
58 igneous rocks have variable  $\epsilon\text{Nd}(t)$  of +5.7 to +8.2 and  $\epsilon\text{Hf}(t)$  ranging from +14.9 to  
59 +21.5; zircons have  $\epsilon\text{Hf}(t)$  of +8.1 to +18.5. These isotopic compositions indicate that the  
60 THO rocks were derived from an isotopically depleted mantle source similar to that of  
61 the Indian Ocean, which was slightly affected by the recycling of subducted sediments.  
62 We conclude that the THO and other Sabzevar-Torbat-e-Heydarieh ophiolites formed in  
63 a back-arc basin well to the north of the Late Cretaceous fore-arc, now represented by the  
64 Zagros ophiolites, testifying that a broad region of Iran was affected by upper-plate

65 extension accompanying Late Cretaceous subduction initiation.

66

67 **KEYWORDS:** Hf-Nd isotopes, U-Pb geochronology, back-arc basin, ophiolite, Iran.

68

## 69 INTRODUCTION

70 Ophiolites are fragments of upper mantle and oceanic crust ([Coleman, 1977](#); [Nicolas,](#)

71 [1989](#)) and are often tectonically incorporated into continental margins during continent-

72 continent and arc-continent collisions ([Dilek and Flower, 2003](#)), ridge-trench interactions

73 ([Lagabrielle et al., 2000](#)), and/or subduction-accretion events ([Cawood, 1989](#)). Ophiolites

74 and their dismembered equivalents are especially common in suture zones in both

75 collisional and accretionary orogens of Neoproterozoic and Phanerozoic age (e.g.,

76 [Furnes et al., 2014](#); [Hébert et al., 2012](#); [Saccani et al., 2013](#)). ([Dilek and Furnes, 2011](#))

77 classified ophiolites into continental margin-, mid-ocean-ridge (MOR)-, plume-, supra-

78 subduction zone-, volcanic arc- and accretionary- types according to their tectonic

79 settings. Evidence is growing that many ophiolites form during subduction initiation in a

80 fore-arc setting ([Whattam and Stern, 2011](#)), and this concept is useful for understanding

81 the Late Cretaceous ophiolites of the Zagros mountains in Iran ([Moghadam and Stern,](#)

82 [2011](#); [Moghadam et al., 2010](#)).

83 The emplacement of an ophiolite on continental crust can occur via various

84 mechanisms, including obduction, subduction and then exhumation of oceanic

85 lithosphere or even through trapping and compression of oceanic basins between two

86 neighboring continental blocks, as is the case for NE Iran ophiolites. Despite the fact that

87 it is geodynamically difficult to emplace ophiolites that form anywhere other than the

88 fore-arc ([Stern, 2002](#)), ophiolites are known to form in other extensional settings such as  
89 marginal basins or back-arc basins. Back-arc basins need strong extension to open and  
90 this can be achieved as a result of subduction initiation (SI). Back arc extension is not as  
91 easily accomplished if regional compression causes induced SI but is expected to  
92 accompany spontaneous SI, due to the large lateral density contrasts across the  
93 lithospheric weakness separating the pertinent plates ([Stern, 2004](#); [Stern and Gerya,](#)  
94 [2017](#)). Spontaneous SI, (i.e., when oceanic lithosphere begins to sink vertically before  
95 down-dip motion is established), will cause extension in the overlying plate, and this can  
96 open a back-arc basin. How subduction initiation causes extension in the overlying plate  
97 also depends on plate configuration and relative motions, thickness of the subducting  
98 oceanic slab, and whether SI is spontaneous or induced.

99 *Marginal basin* is a general term for basins of unknown origin associated with  
100 continental margins and island arcs. Back-arc basins are a type of marginal basin that  
101 open at a convergent plate margin behind an active magmatic arc. Most back-arc basins  
102 are associated with oceanic arcs, although rifting of continental lithosphere also produces  
103 back-arc basins (i.e. ensialic back-arc basins) ([Gerya, 2011](#); [Stern, 2002](#)). Back-arc  
104 ophiolites are represented by MORB-like, BABB-like and calc-alkaline type intrusions  
105 and lavas, generated by partial melting of a MORB-type mantle source (through mantle  
106 wedge flow; e.g., ([Long and Wirth, 2013](#))) into the sub-arc mantle wedge ([Saccani et al.,](#)  
107 [2008](#)). In many cases, the tectonic setting of ophiolites is obscured by alteration and  
108 deformation, so that workers rely heavily on relict mineralogy and immobile trace  
109 element geochemistry to resolve the original tectonic setting. This approach is  
110 problematic because BAB and fore-arc ophiolites share many geochemical and

111 petrographic features and can be difficult to distinguish solely on a basis of petrology and  
112 geochemistry; other considerations are required to distinguish back-arc and fore-arc  
113 ophiolites. This report addresses this problem by focusing on a well-preserved ophiolite  
114 belt in NE Iran that clearly formed in a back-arc basin distal to coeval ophiolites that  
115 formed in a fore-arc, subduction-initiation (SI) setting. Our research supports results from  
116 recent IODP drilling in the Philippine Sea indicating that extensional magmatism related  
117 to subduction initiation can affect much larger regions than just the immediate fore-arc  
118 environment ([Hickey-Vargas et al., 2018](#)).

119       The Sabzevar-Torbat-e-Heydariyeh ophiolites (= STHO) are excellent examples of  
120 Late Cretaceous ophiolites of Iran. The STHO is exposed over a large area of NE Iran,  
121 approximately 130 x 400 km (Fig. 1). From a regional-tectonic perspective, the STHO is  
122 situated in a back-arc setting, separated by ~600km from the Zagros fore-arc ophiolites  
123 ([Moghadam and Stern, 2011](#); [Monsef et al., 2018](#)), the Urumieh-Dokhtar Magmatic Belt  
124 (UDMB) and continental crust of the Lut block (Fig. 2). The faulted contact between the  
125 southernmost STHO ophiolites and Ediacaran-Cambrian (Cadomian) basement to the  
126 south is exposed on the southern margin of the STHO (Fig. 3). Cadomian basement  
127 comprises granitoids, gabbros, rhyolites and pyroclastic rocks with ages of 531-553 Ma  
128 ([Moghadam et al., 2017b](#)). There is no suture to which STHO ophiolites are clearly  
129 related, which probably were exhumed during latest Cretaceous-Paleogene formation of  
130 the Oryan Basin (Fig. 3). This is also confirmed by low-temperature thermo-  
131 chronometric and structural evidence, which show that uplift of the ophiolite domain was  
132 accompanied by dextral transpression beginning in early Paleocene (~60 Ma) and ended  
133 in the Miocene-Pliocene (5 Ma) ([Tadayon et al., 2018](#)). This conclusion is supported by

134 the presence of an early Paleocene unconformity and deposition of middle Paleocene  
135 conglomerates which seal the STHO ophiolites. These conglomerates were produced by  
136 the erosion of the exhuming ophiolites during dextral transpression ([Tadayon et al.,](#)  
137 [2018](#)).

138 The modern episode of subduction of the Zagros orogen subducted Neotethys and  
139 began at 104-98 Ma, as determined by zircon U-Pb dating of Zagros fore-arc ophiolites  
140 ([Moghadam et al., 2013](#); [Moghadam and Stern, 2015](#)). Late Cretaceous subduction  
141 initiation was accompanied by a major change in the direction and velocity of Arabia-  
142 Eurasia convergence ([Agard et al., 2007](#)). We suggest that Late Cretaceous spontaneous  
143 SI caused the observed change in plate motion; that subsidence of Mesozoic Neotethys  
144 lithosphere commenced along a transform margin adjacent to buoyant Eurasian  
145 lithosphere, causing proto-forearc seafloor spreading and producing the Zagros ophiolites  
146 ([Moghadam and Stern, 2011](#); [Moghadam et al., 2010](#)). Foundering Neotethys oceanic  
147 lithosphere induced extension on the southern margin of Eurasia, producing back-arc  
148 basins, tilting of crustal blocks, uplift and intense erosion of the Iranian plateau, as well  
149 as core complex exhumation in some parts of the Iranian plateau ([Malekpour-Alamdari et](#)  
150 [al., 2017](#); [Moritz et al., 2006](#); [Verdel et al., 2007](#)). For testing the Late Cretaceous SI  
151 model for southern Eurasia, it is essential to understand the significance of the Late  
152 Cretaceous back-arc basins in NE Iran, of which the Sabzevar-Oryan-Cheshmehshir-  
153 Torbat-e-Heydarieh ophiolite is the largest representative (Fig. 3). Besides the suspected  
154 back-arc basins in NE Iran, there are several other Late Cretaceous oceanic basins  
155 (ophiolites) whose opening seems to be related to the Late Cretaceous extension within  
156 the Iranian plateau caused by SI along the Zagros suture zone. These ophiolites include

157 [the Khoys ophiolite](#) in NW Iran (e.g, ([Khalatbari-Jafari et al., 2004](#))) and scattered  
158 [ophiolitic slices](#) along the Talysh-Qare Dagh mountains in NNW Iran (e.g., ([Burtman,](#)  
159 [1994](#); [Omidvar et al., 2018](#))).

160 We present here the results of our study of Late Cretaceous mantle peridotites,  
161 gabbros, lavas and plagiogranites from the Torbat-e-Heydarieh ophiolite. We provide  
162 zircon U-Pb ages for six samples of geochemically-distinct plagiogranites, gabbros and  
163 dikes, and compare these with geochronological data from the Sabzevar ophiolite to the  
164 NW (Fig. 3). Peridotite mineral compositions as well as major, trace and rare-earth  
165 element data and bulk rock Nd-Hf and zircon Hf isotopes for selected samples are used to  
166 constrain the tectonic setting of the different magmatic suites. We show that the mantle  
167 rocks and magmatic rocks were generated during back-arc basin extension and use these  
168 results and their magmatic-stratigraphic associations suggest that magmatism occurred in  
169 response to SW-directed rollback of a NE-dipping subduction zone during SI (Fig. 2).

## 170 **GEOLOGICAL SETTING**

171 The STHO is bordered to the north by the major Sangbast-Shandiz strike-slip fault  
172 delimiting the Binalud Mountains (Fig. 1). To the south, the STHO is bounded by the  
173 major Great Kavir-Dorouneh sinistral strike-slip fault (Figs. 1 & 3). The STHO  
174 comprises four main regions where ophiolites crop out (Fig. 3), separated by the  
175 Paleocene-Eocene Oryan sedimentary basin: (1) NNW of Sabzevar (the Sabzevar  
176 ophiolite, studied by ([Moghadam et al., 2014b](#); [Moghadam et al., 2015](#); [Nasrabady et al.,](#)  
177 [2011](#); [Omran et al., 2013](#); [Rossetti et al., 2014](#); [Rossetti et al., 2010](#); [Shojaat et al.,](#)  
178 [2003](#))); (2) SSW of Sabzevar (Oryan ophiolite, no published data); (3) Cheshmehshir in

179 the far south ([Maghfouri et al., 2016](#)), and (4) north of Torbat-e-Heydarieh, the focus of  
180 this study.

181 The STHO lies between the Lut block in the south and the Kopeh-Dagh (Turan  
182 platform ([Thomas et al., 1999](#)) in the north. The STHO formed during the Late  
183 Cretaceous ([Moghadam and Stern, 2015](#)) and contains a well-preserved mantle sequence,  
184 but some parts are fragmented and sheared. There is consensus that the STHO formed  
185 above a subduction zone (-SSZ) setting, as most Sabzevar ophiolite lavas show  
186 appropriate geochemical signatures ([Ghazi et al., 1997](#); [Moghadam et al., 2014a](#); [Shojaat  
187 et al., 2003](#)). Sabzevar mantle peridotites have spinels with both MORB-like (Cr#<50%)  
188 and SSZ-type (Cr#>50%) signatures but most peridotite spinels have high Cr# (>50) with  
189 low TiO<sub>2</sub> and resemble those of SSZ peridotites ([Moghadam et al., 2014a](#)). Some  
190 Sabzevar ophiolite pillow lavas have OIB-like whole-rock compositions, suggesting a  
191 plume or subcontinental lithospheric mantle source. The Sabzevar ophiolite is covered by  
192 Late Campanian to Early Maastrichtian (~75-68 Ma) pelagic sediments. Sabzevar  
193 plagiogranites yield zircon U-Pb ages of 99.9-77.8 Ma ([Moghadam et al., 2014a](#)).  
194 Magmatic rocks of the Sabzevar ophiolite have positive εNd (t) values (+5.4 to +8.3) and  
195 most have high <sup>207</sup>Pb/<sup>204</sup>Pb, indicating a significant contribution of subducted sediments  
196 to their mantle source ([Moghadam et al., 2014a](#)).

197 The Torbat-e-Heydarieh ophiolite (THO) constitutes the southeasternmost of the four  
198 STHO outcrops, covering an area 60 km long and 50 km wide (Fig. 4). The THO shows  
199 no contact with older rocks and is unconformably overlain by Paleocene-Eocene  
200 conglomerates and sandstones. The THO is mostly composed of mantle peridotites  
201 including lherzolites, impregnated lherzolites, minor harzburgites and discordant dunites

202 and chromitite lenses (Figs. 5, 6A). Harzburgites with 2-3 modal% clinopyroxene and  
203 plagioclase-lherzolites are also common. Dunites also occur as small veins and  
204 pods/lenses within the harzburgite. Diabasic-gabbroic-pyroxenitic dikes crosscut the  
205 mantle sequence and in most cases are boudinaged (Fig. 5). Diabasic-gabbroic dikes are  
206 locally converted into rodingite (Fig. 6B). Some diabasic dikes are metamorphosed to  
207 greenschist or lower amphibolite facies. Small intrusions of cumulate and fine-grained  
208 isotropic gabbro and pyroxenite (Figs. 6C, D) are common in harzburgites and  
209 lherzolites; pyroxene-rich gabbroic dikes are also common within these gabbros.  
210 Cumulate gabbroic lenses occasionally are layered, characterized by plagioclase-rich  
211 (anorthosite) and Opx- and Cpx-rich (olivine-bearing) bands (olivine-bearing  
212 melanocratic gabbros) (Fig. 6D). The gabbroic sequence is crosscut by diabasic and  
213 microgabbroic to more-evolved plagiogranitic dikes or small pockets (Fig. 6E). Some  
214 dikes within the gabbros also intrude the underlying peridotites. In some cases, angular  
215 gabbroic xenoliths are found within the plagiogranitic pockets (agmatite, Fig. 6F). Late  
216 plagiogranitic dikes were injected into both gabbros and underlying peridotites.

217 The THO crustal sequence is more poorly exposed than the mantle section but  
218 includes massive and pillow lavas (Fig. 6G), isotropic and coarse-grained massive  
219 gabbros and plagiogranite lenses/dikes within the gabbros (Fig. 5). The contact between  
220 the mantle sequence and crustal rocks in most cases is tectonized, but in some cases the  
221 mantle rocks are overlain by cumulate gabbros or by crustal lavas and pelagic limestones.  
222 The presence of pelagic limestone on top of the mantle section suggests that Late  
223 Cretaceous extension on the seafloor was locally amagmatic. Crustal gabbros differ from  
224 mantle gabbros by containing more diabasic dikes and large plagiogranitic lenses, but

225 plagiogranitic dikes are also common. Lava flows are slightly metamorphosed to  
226 greenschist or lower amphibolite facies. Other rocks from both crustal and mantle  
227 sequences show no trace of metamorphism, but instead they show slight to moderate  
228 alteration. High-temperature alteration of mantle dikes into rodingite is also common.  
229 Pillow lavas show pyrite-chalcopyrite mineralization. Massive and pillow lavas are  
230 occasionally tectonically interlayered with peridotites. There is no obvious geochemical  
231 difference between most pillow and massive lavas (see next section). Late Cretaceous  
232 (Cenomanian to Turonian, ~ 99-90 Ma) pelagic sediments and pyroclastic rocks are  
233 interlayered with and conformably cover the lavas (Figs. 6H, I). Cold breccia including  
234 basaltic fragments set in a pelagic limestone matrix is abundant. THO melanges include  
235 serpentinites, lavas and pelagic sediments. These melanges are especially abundant in the  
236 Sabzevar ophiolites, where various ophiolitic units, Paleocene-Eocene magmatic rocks  
237 and shallow-water limestones are dispersed with serpentinites, showing that these  
238 melanges are related to Eocene or younger deformation ([Moghadam et al., 2014a](#)).

239

## 240 **PETROGRAPHY**

241 Lherzolites are the predominant THO mantle rocks; they contain serpentized  
242 olivine, orthopyroxene and large clinopyroxenes (Fig. 7A). Nearly all lherzolite samples  
243 are moderately (20-30%) serpentized. Vermicular brown spinel is abundant and  
244 generally intergrown with clinopyroxene. Harzburgites are minor and contain  
245 serpentized olivine and orthopyroxene porphyroclasts with fine-grained clinopyroxene  
246 (2-3 %, Fig. 7C) and deep brown spinel. Serpentinization of harzburgites (50-60%) is  
247 greater than in lherzolites (20-30 %). The content of clinopyroxene is higher in Cpx-

248 harzburgites (3-5 %). Here, fine clinopyroxenes occur in embayments of orthopyroxene  
249 porphyroclasts (Fig. 7B), associated with vermicular spinels (Fig. 8A). Part of the THO  
250 mantle section was impregnated with a percolating basaltic melt which filtered through  
251 peridotites, crystallizing plagioclase and clinopyroxene. Impregnated lherzolites have  
252 more coarse-grained clinopyroxene aggregates and lighter-brown spinel compared to  
253 normal lherzolites (Fig. 7C). Plagioclase lherzolites show traces of altered plagioclase (5-  
254 7 modal %) along with melt-impregnated clinopyroxenes (up to 20-30 %) and light  
255 brown vermicular spinel. Large clinopyroxenes enclose plagioclase and brown spinels  
256 (Figs. 6D and 7B). Plagioclase also occurs at the contact of orthopyroxene with  
257 impregnated clinopyroxenes (Fig. 8C). Blebs of sulfide minerals are also observed.  
258 Clinopyroxene accumulation in plagioclase lherzolites makes these rocks similar to  
259 olivine websterites (Fig. 9A). Plagioclase lherzolites show melt-assisted crystallization of  
260 new olivine grains in plagioclase and clinopyroxene embayments (Fig. 8C). Dunites are  
261 altered (50-70 % serpentinization) with mesh-textured olivines (>90%) and coarse-  
262 grained black spinel. Spinels contain abundant inclusions of serpentinized olivine,  
263 clinopyroxene and amphibole (Fig. 8D). Amphibole inclusions are altered to chlorite.

264 Gabbroic lenses within peridotites vary from gabbro (~1-2 % Opx) to gabbronorite  
265 (10-30 % Opx, Fig. 9B). Cumulate gabbros are heterogeneous, with dark bands rich in  
266 clinopyroxene, orthopyroxene and minor plagioclase and whitish bands rich in  
267 plagioclase with minor clinopyroxene. Olivine is rare, whereas coarse-grained, subhedral  
268 orthopyroxene and anhedral clinopyroxene are the main components of cumulate gabbros  
269 (Fig. 7E, F). Plagioclase is interstitial between pyroxene crystals (Fig. 8E, F). Fine-  
270 grained, isotropic gabbros containing plagioclase, orthopyroxene and clinopyroxene are

271 also common in the mantle sequence, closely associated with cumulate gabbros.  
272 Occasional primary brown amphiboles also occur as interstitial laths between other  
273 minerals. Rodingitized dikes contain fine-grained hydrogrossular, rare diopside and  
274 wollastonite as well as pectolite.

275 Coarse-grained crustal plutonic rocks contain plagioclase and amphibole in diorites  
276 and clinopyroxene and plagioclase in gabbros. Some gabbros contain interstitial  
277 amphibole. Plagiogranites have granular texture and are dominated by plagioclase, quartz  
278 and amphibole with secondary epidote, chlorite, sericite, iron oxide and titanite. Apatite  
279 and zircon are minor components. Plagiogranites can be petrographically divided into  
280 tonalites and diorites with more amphibole. Granophyric intergrowths of plagioclase and  
281 quartz are also common in these rocks.

282 Diabasic dikes are fine-grained and contain magnesio-hornblende and sodic  
283 plagioclase. Pillow lavas contain clinopyroxene microphenocrysts, plagioclase microlites  
284 and palagonitized glass. Fine-grained clinopyroxene is also common in the groundmass.  
285 Calcite, chalcedony, titanite, sericite, epidote, prehnite and chlorite are secondary phases.

286 Pillow lavas display hyaloporphyritic to intersertal texture with clinopyroxene and  
287 plagioclase micro-phenocrysts. Massive lavas are similar to pillow lavas but are less  
288 altered. The glassy groundmass of some massive lavas is altered into chlorite and clay,  
289 but most are holocrystalline without glass.

290 **ANALYTICAL METHODS**

291 We used six main analytical procedures to study THO rocks: 1) JEOL wavelength  
292 dispersive electron probe X-ray micro-analyzer (JXA 8800R) to determine the  
293 composition of minerals; 2) Inductively Coupled Plasma-Atomic Emission (ICP-AES)  
294 and Inductively Coupled Plasma-Mass Spectrometry (ICP-MS) to determine whole-rock  
295 contents of major- and trace elements; 3) Cathodoluminescence (CL) imaging of zircons;  
296 4) Sensitive High Resolution Ion Microprobe (SHRIMP) analyses to determine zircon U-  
297 Pb ages; 5) Laser Ablation Inductively Coupled Plasma-Mass Spectrometry (LA-ICPMS)  
298 analyses to determine zircon U-Pb ages and to analyze the trace-element compositions of  
299 clinopyroxene and orthopyroxene from mantle peridotites and gabbros; 6) Multi  
300 Collector-Inductively Coupled Plasma-Mass Spectrometry (MC-ICPMS) equipped with  
301 LA for *in situ* analysis of zircon Hf isotopic compositions. The same MC-ICPMS was  
302 used to analyze the isotopic compositions of Nd and Hf in whole-rock samples.  
303 We studied ~100 samples for petrography, 13 polished thin sections for electron  
304 microprobe analysis, 39 for whole-rock major- and trace-element compositions, 6 for U-  
305 Pb zircon ages, 8 for whole-rock Nd and Hf analyses, 6 for *in situ* mineral trace elements  
306 and 6 for *in situ* Lu-Hf isotope analyses of zircons. The Nd and Hf isotopic compositions  
307 discussed below are corrected for 100 Ma of radiogenic ingrowth. The details of each  
308 technique are given in Electronic Appendix A.

309

## 310 **WHOLE ROCK GEOCHEMISTRY**

311 Three mantle peridotites, fourteen mantle gabbros, ten pillowed and massive lavas,  
312 four amphibole gabbros, two mantle-intruding dikes, and six plagiogranites and  
313 associated diorites and diabase dikes samples were selected for whole rock analysis.

314 Sample locations are shown on Fig. 4. The analyzed samples are characterized by  
315 variable loss on ignition; 0.6-4.2 wt % for crustal rocks, 5.9-11.7 wt % for peridotites and  
316 0.6-5.8 wt % for mantle gabbros. Because of the mobility of some major- and trace  
317 elements during alteration, emphasis is placed on immobile trace elements such as the  
318 REE and high field strength elements (HFSE) to evaluate the original composition and  
319 tectono-magmatic setting of Torbat-e-Heydarieh magmatic rocks. Fluid-mobile elements  
320 such as Cs, Rb, U, Pb, and Sr may be discussed but are generally de-emphasized in the  
321 following sections. Similarly, to avoid the effects of alteration and seawater exchange on  
322 isotopic composition of the rocks, alteration-resistant Nd and Hf isotopes are reported.

323

#### 324 **Mantle Units**

325 Harzburgite has low contents of CaO and Al<sub>2</sub>O<sub>3</sub> (~1.6 wt %), whereas Cpx-  
326 harzburgite and plagioclase lherzolite contain more CaO (~2.3 and ~8.9 wt %  
327 respectively) and Al<sub>2</sub>O<sub>3</sub> (~2.3 and ~5.1 wt % respectively) (Supplementary Table 1).  
328 Harzburgites show highly depleted REE patterns, with steep slopes from LREEs to  
329 MREEs (Fig. 10A). REE abundances are higher in Cpx-harzburgite and plagioclase  
330 lherzolite with nearly flat patterns from MREEs to HREEs, but with steep slope from  
331 LREEs to MREEs. These patterns are similar to those of the cumulate gabbros (Fig.  
332 10A). Enrichment in MREEs to HREEs for Cpx-harzburgite and plagioclase lherzolite is  
333 consistent with the formation of Cpx by metasomatism. Enrichment in fluid-mobile  
334 elements such as U, Rb, Ba, Sr, and Pb relative to LREEs is characteristic of THO mantle  
335 peridotites.

336 Mantle gabbroic rocks have variable contents of SiO<sub>2</sub> (~45-54 wt %), Al<sub>2</sub>O<sub>3</sub> (~10-22

337 wt %), MgO (~4-16 wt %), and CaO (~10-20 wt %), reflecting different extents of  
338 fractionation and/or modal contents of olivine, orthopyroxene, clinopyroxene, and  
339 plagioclase. Gabbroic rocks are Ti-poor, with ~0.06-0.9 wt % TiO<sub>2</sub>; a microgabbro dike  
340 within the gabbro cumulate contains more TiO<sub>2</sub> (0.9 wt %). Isotropic gabbros show an  
341 IAT signature in the Ti vs V diagram ([Shervais, 1982](#)) (Fig. 11B). Gabbroic rocks show  
342 three distinct patterns of rare earths and other trace elements (Fig. 10A and B). Cumulate  
343 gabbros have low REE concentrations compared to fine-grained isotropic gabbros and the  
344 microgabbro dike. Cumulate gabbros are highly depleted in LREE ( $La_{(n)}/Yb_{(n)} = 0.04-$   
345  $0.23$ ) but with nearly flat REE patterns from HREE to MREE ( $Gd_{(n)}/Yb_{(n)} = 0.7-1.2$ ). Eu  
346 enrichment is also noticeable. Extreme depletion in Nb, Ta and Zr (e.g.,  $Nb_{(n)}/La_{(n)} =$   
347  $0.05-0.2$ ) and enrichment in U, Pb, Ba and Sr (e.g.,  $Sr_{(n)}/La_{(n)} = 93-338$ ) relative to LREE  
348 is characteristic of these rocks (Fig. 10B).

349 Isotropic gabbros are enriched in bulk REE compared to the cumulate gabbros and  
350 show LREE-depletion to almost flat patterns ( $La_{(n)}/Yb_{(n)} = 0.3-0.7$ ). These rocks are  
351 slightly depleted in Nb and Zr (e.g.,  $Nb_{(n)}/La_{(n)} = 0.3-0.9$ ) and enriched in Sr, Th, and U  
352 (Fig. 10B). The microgabbro dike shows a flat REE pattern ( $La_{(n)}/Yb_{(n)} = 1.2$ ), weak  
353 negative anomalies in Nb-Ta and enrichment in Sr, Th, U, Ba and Rb.

#### 354 **Crustal rocks**

355 The Torbat-e-Heydariieh massive lavas have similar contents of SiO<sub>2</sub> (~47-49 wt%)  
356 and TiO<sub>2</sub> (1.1-1.6 wt %) and Mg# ( $100Mg/Mg+Fe^{+2}$ ) (54-63) (Supplementary Table 4).  
357 Pillow lavas show greater variability, ranging from 49-55 wt % SiO<sub>2</sub>, Mg# values of 33-  
358 60, and TiO<sub>2</sub> contents of 0.4-2.4 wt %. These volcanic rocks exhibit both tholeiitic and

359 calc-alkaline tendencies in the  $\text{FeO}^t/\text{MgO}$  vs  $\text{SiO}_2$  diagram ([Miyashiro, 1974](#)) (Fig. 11A).  
360 In a Ti vs V diagram ([Shervais, 1982](#)), THO volcanic rocks tend to plot in both the  
361 island-arc tholeiitic (IAT) and MORB fields. Sample TH11-39 shows affinity to E-  
362 MORB-type lavas (Fig. 11B).

363 Massive lavas are depleted in LREE relative to HREE ( $\text{La}_{(n)}/\text{Yb}_{(n)}=0.5-0.8$ ) and have  
364 a slight to moderate depletion in Nb ( $\text{Nb}_{(n)}/\text{La}_{(n)}=0.4-0.7$ ). They are not enriched in Ba,  
365 Th and U ( $\text{Th}_{(n)}/\text{La}_{(n)}=0.7-1$ ) relative to N-MORB (Figs. 10 C and D). These  
366 characteristics are similar to back-arc basin basalts or early arc tholeiites ([Peate and](#)  
367 [Pearce, 1998](#)). These lavas differ from Sabzevar calc-alkaline lavas, which are enriched  
368 in LREE, Th, U and extremely depleted in Nb ([Moghadam et al., 2014a](#)).

369 Pillow lavas can show both enrichment and depletion in LREE relative to HREE  
370 ( $\text{La}_{(n)}/\text{Yb}_{(n)}\sim 0.6-2.7$ ) as well as variable Nb-Ta depletion and Th enrichment (e.g.,  
371  $\text{Nb}_{(n)}/\text{La}_{(n)}=0.3-0.8$  and  $\text{Th}_{(n)}/\text{La}_{(n)}=1.2-4.3$ ) relative to N-MORB (Fig. 10 C and D). They  
372 are geochemically similar to E-MORB and depleted tholeiitic lavas. There is no clear  
373 relationship between these two types of pillow lavas in the field.

#### 374 **Plagiogranites and their host rocks**

375 Plagiogranites and their host rocks (diorites and diabasic dikes) have variable  $\text{SiO}_2$   
376 (71-79 wt % for plagiogranites and 56-58 wt %  $\text{SiO}_2$  for host rocks) and  $\text{TiO}_2$  (0.2-0.5 wt  
377 %) contents (Supplementary Table 4). Plagiogranites and their host rocks have LREE-  
378 enriched and flat REE patterns respectively ( $\text{La}_{(n)}/\text{Yb}_{(n)}=0.8-3.7$ ) with depleted Nb and Ta  
379 contents ( $\text{Nb}_{(n)}/\text{La}_{(n)}=0.3-0.9$ ) accompanied by Ba, U, K, and Th enrichment  
380 ( $\text{Th}_{(n)}/\text{La}_{(n)}\sim 2-9$ ) relative to N-MORB (Fig. 10F). Plagiogranites also show strong positive  
381 anomalies in Sr and sometimes in Eu. These geochemical features are similar to Sabzevar

382 plagiogranites ([Moghadam et al., 2014a](#)) and felsic igneous rocks of convergent plate  
383 margins ([Pearce et al., 1984](#)). These geochemical signatures are also similar to the  
384 geochemical characteristics of plagiogranites from other Tethyan ophiolites of the eastern  
385 Mediterranean realm (e.g., ([Anenburg et al., 2015](#); [Bonev and Stampfli, 2009](#); [Dilek and](#)  
386 [Thy, 2006](#); [Osozawa et al., 2012](#); [Uner et al., 2014](#)).

### 387 **Mantle dikes**

388 Diabasic and dioritic dikes injected into mantle peridotites have  $\text{SiO}_2 \sim 50\text{-}57$  wt %,  
389 with Mg# ranging between 43 and 82 (Supplementary Table 4). Their  $\text{TiO}_2$  contents are  
390 low, ranging from 0.1-1.2 wt %. In the  $\text{FeO}^{\text{I}}/\text{MgO}$  vs  $\text{SiO}_2$  diagram, the dikes are broadly  
391 calc-alkaline, excluding sample TH11-19 (Fig. 11A). In a Ti vs V diagram ([Shervais,](#)  
392 [1982](#)), these rocks plot in the IAT field (Fig. 11B). Diabasic dikes are characterized by  
393 flat REE patterns ( $\text{La}_{(n)}/\text{Yb}_{(n)}=1.1\text{-}1.8$ ), depletions in Nb and Ta ( $\text{Nb}_{(n)}/\text{La}_{(n)}=0.3\text{-}0.5$ ) and  
394 Ba, U, Sr, and Th enrichment ( $\text{Th}_{(n)}/\text{La}_{(n)}=2.6\text{-}3.2$ ), resembling island arc tholeiites (IAT).  
395 Amphibole gabbros are characterized by an IAT signature in the Ti vs V diagram (Fig.  
396 11B). They show LREE-enriched concave-upward patterns ( $\text{La}_{(n)}/\text{Yb}_{(n)} \sim 2\text{-}10$ ) and  
397 depletion in Nb and Ta ( $\text{Nb}_{(n)}/\text{La}_{(n)} \sim 0.4\text{-}0.6$ ).

398

### 399 **MINERAL COMPOSITION**

400 Major element compositions of the main rock-forming minerals were determined in  
401 mantle peridotites and cumulate gabbroic rocks: olivine, spinel, orthopyroxene,  
402 clinopyroxene, plagioclase and amphibole. Trace element contents of clinopyroxenes are  
403 also presented. These results are discussed below.

### 404 **Olivine**

405 Olivine in dunite has forsterite contents ranging from 92.8% to 93.1% ( $\text{Fo}_{92.8-93.1}$ )  
406 with high NiO content (~0.3-0.4 wt %) (Supplementary Table 1), typical for mantle  
407 olivine. Olivine in the harzburgites and Cpx-harzburgites is slightly less magnesian (but  
408 still mantle-like) with Mg# and NiO between 91.4-91.9 ( $\text{Fo}_{91.4-91.9}$ ) and 0.34-0.43 wt %  
409 respectively. Lherzolites and impregnated lherzolites are characterized by olivine Mg#  
410 and NiO content of 89.5-91.3 ( $\text{Fo}_{89.5-91.3}$ ) and 0.34-0.52 wt% respectively, also mantle-  
411 like. Olivine in plagioclase lherzolites has lower Fo and NiO contents ( $\text{Fo}_{84.8-85.6}$  and 0.18-  
412 0.24 wt %) than commonly are found in mantle peridotite. These olivines have a  
413 magmatic composition (compared to high Mg# mantle olivines) and are interpreted to  
414 have crystallized from impregnating mafic melts.

#### 415 **Spinel**

416 Peridotite spinels show variable Cr# ( $100\text{Cr}/(\text{Cr}+\text{Al})$ ; 10-63), similar to those in  
417 abyssal, back-arc basin, and fore-arc peridotites ([Dick and Bullen, 1984](#)) (Fig. 12). Spinel  
418 from dunites has higher Cr# (59-63) and  $\text{TiO}_2$  contents (0.18-0.25 wt %) and follows the  
419 peridotite-boninitic melt interaction trend of ([Pearce et al., 2000a](#)) (Figs. 12A and B).  
420 Spinel from harzburgites and Cpx-harzburgites have variable contents of  $\text{TiO}_2$  (0.03-  
421 0.07 wt % in harzburgites and 0.1 to ~0.3 in Cpx-harzburgites) and FeO (~12.2-12.8 wt  
422 % in harzburgites and 14.2-15.5 wt % in Cpx-harzburgites). Harzburgite spinels have  
423 lower Cr# (22-24) than Cpx-harzburgite spinels (24-36).

424 Spinel of lherzolites and impregnated lherzolites have variable contents of  $\text{TiO}_2$   
425 (0.02-0.12 wt %) and Cr# (10-20). Spinel compositions of lherzolites and impregnated  
426 lherzolites overlap at low Cr#. This is because these two rocks have same mineral

427 assemblages; impregnated lherzolites have more coarse-grained clinopyroxene  
428 aggregates with the lightest brown spinels. The Cr# of their spinels is similar to that of  
429 abyssal peridotites ([Dick and Bullen, 1984](#)). Spinels from plagioclase lherzolites have  
430 high TiO<sub>2</sub> (0.15-0.25 wt%) and FeO (~31-39 wt%) content and high Cr# (41-48).

#### 431 **Orthopyroxene**

432 Orthopyroxene in harzburgite and Cpx-harzburgite has Mg# (91-92) and elevated  
433 contents of Al<sub>2</sub>O<sub>3</sub> (2.7-5 wt %) and Cr<sub>2</sub>O<sub>3</sub> (0.56-1 wt %) (Supplementary Table 1).  
434 Orthopyroxene in lherzolites and impregnated lherzolites has constant Mg# (89-91) but  
435 variable Al<sub>2</sub>O<sub>3</sub> (~3-6.1 wt %) content. Plagioclase-lherzolite orthopyroxenes have low  
436 Mg# (86) and Al<sub>2</sub>O<sub>3</sub> (2.1-2.3 wt %) compared to orthopyroxene from other THO  
437 peridotites. Orthopyroxene in gabbros has lower Mg# (79-84) and Al<sub>2</sub>O<sub>3</sub> contents (1.5-  
438 2.1 wt %). The Al<sub>2</sub>O<sub>3</sub> content of the THO peridotite orthopyroxenes are relatively high,  
439 ranging from 1.5-6.1 wt %; the higher values are encountered in impregnated lherzolites.  
440 However, the Al<sub>2</sub>O<sub>3</sub> content of orthopyroxene from fertile spinel peridotites from  
441 ophiolites in other worldwide localities (e.g., the Vardar ophiolite, ([Bazylev et al., 2009](#))  
442 and fertile peridotites from the Yarlung Zangbo suture zone, ([Bedard et al., 2009](#))) and  
443 oceanic back-arcs (e.g., Mariana Trough, ([Ohara et al., 2002](#)) and South Sandwich arc-  
444 basin, ([Pearce et al., 2000b](#))) are also high, resembling the THO impregnated lherzolites,  
445 and show the fertile nature of the host mantle rocks.

#### 446 **Clinopyroxene**

447 Clinopyroxene is abundant in dunite as inclusions in large chromites. Its composition  
448 is W<sub>0.49-0.51</sub>En<sub>47-49</sub>Fs<sub>2-3</sub>. It has high Mg# (94-97) and low TiO<sub>2</sub> (0.06-0.19 wt. %) and Al<sub>2</sub>O<sub>3</sub>

449 (0.6~2 wt. %). Harzburgites and Cpx-harzburgites contain clinopyroxene with  $W_{044-}$   
 450  $_{52}En_{48-49}Fs_{3-4}$ . Clinopyroxene in Cpx-harzburgites have higher  $TiO_2$  (0.26-0.35 wt. %),  
 451 but lower  $Al_2O_3$  (3.9-4.6 wt. %) compared to those in harzburgites ( $TiO_2=0.12-0.17$  wt.  
 452 %;  $Al_2O_3=3-5.2$  wt. %) (Fig. 12C) with identical Mg# (92-94). Clinopyroxene in mantle  
 453 lherzolites and impregnated lherzolites has variable composition ( $W_{036-51}En_{45-59}Fs_{4-6}$ )  
 454 with high Mg# (91-93),  $Al_2O_3$  (4.9-7.1 wt %) and  $TiO_2$  (0.3-0.5 wt %) (Supplementary  
 455 Table 1). Plagioclase lherzolites have clinopyroxene with more constant composition  
 456 ( $W_{041-48}En_{46-52}Fs_{6-7}$ ) but with low  $TiO_2$  (0.06-0.16 wt %) and  $Al_2O_3$  (2.2-3.8 wt %) and  
 457 lower Mg# (87-89) compared to clinopyroxene from other THO lherzolites. On a  $TiO_2$  vs  
 458 Mg# diagram (Fig. 12C) clinopyroxenes from THO peridotites are similar to those found  
 459 in both abyssal and supra-subduction zone peridotites. Clinopyroxene and spinel from  
 460 nearly all mantle units of Tethyan ophiolites show both abyssal and supra-subduction-  
 461 zone geochemical signatures (e.g., ([Aldanmaz, 2012](#); [Ghazi et al., 2010](#); [Monsef et al.,](#)  
 462 [2010](#))). This geochemical duality can be also observed in the crustal lavas of Neotethyan  
 463 ophiolites (e.g., ([Dilek and Furnes, 2009](#); [Dilek et al., 2007](#); [Sarifakioglu et al., 2009](#))).

464 Clinopyroxene in gabbro has variable composition ( $W_{037-47}En_{45-51}Fs_{7-13}$ ). The more  
 465 evolved compositions (with low Ca but high Fe) are found in smaller crystals between  
 466 large clinopyroxenes. Gabbroic clinopyroxenes have  $TiO_2$  and  $Al_2O_3$  contents from 0.07-  
 467 0.21 and 1.7-2.8 wt % respectively; these are lower than in Sabzevar gabbroic  
 468 clinopyroxenes.

#### 469 **Plagioclase**

470 Plagioclase in plagioclase lherzolites is highly altered; unaltered portions show very  
 471 high An contents (96.2-98.3%). Gabbro plagioclase is also anorthite-rich (~An 91.1-98.2)

472 (Supplementary Table 1); amphibole-bearing gabbros with less orthopyroxene contain  
473 An<sub>91-92</sub> plagioclase. Comparison of the clinopyroxene Mg# against anorthite content in  
474 plagioclase ([Sanfilippo et al., 2013](#)), shows a pattern similar to SSZ-type gabbros (Fig.  
475 12D).

#### 476 **Amphibole**

477 Analyses of amphibole inclusions within dunite chromites, plotted in the Mg# vs Si  
478 diagram (*not shown*), show that these are pargasite to edenite according to ([Leake et al.,](#)  
479 [1997](#)). The Cr<sub>2</sub>O<sub>3</sub> contents of these amphiboles are high (2.4-3.1 wt. %).

480

#### 481 **Clinopyroxene: Trace Element Geochemistry**

482 Trace-element abundances (including REEs) in THO lherzolites, impregnated  
483 lherzolites, plagioclase lherzolites and cumulate gabbros are listed in Supplementary  
484 Table 2.

485 All mantle clinopyroxenes from the Torbat-e-Heydarieh ophiolite are enriched in  
486 REEs with LREE-depleted patterns. They are similar to REE abundances in Cpx from  
487 mid-ocean ridge (MOR) cumulates and abyssal peridotites and are much more enriched  
488 than those in SSZ peridotites (Fig. 13A, C).

489 Chondrite-normalized REE patterns of clinopyroxenes from THO lherzolites are  
490 strongly depleted in light REEs (LREE) but are flat in middle to heavy REEs (MREE-  
491 HREE). These patterns are similar to those of Cpx in oceanic abyssal peridotites ([Bizimis](#)  
492 [et al., 2000](#); [Johnson et al., 1990](#)), although total REE concentrations are greater (Fig.  
493 11A). The REE content of THO lherzolite Cpx is even higher than Cpx from Sabzevar  
494 plagioclase lherzolites (Fig. 13B) ([Shafaii Moghadam et al., 2015](#)). Clinopyroxene trace-

495 element patterns are depleted in Ti and Zr, but not in Sr and Eu (Fig. 13B).  
496 Clinopyroxene in THO impregnated lherzolites exhibits REE patterns similar to Cpx  
497 from THO lherzolites, characterized by higher total REE contents compared to Cpx from  
498 abyssal peridotites and Sabzevar lherzolites (Fig. 13C). Negative anomalies in Ti and Zr  
499 are also obvious (Fig. 13D).

500 Cpx in THO plagioclase lherzolites have REE patterns similar to those of Cpx from  
501 MOR cumulates ([Ross and Elthon, 1993](#)), but with more depleted LREE (La-Sm, Fig.  
502 13C). These patterns are also similar to those for Cpx from Sabzevar Cpx-harzburgites.  
503 MREE-HREE abundances in Cpx of plagioclase lherzolite are depleted compared to Cpx  
504 from THO lherzolites and impregnated lherzolites (Fig. 13C). Slight depletion in Ti and  
505 strong Zr negative anomalies are conspicuous in plagioclase lherzolites (Fig. 13D).

506 The REE abundances and patterns of clinopyroxenes in THO gabbro cumulates are  
507 in the range of those exhibited by MOR cumulates ([Ross and Elthon, 1993](#)) (Fig. 13A),  
508 but with more convex-upward MREEs with Sm-Ho peaks. They are similar to  
509 clinopyroxene patterns from Sabzevar cumulate gabbros but with lower REE abundances  
510 (Fig. 13A). The Cpx from cumulate gabbros are depleted in Zr and Ti but enriched in Sr  
511 (Fig. 13B). Trace element patterns of Cpx in cumulate gabbros are between those from  
512 Cpx of plagioclase and impregnated lherzolites.

513

#### 514 **Nd-Hf Isotopes**

515 Eight samples were selected including depleted tholeiitic pillow lavas, back-arc  
516 basin-type massive lavas, supra-subduction zone-type plagiogranites, IAT-like diabasic  
517 dike and back-arc to fore-arc-type gabbros for analysis of whole-rock Nd and Hf

518 isotopes. Hf-Nd isotope compositions are useful for inferring mantle source  
519 characteristics and the role of sediments and older continental crust in generating  
520 subduction-related magmas ([Vervoort and Blichert-Toft, 1999b](#); [Vervoort et al., 1999](#);  
521 [Woodhead et al., 2012](#); [Yogodzinski et al., 2010](#)).

522 The  $\epsilon_{\text{Nd}}(t)$  and  $\epsilon_{\text{Hf}}(t)$  values for THO rocks vary between +5.7 to +8.2 and +14.9 to  
523 +21.5 respectively; gabbro shows especially high  $\epsilon_{\text{Hf}}(t)$  (+21.5) (Fig. 14A). All the  
524 samples plot near the field for modern Indian Ocean MORBs, suggesting a similar  
525 mantle source ([Chauvel and Blichert-Toft, 2001b](#)). Figure 13B shows the results of bulk-  
526 mixing calculations between mantle-derived MORB melts and various types of sediments  
527 ([Chauvel et al., 2009](#)). Involvement of subducted Fe-Mn rich sediments (as well as  
528 calcareous clays) in the mantle source affects Nd- more than Hf isotopic compositions  
529 (Fig. 14B). In contrast, addition of continental sands will affect Hf as well as Nd isotopic  
530 compositions, depending upon whether bulk assimilation of sediments or sediment melts  
531 are involved. Also, the different Hf/Nd ratios of sediments are expected to have a large  
532 influence, especially with the contribution of zircons in the subducted sediments.

533 In contrast to the Oman plagiogranites, which show strong involvement of sediment  
534 melts in their magmatic reservoir ([Haase et al., 2015](#)), the mantle sources of the Torbat-e-  
535 Heydarieh plagiogranites were not significantly affected by sediment melt addition or  
536 crustal assimilation. However, the mantle source of the Torbat-e-Heydarieh magmatic  
537 rocks could have been slightly affected by subducted pelagic sediments (high Nd/Hf  
538 ratio), because they vary considerably in  $\epsilon_{\text{Nd}}(t)$ . They have less radiogenic Nd- isotope  
539 compositions than the igneous rocks of the Dehshir Late Cretaceous ophiolite (inner belt  
540 Zagros ophiolites, Fig. 1 ([Moghadam et al., 2010](#))). The Nd-isotope compositions of the

541 THO magmatic rocks are similar to those of the Sabzevar ophiolite from NE Iran, which  
542 have high but variable  $\epsilon\text{Nd}(t)$  values (+5.4 to +8.3) and moderately high  $^{207}\text{Pb}/^{204}\text{Pb}$   
543 ratios (15.50-15-65) ([Moghadam et al., 2014a](#)). The Nd-Hf-Pb isotopic compositions of  
544 the Sabzevar-Torbat-e-Heydarieh rocks suggest a minor contribution of subducted  
545 sediments to the mantle source of these ophiolites from NE Iran.

546

#### 547 **ZIRCON GEOCHRONOLOGY**

548 Four plagiogranites and two diabasic and gabbroic mantle-intruding dikes from the  
549 Torbat-e-Heydarieh ophiolite have been dated. We also analyzed five of these zircon  
550 separates for Hf-isotope compositions.

#### 551 **Sample TH11-23**

552 This sample is taken from a plagiogranitic dike injected into the mantle diabasic  
553 dikes. Zircons are euhedral and prismatic and show magmatic concentric zoning (Fig.  
554 15). These zircons contain 215-762 ppm U and have high Th/U ratios of 0.6-1.7  
555 (Supplementary Table 6), consistent with a magmatic origin. Twenty-one analyses define  
556 a mean  $^{206}\text{Pb}/^{238}\text{U}$  age of  $99.32 \pm 0.72$  Ma (MSWD=1.4) (Fig. 15). This is interpreted as  
557 the time of plagiogranite crystallization. Zircons from this sample show a wide range of  
558  $\epsilon\text{Hf}(t)$ , between  $\sim +8$  and +16.1 (Supplementary Table 8).

#### 559 **Sample TH11-12**

560 This sample is taken from a rodingitized gabbroic dike injected into mantle  
561 peridotites. The Th/U ratio of analyzed zircons varies between 0.47-0.69, consistent with  
562 a magmatic origin. Six analyzed grains yield a mean  $^{206}\text{Pb}/^{238}\text{U}$  age of  $96.7 \pm 2.1$  Ma  
563 (MSWD=0.32) (Fig. 15). This is the age of gabbroic dike intrusion and provides a

564 minimum age for the Torbat-e-Heydariieh ophiolite formation. Zircons from this sample  
565 show  $\epsilon_{\text{Hf}}(t)$  values that vary from  $\sim +9$  to  $+16.9$ .

566 **Sample TH11-82B**

567 This plagiogranite intrudes mantle cumulate gabbros. Twenty-five zircons from this  
568 sample were dated by LA-ICPMS. Cathodoluminescence (CL) images show that the  
569 grains are medium-grained ( $<100 \mu\text{m}$ ) and euhedral to subhedral (Fig. 15). Zircons have  
570 low to medium U (25-420 ppm) and Th (10-208 ppm) concentrations, and Th/U ratios  
571 vary between 0.4 and 0.7 (Supplementary Table 7), consistent with a magmatic origin.  
572 The  $^{206}\text{Pb}/^{238}\text{U}$  and  $^{207}\text{Pb}/^{235}\text{U}$  data define a concordia age of  $91.9 \pm 0.33 \text{ Ma}$  (MSWD =  
573 1.7). This is interpreted as the age of plagiogranite crystallization. Zircons from this  
574 sample show  $\epsilon_{\text{Hf}}(t)$  values of  $\sim +9.8$  to  $+15.1$  (Supplementary Table 8).

575 **Sample TH11-74**

576 This plagiogranite intrudes mantle cumulate gabbros. We analyzed fourteen zircons  
577 from this sample. CL images indicate magmatic zonation. Zircons have low to medium U  
578 (53-613 ppm) and Th (26-364 ppm) concentrations, and Th/U ratios vary between 0.5  
579 and 1.3 (Supplementary Table 7). In the concordia diagram, fourteen analyses yield an  
580 age of  $97.0 \pm 1.3$  (MSWD = 0.2) (Fig. 15). Zircons from this sample show  $\epsilon_{\text{Hf}}(t)$  values  
581 that vary from  $\sim +11.3$  to  $+17.6$ .

582 **Sample TH11-29**

583 This sample is a diabasic dike within the mantle peridotites and contained only eight  
584 zircons. Zircons from this sample are prismatic ( $\sim <50 \mu\text{m}$  to  $\sim 100 \mu\text{m}$ ). CL images show  
585 oscillatory zoning in some grains and some are less luminescent with weak zonation.  
586 Eight analyzed spots have high Th/U values (0.3 to 1.6). Five of the analyzed zircons

587 show concordant ages with weighted mean of  $^{206}\text{Pb}/^{238}\text{U}$  age of  $97.1 \pm 1.2$  (MSWD=0.6)  
588 (Fig. 15). The striking feature of this sample is the presence of three xenocrystic zircons  
589 with  $^{207}\text{Pb}/^{235}\text{U}$  ages of ~1.1-1.5 Ga. Late Cretaceous zircons from this sample show  $\epsilon\text{Hf}$   
590 (t) values that vary from ~ +8.1 to +12.7, whereas the old zircons have  $\epsilon\text{Hf}$  (t) values  
591 between +1.7 and +6.2 (Supplementary Table 8).

#### 592 **Sample TH11-20**

593 Zircon grains from this sample, a plagiogranitic dike within the crustal gabbros, are  
594 long-prismatic and euhedral. Most crystals have magmatic zonation. Twenty-five  
595 analyses show low to moderate Th/U (~0.2-0.7) (Supplementary Table 7). Analyses are  
596 concordant, yielding a weighted mean age of  $97.9 \pm 0.6$  Ma (MSWD= 1.4). This is  
597 interpreted as the crystallization age for this dike. Zircons from this sample show  $\epsilon\text{Hf}$  (t)  
598 values that vary from ~ +13 to +18.5.

599

## 600 **DISCUSSION**

601 This new geochemical and isotopic dataset from the Torbat-e-Heydarieh ophiolites  
602 allows a detailed investigation of the mantle characteristics and the source of crustal  
603 rocks; the timing of back-arc basin opening and the relationship of this ophiolite to other  
604 Iranian ophiolites; the tectonic setting in which the Torbat-e-Heydarieh ophiolite formed;  
605 and the implications for understanding Late Cretaceous tectonic evolution in the region.

#### 606 **Sources of mantle peridotites and crustal melts**

607 Mineral- and whole-rock compositions of various mantle peridotites, crustal gabbros,  
608 and effusive lavas classify the rocks into four different tectonic settings: abyssal

609 peridotite, supra-subduction zone fore-arc (FA), island-arc (IA), and back-arc basin  
610 (BAB) settings.

611 ***Mantle peridotites of MOR origin***

612 Lherzolites and impregnated lherzolites show affinities with abyssal (MOR)  
613 peridotites. Compositions of Cr-spinel and co-existing olivine all plot in a confined field  
614 between fertile MORB-source mantle (FMM) and its partial melts (Figs. 9A-B). The  
615 clinopyroxene and spinel compositions of impregnated lherzolites are similar to the  
616 mineral compositions of lherzolites, suggesting these phases precipitated from the same  
617 melts during the impregnation. The overall compositional trends show mixing between a  
618 FMM source and its partial melting residue ( $F = \sim 9\%$ ). The trend may also represent  
619 various degrees of extraction (lherzolite) and addition (impregnated lherzolite) of basaltic  
620 melts (Fig. 10A). Clinopyroxene compositions in these rocks also plot within the  
621 enriched part ( $\text{TiO}_2 > 0.2$  wt. %) of the abyssal-peridotite field (Fig. 10C). Such variations  
622 can form in the fractional to reactive melting regime in the spinel-stability field beneath a  
623 spreading ridge ([Kimura and Sano, 2012](#)), as envisaged by the clinopyroxene REE  
624 patterns with flat MREE to HREE and depleted LREE (Figs. 10A-C).

625 ***Dunite of SSZ fore-arc origin***

626 Spinel in dunite samples are rich in Cr and Ti and their compositions plot close to  
627 the boninite and IAT basalt field (Figs. 9A-B). They plot away from the abyssal  
628 peridotite field, into the SSZ field. Because of the proximity of the compositions of spinel  
629 and clinopyroxene to those of boninite or IAT, these are most like SSZ fore-arc  
630 peridotites.

631 ***Plagioclase lherzolite and cumulate gabbro of SSZ-IA origin***

632 Cumulate gabbros contain low-Mg# clinopyroxene and An-rich (~90) plagioclase.  
633 These are features of assemblages formed from water-rich arc basalt magmas (e.g.,  
634 [Hamada and Fujii, 2008](#)). Therefore, the gabbros are most similar to arc magmas  
635 [\(Ishizuka et al., 2014\)](#).

636 Spinels in plagioclase lherzolites show intermediate abundances of Cr and Ti (Figs.  
637 9A-B). Clinopyroxenes have low Mg# and are poor in Ti, similar to cumulate gabbros.  
638 The low Ti content of clinopyroxenes from plagioclase lherzolites suggest crystallization  
639 from a SSZ-derived melt during magmatic impregnation. The Cr and Ti compositions of  
640 plagioclase lherzolite spinels lie between the fields of abyssal peridotite and basalt (Fig.  
641 10A); however, Mg# in the spinel plots away from abyssal peridotite but close to SSZ-  
642 FA peridotite. Considering the Mg#-rich spinel and Mg-poor clinopyroxene together  
643 (Figs. 9B-C), the plagioclase lherzolites suggest affinities with island-arc tholeiites.

644 The REE patterns of clinopyroxenes from cumulate gabbros show depleted MREE to  
645 HREE relative to MOR gabbros with elevated Sr (Fig. 11B). Plagioclase lherzolites show  
646 the same feature, with more depleted MREE to HREE and elevated Sr (Fig. 11D). Low  
647 REE abundance is the signature of a depleted mantle source and elevated Sr may reflect  
648 addition of metasomatic slab-derived fluid. Sr enrichment in plagioclase-bearing  
649 peridotites is also suggested to postdate melt impregnation and could be the result of  
650 high-temperature (370-850 °C) breakdown of plagioclase, which liberated Sr to enrich  
651 adjacent pyroxenes [\(Pirnia et al., 2014\)](#).

652 The lower abundances of Zr in plagioclase lherzolites relative to lherzolites and  
653 depletion in HFSE in the mantle and gabbro sources are consistent with hydrous

654 metasomatism ([Arai et al., 2006](#); [Khedr and Arai, 2009](#)). This feature is most consistent  
655 with a SSZ-FA origin of the mantle-crust lithologies.

656 ***Harzburgite and Cpx-harzburgite of BAB origin***

657 Spinel in harzburgite have intermediate Mg# (66-76) and partially overlap lherzolite  
658 fields (Figs. 9A-B). In contrast, spinels with lower Ti and higher Cr than those of  
659 lherzolite are more depleted (Figs. 9A-B). Ti contents are low in both clinopyroxenes and  
660 dunite, suggesting a SSZ signature (Fig. 10C). Any further constraints on harzburgite  
661 tectonic affinities are difficult to identify.

662 Cpx-harzburgite forms common geochemical trends with harzburgite. They plot  
663 between abyssal basalt, abyssal peridotite, and SSZ dunite (Figs. 9A-C). The depleted  
664 nature of these rocks implies that harzburgite was impregnated by MORB or IAT melt  
665 (Figs. 9A-C). It is difficult to identify the impregnated melts as either MOR or IA.  
666 However, the harzburgites are distinct from abyssal peridotites suggesting involvement of  
667 strongly depleted mantle ( $F = \sim 12\%$ ; Fig. 9A). Such highly depleted sources can occur in  
668 fore-arc or BAB settings ([Hirahara et al., 2015](#)). We thus conclude that harzburgite and  
669 cpx-harzburgite probably formed in a fore-arc or BAB.

670 No Cpx-REE data are available for the Cpx-harzburgites. Some insight may be  
671 gained by considering harzburgite clinopyroxenes from the nearby Sabzevar ophiolite.  
672 These are extremely depleted (Fig. 11D) consistent with a SSZ mantle origin of the NE  
673 Iran ophiolite harzburgites and impregnated harzburgites.

674 ***Isotropic and cumulate gabbros: back-arc basin or fore-arc origin?***

675 Isotropic gabbros show flat to slightly LREE-depleted patterns with lower total  
676 abundances than N-MORB, along with Nb-Ta troughs and elevated La and Th (Fig.

677 12B). These geochemical features are close to those of FAB from the IBM fore-arc  
678 ([Reagan et al., 2010](#)), although Nb-Ta depletions are greater in THO rocks. One  
679 microgabbroic dike is similar, with more elevated trace element abundances and no Eu  
680 anomaly (Figs. 11A-B). This may represent a melt-rich part of the gabbros. Although  
681 some depleted IA basalts generated during BAB opening show similar trace element  
682 patterns, these are generally richer in Pb, Th, and LREEs (e.g., ([Shinjo et al., 1999](#))).  
683 Similarly, enriched E-type MORB erupted in the Sea of Japan back-arc basin during its  
684 opening at ~17 Ma ([Hirahara et al., 2015](#)). Depleted D-type MORB is also associated  
685 with the opening of the Sea of Japan ([Hirahara et al., 2015](#)). Sea of Japan D-type basalts  
686 are geochemically

687 similar to THO isotropic gabbros, apart from depleted HREE due to residual garnet  
688 in the source of the former basalts ([Hirahara et al., 2015](#)). According to these  
689 considerations, we find that the isotropic gabbros are most similar to FA or BAB.

690 In contrast to the isotropic gabbros, cumulate gabbros show elevated Sr, Pb, Ba, and  
691 Eu anomalies due to plagioclase accumulation. LREE-depleted patterns reflect cumulate  
692 clinopyroxene, but the patterns still show Nb-Ta depletion relative to La and Th. This is  
693 similar to gabbros of FA or BAB origin. The loss of melt from cumulate gabbros and the  
694 concentration of some cumulate minerals could explain the different chemistries of  
695 isotropic and cumulate gabbros (Figs. 11A-B). Plagioclase is anorthite-rich (Fig. 10D),  
696 suggesting that these gabbros most likely originated from water-rich basaltic melts  
697 ([Hamada and Fujii, 2008](#)). All of the above observations indicate that the THO gabbros  
698 are most similar to FA or BAB basalts.

699 It is hard to specify the tectonic setting of the SSZ gabbros from geochemistry alone;  
700 this is consistent with fore-arc, arc, or back-arc basin settings.

701 *Pillow and massive basaltic lavas, dikes within mantle of IA-BAB origin*

702 Most lavas show slightly LREE-depleted flat patterns with slight Nb depletion and  
703 slight Th enrichment. The pattern is akin to N-MORB, FAB, or BABB. These features  
704 are further examined below using Th/Yb and Th/Ce ratios.

705 A useful observation is the lack of boninite in the THO. Fore-arc volcanic sequences  
706 are frequently but not always associated with boninite and high-Mg andesite (([Ishizuka et al., 2014](#);  
707 [Reagan et al., 2010](#)) for IBM; ([Ishikawa et al., 2002](#)) for Oman ophiolite). In  
708 the fore-arc setting, boninites are suggested to be generated 2-4 m.yr. later than fore-arc  
709 basalts, when the residual, highly depleted mantle melted at shallow levels after  
710 interaction with a water-rich fluid derived from the subducting slab ([Ishizuka et al., 2014](#);  
711 [Reagan et al., 2010](#)). However, boninite does not occur in the THO, suggesting that it did  
712 not form in a fore-arc subduction-initiation setting.

713 One pillow-lava sample is enriched in LREE, like E-MORB (Fig. 12D). This sample  
714 is similar to OIB-like pillow and massive lavas from the Sabzevar ophiolite ([Moghadam  
715 et al., 2014a](#)). E-MORB occurs either in MOR or in BAB as an along-ridge geochemical  
716 variation (e.g., ([Kelley et al., 2013](#))). E-MORB also occurred in the SW Japan FA when  
717 subduction re-initiated at 15 Ma ([Kimura et al., 2005](#)). E-MORB occurs all over MOR-  
718 FA-BAB settings, so its presence does not constrain the setting of THO. Melting of  
719 enriched subcontinental lithosphere might be responsible for generating THO E-MORB-  
720 like lavas.

721 Two of the most depleted samples have strong Nb depletions and strong Th  
722 enrichments (Fig. 12D). REEs are more depleted than MORBs, but with elevated LILEs  
723 such as Sr, U, and Ba. These are IAT-like basalts; such basalts occur in BAB and in fore-  
724 arcs.

### 725 *Plagiogranites and amphibole gabbros of IA-BAB origin*

726 Plagiogranites and amphibole gabbros all have arc-magma signatures including Nb-  
727 Ta troughs and strong Th enrichment (Fig. 12F). HREEs are strongly depleted, similar to  
728 IAT-type pillow lavas. LREEs are highly enriched in both lithologies with greater LILE  
729 enrichment in amphibole gabbros. Sample TH11-9B geochemically resembles E-MORBs  
730 with enriched LREEs and less Nb depletion. Elevated Sr and Eu contents in the  
731 plagiogranites are probably due to plagioclase accumulation. Positive Zr-Hf anomalies in  
732 the amphibole gabbros and host rocks of plagiogranites are likely to reflect preferential  
733 partitioning of these elements into amphibole during fractional crystallization ([Tiepolo et](#)  
734 [al., 2007](#)) (Fig. 12F).

### 735 *Nb/Yb - Th/Yb discrimination*

736 ([Pearce, 2008](#)) proposed that Th/Yb vs Nb/Yb relationships could distinguish  
737 MORB-OIB from SSZ igneous rocks. Most THO lavas and crustal gabbros show  
738 elevated Th/Yb at moderate to low Nb/Yb, consistent with subduction contributions  
739 (sediment melt) to a moderately depleted mantle source (Fig. 16A). Exceptions are  
740 TH11-70, TH11-33, TH11-32, TH11-64, TH11-67, TH11-66, which plot along the  
741 MORB-OIB array within the N-MORB field, and TH11-39 pillow lava and TH11-9B  
742 amphibole gabbro, which plot along the MORB-OIB array within the E-MORB field.  
743 Other lavas and gabbros have Nb/Yb similar to N- and E-MORB, but have elevated

744 Th/Yb (Fig. 16A). Pillow and massive lavas, mantle dikes and cumulate gabbros have  
745 low Nb/Yb, whereas amphibole gabbros and plagiogranites show high Nb/Yb indicating  
746 derivation of these magmas from more- and less-depleted mantle sources, respectively  
747 ([Pearce, 2008](#)).

#### 748 *Th/Nb - Ce/Nb discrimination*

749 Similar conclusions are reached based on the Th/Nb - Ce/Nb plot (Fig. 16B)  
750 ([Sandeman et al., 2006](#)). Most lava flows (TH11-70, TH11-33, TH11-32, TH11-64,  
751 TH11-67, TH11-66) and the TH11-9A amphibole gabbro have MORB signatures  
752 whereas TH11-39 pillow lava and TH11-9B amphibole gabbro are similar to Sabzevar  
753 OIB-type lavas. These are in turn similar to Lau Basin BAB and Okinawa Trough intra-  
754 arc rift lavas. In contrast, other IA-BAB-type lavas, isotropic gabbros, amphibole  
755 gabbros, and mantle dikes have lower Ce/Th, plotting close to Okinawa Trough BABs.  
756 Overall, THO magmatic rocks including lavas, gabbros, and plagiogranites plot between  
757 MORB and Mariana arc lavas, and therefore indicate generation from a heterogeneous  
758 DMM source mantle that was variably fluxed by slab fluids.

759 The above considerations support a BAB origin for the THO magmatic rocks. Only  
760 plagiogranites and amphibole gabbros show strong IAT signatures (Fig. 12D). These  
761 geochemical signatures resemble Sabzevar ophiolite magmatic rocks ([Moghadam et al.,  
762 2014a](#)).

#### 763 *Zr/Nb - Hf/Nb and Th/Nd - <sup>143</sup>Nd/<sup>144</sup>Nd discrimination diagrams*

764 The composition of BAB basalts varies significantly, indicating that BABB melts are  
765 derived from heterogeneous mantle sources, which range from depleted to enriched and  
766 from MORB-like to arc-like ([Stern, 2002](#); [Taylor and Martinez, 2003](#)). The THO igneous

767 rocks are LREE-depleted or slightly enriched relative to N-MORB, similar to BABB  
768 (Fig. 12) like those of the Lau Basin ([Tian et al., 2011](#)) and Okinawa Trough ([Shinjo,  
769 1999](#)). The THO igneous rocks involve both depleted (FAB and D-type BABB-like  
770 igneous rocks) and enriched (E-BABB and E-MORB-like rocks) mantle components, a  
771 conclusion which is supported by the plot of Hf/Nb vs Zr/Nb ([Sorbadere et al., 2013](#))  
772 (Fig. 16C).

773 To better understand the contribution of slab-derived components to the mantle  
774 source of THO igneous rocks, we used a plot of Th/Nb vs  $^{143}\text{Nd}/^{144}\text{Nd}$  (Fig. 16D). THO  
775 igneous rocks reflect variable enrichment by sediment melts, as shown on Fig. 16D  
776 ([Sorbadere et al., 2013](#)). THO melts are like those of the Sabzevar ophiolite, which  
777 sampled multiple mantle and slab components, again consistent with a BAB  
778 interpretation.

#### 779 *Whole rock Nd-Hf and zircon Hf isotopes*

780 Whole rock ( $\epsilon_{\text{Hf}}=+14.9 - +21.5$ ) and zircon ( $\epsilon_{\text{Hf}}= +8.1 - +18.5$ ) Hf- isotope data  
781 from the Torbat-e-Heydariieh ophiolite are comparable. These data indicate that the  
782 mantle source beneath the THO back-arc was broadly MORB-like ([Todd et al., 2011](#);  
783 [Woodhead et al., 2012](#); [Woodhead and Devey, 1993](#)). However, this mantle source also  
784 had slightly enriched components ([Stracke et al., 2005](#)), as shown by Hf and Nd isotopic  
785 data (Fig. 14).

786 All THO lavas seem to be derived from an Indian MORB source mantle (I-DMM),  
787 similar to the source of the Oman ophiolitic gabbros. The addition of HFSE such as Hf  
788 occurs if subducted sediments are melted or if supercritical fluids are involved ([Kessel et  
789 al., 2005](#)). The THO igneous rocks vary modestly in  $\epsilon_{\text{Hf}}$  and  $\epsilon_{\text{Nd}}$ , indicating restricted

790 contributions of subducted sediment melts. We conclude that the THO pillow lavas and  
 791 massive lavas reflect derivation from an Indian Ocean DMM mantle that may have been  
 792 slightly affected by melts of subducted sediments, although some isotropic gabbros and  
 793 E-MORB lavas show a modestly-enriched mantle signature.

794 It is worth noting that THO Hf-isotope compositions are similar to those of the  
 795 Zagros fore-arc ophiolites, both inner belt (Nain-Baft;  $\epsilon_{\text{Hf}}(t) = +8 - +21$ ) and outer belt  
 796 (Neyriz-Kermanshah;  $\epsilon_{\text{Hf}}(t) = +10 - +23$ ) ophiolites, confirming a broadly similar  
 797 mantle source for the generation of Late Cretaceous Iranian ophiolitic magmas. However,  
 798 the conspicuous variations in the zircon  $\epsilon_{\text{Hf}}$  values (+8.1 - +18.5) (which are similar to  
 799 the whole rock Hf isotope variations;  $\epsilon_{\text{Hf}} = +14.9 - +21.5$ ), can reflect mixing with new  
 800 pulses of similar magmas but with slight isotopic differences entering the magma  
 801 chamber during cooling of the plagiogranitic melts ([Shaw and Flood, 2009](#)).

#### 802 *Heterogeneous mantle sources for THO magmas: further thoughts*

803 Table 1 summarizes possible sources and tectonic affinities of the studied THO  
 804 rocks. As discussed above, lherzolites and impregnated lherzolites are similar to MOR  
 805 abyssal peridotite. Dunites are most like SSZ-FA mantle whereas plagioclase lherzolites  
 806 are most like sub-arc mantle. Plagiogranites and amphibole gabbros also have strong arc  
 807 affinities. Lavas, dikes in peridotite, other gabbros, and harzburgites have the strongest  
 808 affinities with BAB (Table 1).

809 Cumulate gabbros are melt-deficient equivalents of isotropic gabbros; both are  
 810 probably derived from Nb-Ta depleted N-MORB-like magmas like THO pillow and  
 811 sheet lavas. Harzburgite is probably melt-depleted residual BAB mantle as indicated by  
 812 Cr# and TiO<sub>2</sub> contents of its spinels (Fig. 10). The Cpx-harzburgite is similar to melt-

813 impregnated harzburgite but with greater addition of abyssal basalt melt (Fig. 10A).  
814 “Abyssal basalt” in this case is not N-MORB but BAB basalt with signatures of slab-  
815 derived fluids. Cpx-harzburgites may represent reactive melt flow channels ([Kimura and](#)  
816 [Sano, 2012](#)). Magmas so generated could have formed dikes within the mantle near the  
817 Moho mantle and could have fractionated to form isotropic and cumulate gabbros. Some  
818 of this magma may have erupted as pillow lavas and sheet lavas to form BAB oceanic  
819 crust Layer 2 ([Hirahara et al., 2015](#)).

820 The presence of heterogeneous mantle rocks (with affinities to FA, IA, and MOR)  
821 associated with THO BAB is consistent with the inferred tectonic setting of the THO.

822

### 823 **Tectonic significance of the Torbat-e-Heydarieh ophiolite**

#### 824 *Timing of back-arc basin opening and its relation to Zagros subduction initiation*

825 Strong upper plate extension accompanies the initiation of some subduction zones  
826 such the Izu-Bonin-Mariana convergent margin, south of Japan. Strong extension on the  
827 upper plate of a nascent subduction zone, above the sinking lithosphere, allows  
828 asthenospheric upwelling and leads to seafloor spreading, forming infant arc crust of the  
829 proto-forearc ([Stern, 2004](#); [Stern and Gerya, 2017](#)). ([Gurnis et al., 2004](#); [Hall et al.,](#)  
830 [2003](#)) suggest that rapid trench retreat and extension in the overriding plate also occur  
831 after subduction becomes self-sustaining, others believe that trench roll-back (and back-  
832 arc extension) can start after the slab pull becomes greater than the far-field push ([Baes et](#)  
833 [al., 2011](#)).

834 Late Cretaceous Zagros ophiolites and their ~3000 km long equivalents in Oman and  
835 from the Mediterranean area (Cyprus, Turkey, Syria to Iraq) show a site of Late

836 Cretaceous subduction initiation along the southern margin of Eurasia ([Moghadam and](#)  
837 [Stern, 2011](#); [Monsef et al., 2018](#)). The chemo-stratigraphic relationships of the lavas from  
838 these ophiolites, integrated with mantle geochemistry and paleomagnetic data, support  
839 the idea of arc infancy at the southern margin of Eurasia during the Late Cretaceous  
840 ([Dilek et al., 2007](#); [Maffione et al., 2017](#); [Moghadam and Stern, 2011](#); [Monsef et al.,](#)  
841 [2018](#); [Pearce and Robinson, 2010](#)). It is also suggested that the earliest subduction stage  
842 after the SI coincided with the transient transfer of high-pressure rocks from the top of  
843 the subducting slab to the overriding plate ([van Hinsbergen et al., 2015](#)). Late Cretaceous  
844 high-pressure rocks are common within the Oman and Zagros ophiolites ([Guilmette et al.,](#)  
845 [2018](#); [Moghadam et al., 2017a](#)), and further attest to the transfer of deep-seated rocks  
846 during the earliest stage of subduction.

847       Because of their setting far to the north of the Late Cretaceous Zagros SI plate  
848 margin, STHO ophiolites must have formed in a back-arc basin. They are easily related to  
849 the Late Cretaceous (~104-98 Ma) formation of a new subduction zone along the  
850 southern margin of Iran, where seafloor spreading formed new oceanic lithosphere  
851 (Zagros inner and outer belts ophiolites) ([Moghadam and Stern, 2015](#)). Subduction  
852 initiation was followed quickly by arc magmatism to form the Urumieh-Dokhtar  
853 Magmatic Belt (e.g., ([Chiu et al., 2013](#); [Ghasemi and Manesh, 2015](#); [Ghorbani et al.,](#)  
854 [2014](#); [Honarmand et al., 2014](#))). Opening of the STHO BAB probably reflected strong  
855 regional extension of the overriding plate during subduction initiation. Our zircon U-Pb  
856 ages range from ~99 to 92 Ma, reflecting a period of ~7 Myr for formation of the THO  
857 ophiolite. A similar age range is also indicated by Cenomanian to Turonian (~ 99-90 Ma)  
858 carbonates deposited over the massive and pillow lavas.

859        Such a broad zone of extension accompanying SI is consistent with IODP 351  
860 drilling results west of the IBM arc, where scientists were surprised to find Eocene  
861 basalts far west of where subduction began at ~51 Ma ([Hickey-Vargas et al., 2018](#)). The  
862 dominance of Late Cretaceous extension in NE Iran is also confirmed by the presence of  
863 a sheeted dike complex in the Sabzevar ophiolites with U-Pb ages of ~90 Ma obtained  
864 from the felsic dikes ([Moghadam et al., 2014b](#)). This extension was also associated with  
865 basement-involved low-angle normal faulting, core complex exhumation, block tilting  
866 and sedimentary basin formation in some parts of Iran (e.g., in Saghand, Fig. 1 ([Verdel et](#)  
867 [al., 2007](#)), in Golpayegan ([Moritz and Ghazban, 1996](#)) and in Torud ([Malekpour-](#)  
868 [Alamdari et al., 2017](#)), attested by  $^{39}\text{Ar}$ - $^{40}\text{Ar}$  and K-Ar ages. These results show that  
869 extensional deformation prevailed during Late Cretaceous in what is now the Iranian  
870 plateau. Extension in NE Iran also generated a volcano-sedimentary basin ([Southern](#)  
871 [Sabzevar basin, N-NW of Oryan](#)) which was filled by Late Cretaceous pelagic sediments,  
872 green siliceous tuffs and submarine volcanic rocks ([Kazemi et al., 2019](#)). Late Cretaceous  
873 extension also allowed asthenospheric melts with radiogenic isotopic compositions to  
874 invade the continental crust and generate granitoids and lavas with radiogenic Nd and  
875 zircon Hf isotopic compositions (e.g., ([Alaminia et al., 2013](#); [Kazemi et al., 2019](#))).

#### 876 *Tectonic setting of the Torbat-e-Heydarieh ophiolite*

877        Three key questions concerning the Torbat-e-Heydarieh ophiolite are addressed here:  
878 1) What is the relationship between the Sabzevar and Torbat-e-Heydarieh ophiolites? 2)  
879 What is the relationship between STHO ophiolites and other ophiolites of similar age in  
880 eastern Iran? 3) What is the relationship between the Zagros fore-arc ophiolites and the  
881 STHO?

882 The ages obtained here agree with U-Pb zircon ages of 100 to 78 Ma for the  
883 Sabzevar ophiolite ([Moghadam et al., 2014a](#)). THO ages are also similar to zircon U-Pb  
884 ages obtained for dacitic-andesitic lavas from the Cheshmeshir and Oryan ophiolites  
885 (~102-76 Ma, Fig. 3; *Moghadam et al., unpublished data*). Some of the younger ages  
886 may reflect arc magmatism. Together, results from the THO, Sabzevar and  
887 Cheshmehshir-Oryan ophiolites indicate a Late Cretaceous oceanic basin that was  
888 magmatically active and perhaps open for ~26 Ma. Our age results indicate that the  
889 Zagros SI may be somewhat older than the formation of the NE Iran back-arc basins  
890 (104-98 Ma *vs* 99-92).

891 Late Cretaceous mantle upwelling accompanying extension led to the emplacement  
892 of several juvenile intrusions and associated extrusive rocks (Late Cretaceous-Eocene  
893 magmatic belt in Fig. 3). These Late Cretaceous igneous rocks are abundant in NE Iran  
894 and are mostly juvenile additions from the mantle to the crust. Xenocrystic zircons (with  
895 ages of 1.1-1.5 Ga) from sample TH11-29 (diabasic dike within peridotites) suggest that  
896 recycling of ancient subducted materials accompanied back-arc opening. These  
897 xenocrytic zircons are found in many Neotethyan ophiolites in China and the  
898 Mediterranean realm (e.g., ([Gong et al., 2016](#); [Robinson et al., 2015](#))).

899 The Torbat-e-Heydariieh ophiolite probably represents an extension of the Sabzevar  
900 ophiolite. Although the formation age of these ophiolites (Sabzevar and THO) is nearly  
901 synchronous, there are striking differences in the tectono-metamorphic evolution of the  
902 two ophiolite belts. The main differences include: 1- mantle peridotites are more  
903 important in the THO and spinels from Sabzevar mantle peridotites have SSZ- or fore-  
904 arc-type signatures, characterized by higher Cr# ([Shafaii Moghadam et al., 2015](#)) (Fig.

905 10B). 2- Podiform chromitites are rare in the THO and abundant in the Sabzevar  
906 ophiolite; 3 -Acidic volcanic rocks are abundant in Sabzevar, whereas mafic volcanics  
907 are more important in the THO (Fig. 13A). Sabzevar volcanic rocks show more  
908 pronounced arc signatures than do those of the THO, indicated by higher Th/Yb, Th/Nb  
909 and Ce/Nb ratios (Figs. 15A-B). 4- OIB-type lavas are present in Sabzevar ([Moghadam et](#)  
910 [al., 2014a](#)) but are absent in the THO, although the latter contains minor E-MORB. 5-  
911 The Sabzevar ophiolite marks an orogenic suture, with a Paleocene HP/LT metamorphic  
912 core ([Omran et al., 2013](#); [Rossetti et al., 2014](#)) and an external thrust-and-fold belt,  
913 showing evidence of a ductile-to-brittle top-to-the-SSE sense of tectonic transport  
914 ([Rossetti et al., 2014](#)). Moreover, a HP granulite event, Albian in age, may exist in the  
915 Sabzevar zone ([Nasrabad et al., 2011](#); [Rossetti et al., 2010](#)). Conversely, the Torbat-e-  
916 Heydarieh ophiolite realm does not show evidence of orogenic metamorphism, and the  
917 post-Cretaceous tectonic evolution has been controlled by polyphase strike-slip shearing  
918 ([Tadayon et al., 2017](#)).

919 The observation that all Sabzevar lavas and mantle peridotites have SSZ signatures  
920 whereas THO lavas and peridotites have mostly MORB-like signatures, as well as the  
921 presence of older high-P rocks in the Sabzevar and their absence in the Torbat-e-  
922 Heydarieh, may indicate that the Torbat-e-Heydarieh and Sabzevar ophiolites represent  
923 distinct back-arc basins, differing proximities to the arc, or different stages in BAB  
924 opening. It is probably not realistic to consider two neighboring oceanic basins so close  
925 together in NE Iran during Late Cretaceous time, although distinct rift basins existed due  
926 to strike-slip faulting accompanying break-up of the continental lithosphere in NE Iran.  
927 We prefer to interpret STHO ophiolite fragments as having formed in a single back-arc

928 basin, perhaps in distinct extensional basins (grabens), developed during Late Cretaceous  
929 hyperextension in the region.

930       Regarding the second question, what is the relationship of STHO to other Late  
931 Cretaceous oceanic remnants in eastern Iran? We believe that back-arc opening  
932 experienced distinct spatio-temporal and geodynamic evolution, but nearly all formed  
933 due to the extensional regime which prevailed in the region during the latest Early to Late  
934 Cretaceous (~110-70 Ma). The Birjand-Zahedan ophiolites in eastern Iran (Fig. 1) are  
935 similar in age to the STHO. SHRIMP U-Pb zircon dating of metafelsic rocks and  
936 eclogites from the Birjand-Zahedan ophiolites gave ages of ~ 86-89 Ma ([Bröcker et al.,](#)  
937 [2013](#)) (Fig. 13). In addition, zircon U-Pb ages from Birjand-Zahedan gabbros are  
938 somewhat older than STHO ophiolites; 113-107 Ma ([Zarrinkoub et al., 2012](#)). These may  
939 be related to a different episode of Early Cretaceous subduction in the region. Zircon and  
940 titanite from felsic segregations in mafic granulites from the Sabzevar ophiolite yield U-  
941 Pb ages of  $107.4 \pm 2.4$  and  $105.9 \pm 2.3$  Ma, respectively (Fig. 13; [Rossetti et al., 2010](#))).  
942 This evidence might suggest the formation of Early Cretaceous (i.e. pre-Albian)  
943 Sabzevar-Birjand-Zahedan single oceanic realm in the upper plate above a Neothethys  
944 subduction zone. In fact, the formation of these high HP granulites in a subduction zone  
945 is questionable, as these rocks contain no high-P minerals and its zircon U-Pb age (ca.  
946 107 Ma) is similar to its titanite age (ca. 105 Ma) and both are similar to the zircon U-Pb  
947 ages reported from the felsic to mafic magmatic rocks from the Sabzevar area (Fig. 3).  
948 Therefore, we believe these metamorphic rocks (with amphibole-plagioclase-garnet  $\pm$   
949 titanite as rock-forming minerals) had a mafic protolith and were not metamorphosed in a  
950 subduction zone. It seems that a MORB precursor related to 105 Ma granulites existed in

951 the Sabzevar area during the Lower Cretaceous (Nasrabad et al., 2011). This may imply  
952 that an oceanic crust older than 105 Ma was present in NE Iran, before the Torbat-e-  
953 Heydarieh back-arc basin start to open.

954 Finally, what is the relationship between Zagros ophiolites and the STHO? There are  
955 geochemical similarities, but Zagros ophiolites are mostly slightly older (*ca* 104-98 Ma)  
956 than the STHO (*ca* 99-80 Ma). This may reflect the migration of extension accompanying  
957 subduction initiation; first in what becomes the fore-arc, then as the slab descends the  
958 locus of extension migrates to the back-arc region (Fig. 17A). In this scenario, the STHO  
959 represents a back-arc basin that formed behind the Zagros fore-arc and the nascent  
960 Urumieh-Dokhtar magmatic arc (Fig. 17B). Back-arc opening would have disrupted  
961 Cadomian continental crust, including Cadomian subcontinental lithospheric mantle  
962 (SCLM; the Lu-Hf vs Hf plot, *not shown*, indicates an isochron with a Cadomian mantle-  
963 depletion age of ~585 Ma). Involvement of such SCLM may explain the origin of OIB-  
964 type lavas in the Sabzevar ophiolite and E-MORB in THO. How far west this back-arc  
965 basin can be traced remains unclear, because the region to the SW between the STHO  
966 and the Nain ophiolites of similar age is covered by younger deposits for ~400 km (Fig.  
967 1). Geophysical studies of this region including magnetics and gravity may help answer  
968 this question.

969 It is also unresolved when and why the STHO BAB collapsed. U-Pb ages for THO  
970 indicate a lifespan of ~7 million years, slightly less than the lifespan of  $12.5 \pm 4.7$  Ma for  
971 global extinct BABs (Stern and Dickinson, 2010). One possibility is that the Iranian  
972 continental lithosphere had been weakened by prolonged arc igneous activity, allowing  
973 the basin to collapse when regional stress changed from extension to compression as the

974 subduction zone evolved. There is abundant evidence for prolonged arc igneous activity  
975 from Late Cretaceous time onwards (e.g., ([Chiu et al., 2013](#); [Honarmand et al., 2014](#);  
976 [Hosseini et al., 2017](#); [Verdel et al., 2011](#))). The volcano-pelagic series above the STHO  
977 includes Cenomanian to Maastrichtian deep-sea pelagic sediments interbedded with  
978 pyroclastic and andesitic to dacitic lavas. Dacitic-andesitic lavas from the Cheshmehshir  
979 and Oryan ophiolites have Late Cretaceous (~102-76 Ma) U-Pb ages (*Moghadam et al.,*  
980 *unpublished data*). This sequence grades upward into a series of Maastrichtian to  
981 Paleocene shallow water sediments and then into the Oryan marine sediments (lower and  
982 middle Oryan sediments) from early Eocene to early middle Eocene. Moreover, zircon U-  
983 Pb ages for plutonic rocks from south of Sabzevar and Neyshabour (Fig. 3, between the  
984 Sabzevar ophiolite in the north and the Cheshmeshir ophiolite in the south) are of  
985 Cenomanian-Maastrichtian ( $97.0 \pm 0.2$  Ma;  $67.5 \pm 0.5$  Ma) to Oligo-Miocene ( $29.8 \pm 0.2$   
986 Ma) (*Moghadam et al., unpublished data*; ([Alaminia et al., 2013](#))). The Late Cretaceous  
987 ages are similar to the U-Pb zircon ages of the Sabzevar plagiogranites (100 to 78 Ma).

988

## 989 CONCLUSIONS

990 Our study of the THO confirms that it formed in Late Cretaceous time. Dikes  
991 intruding THO mantle peridotites and plagiogranites have U-Pb ages of 99-92 Ma. THO  
992 igneous rocks have a range of  $\epsilon_{\text{Nd}}(t)$  between +5.7 - +8.2 and their  $\epsilon_{\text{Hf}}(t)$  values range  
993 from +14.9 to +21.5; THO zircons have  $\epsilon_{\text{Hf}}(t)$  values of +8.1 - +18.5. Like all NE Iran  
994 ophiolites, the THO is found in a tectonic position well to the north of slightly older  
995 Zagros fore-arc ophiolites and the Urumieh-Dokhtar magmatic belt, and thus appears to  
996 have formed as a continental back-arc basin. Petrological, geochemical, and isotopic

997 compositions are consistent with this interpretation. THO peridotites contain spinels and  
998 clinopyroxenes with compositions like those in peridotites from mid-ocean ridges and  
999 back-arc basins. THO igneous rocks have Hf-Nd isotopic compositions that are similar to  
1000 Indian Ocean MORBs, and do not show clear evidence for addition of sediment-derived  
1001 melts or fluids from a subducted slab. Magmatic rocks in the Torbat-e-Heydarieh  
1002 ophiolite show both MORB-like and SSZ geochemical signatures. We conclude that  
1003 formation of the Sabzevar- Torbat-e-Heydarieh ophiolite reflects opening of a Late  
1004 Cretaceous back-arc basin as a result of regional hyper-extension accompanying  
1005 subduction initiation along southern Iran.

1006

#### 1007 **ACKNOWLEDGMENTS**

1008 This is contribution 1236 from the ARC Centre of Excellence for Core to Crust Fluid  
1009 Systems (<http://www.ccfs.mq.edu.au>), 1275 from the GEMOC Key Centre  
1010 (<http://www.gemoc.mq.edu.au>), and UTD Geosciences contribution number 1343 and is  
1011 related to IGCP-662. Zircon U-Pb geochronology, clinopyroxene *in situ* trace elements  
1012 and zircon Lu-Hf isotope data were obtained using instrumentation funded by DEST  
1013 Systemic Infrastructure Grants, ARC LIEF, NCRIS/AuScope, industry partners, and  
1014 Macquarie University. We thank Prof S. Arai for his support during EMP analysis at  
1015 Kanazawa University. We are very grateful to Federico Rossetti, an anonymous reviewer  
1016 and GSA Bulletin's associate editor for their constructive reviews of the manuscript.  
1017 Editorial suggestions by Brad Singer are appreciated. All logistical support for field  
1018 studies came from Damghan University.

1019

1020 **FIGURE CAPTIONS**

1021 Fig. 1- Simplified geological map of Iran emphasizing Cadomian rocks, the main  
1022 ophiolitic belts (thick dashed lines) and Cenozoic magmatic rocks. A-B line shows the  
1023 cross-section position in Fig. 2C.

1024 Fig. 2- (A) and (B) Schematic model showing the opening and evolution of the Sabzevar-  
1025 Torbat-e-Heydarieh back-arc basin relative to the Zagros, Neotethyan Ocean (modified  
1026 after ([Dercourt et al., 1986](#); [Kazmin et al., 1986](#))).

1027 Fig. 3- Geological map of the Sabzevar-Torbat-e-Heydarieh region, north of the  
1028 Dorouneh Fault, with emphasis on the distribution of ophiolitic and arc-related rocks.  
1029 (Abbreviations are M et al.= *Moghadam et al., unpublished data*; K et al.= ([Kazemi et al.,](#)  
1030 [2019](#)); M et al., 2014= ([Moghadam et al., 2014a](#))).

1031 Fig. 4- Simplified geological map of the Torbat-e-Heydarieh ophiolite (modified after  
1032 ([Vaezi Pour et al., 1992](#))).

1033 Fig. 5- Simplified stratigraphic column displaying idealized internal lithologic  
1034 successions in THO.

1035 Fig. 6- Outcrop photos of the THO rock units. (A) outcrops of mantle peridotites. (B)  
1036 Rodingitized dikes within the THO mantle peridotites. (C) Outcrop of interlayered  
1037 cumulate gabbros (layered gabbros) and clinopyroxenites. (D) Small intrusions of  
1038 cumulate (layered) gabbros within the THO mantle sequence. (E) Plagiogranitic dikes  
1039 within the mantle gabbroic intrusions. (F) Angular gabbroic xenoliths within the  
1040 plagiogranitic pockets. (G) Outcrops of crustal massive and pillow lavas. (H-I) Late  
1041 Cretaceous (Cenomanian to Turonian, ~ 99-90 Ma) pelagic sediments are interlayered  
1042 with and conformably cover the lavas.

1043 Fig. 7- Photomicrographs of the THO mantle peridotites and gabbros. (A) Opx, Cpx and  
1044 serpentinized olivine in lherzolites. (B) Serpentinized olivines, Opx and Cpx grains as  
1045 embayment within the Opx in Cpx-harzburgites. (C) Serpentinized olivine, Opx and Cpx  
1046 aggregates within the impregnated lherzolites. (D) Coarse-grained Cpx crystals and  
1047 altered plagioclase in plagioclase-bearing lherzolites. (E) and (F) Opx, Cpx and  
1048 plagioclase in mantle cumulate gabbros.

1049 Fig. 8- Back-scattered images of THO mantle rocks. (A) Association of clinopyroxene  
1050 and vermicular spinels at the embayments of orthopyroxene porphyroclasts in Cpx-  
1051 harzburgites. (B) Altered plagioclase enclosed by large Cpx grains in plagioclase  
1052 lherzolites. (C) Olivine, Opx, Cpx and plagioclase in plagioclase lherzolites. (D) Cpx and  
1053 chloritized amphibole inclusions in the chromite of dunites. (E) and (F) Cumulate texture  
1054 in mantle cumulate gabbros with early crystallized Opx and Cpx and late-stage,  
1055 interstitial plagioclase crystals.

1056 Fig. 9- Modal composition of THO mantle peridotites (A) and gabbros (B).

1057 Fig. 10- (A) Relationship between Cr# and TiO<sub>2</sub> contents of spinel in mantle peridotites  
1058 of the Torbat-e-Heydariieh ophiolite. The thick gray arrow shows the effect of melts (with  
1059 composition of Troodos boninites) on refractory subduction-zone peridotites.

1060 Compositions of Tonga and Izu-Bonin-Mariana island arc tholeiites and abyssal basalts  
1061 are from ([Pearce et al., 2000a](#)) and the composition of Troodos boninite is from ([Dick  
1062 and Bullen, 1984](#)). (B) Relationship between Cr# and Mg# of spinels in Torbat-e-  
1063 Heydariieh mantle peridotites. Abyssal-peridotite fields are from ([Dick and Bullen, 1984](#)),  
1064 fore-arc-peridotite field is from ([Pearce et al., 2000a](#)). Data on Sabzevar peridotites are  
1065 from ([Moghadam et al., 2014a](#)). (C) Mg# vs TiO<sub>2</sub> contents of clinopyroxene from

1066 peridotite and mantle gabbro (abyssal and fore-arc peridotite fields are from ([Bedard et](#)  
1067 [al., 2009](#)). (D)- Anorthite content vs clinopyroxene Mg# (modified after ([Sanfilippo et al.,](#)  
1068 [2013](#))) in Torbat-e-Heydarieh gabbroic rocks. The Kizildag ophiolite data are from  
1069 ([Bagci et al., 2005](#)). Fields of MORB and arc gabbro are from ([Burns, 1985](#)).

1070 Fig. 11- Abundances of Rare Earth Elements and other trace elements in clinopyroxene in  
1071 lherzolites and cumulate gabbros (A-B) and impregnated and plagioclase lherzolites (C-  
1072 D), from the Torbat-e-Heydarieh ophiolite. Chondrite normalization values are from  
1073 ([Mcdonough and Sun, 1995](#)). Fields for abyssal and supra-subduction zone (SSZ-)  
1074 peridotite clinopyroxenes are from ([Bizimis et al., 2000](#); [Johnson et al., 1990](#)). The  
1075 composition of MOR cumulate Cpx is from ([Ross and Elthon, 1993](#)). Data on Sabzevar  
1076 ophiolite rocks are from ([Shafaii Moghadam et al., 2015](#)).

1077 Fig. 12- Chondrite-normalized REE patterns (chondritic abundances from ([Mcdonough](#)  
1078 [and Sun, 1995](#))) and primary mantle and N-MORB normalized multi-element patterns  
1079 (N-MORB and primary mantle concentrations from ([Mcdonough and Sun, 1995](#))) for  
1080 Torbat-e-Heydarieh peridotites, mantle gabbros, plagiogranites and crustal magmatic  
1081 rocks.

1082 Fig. 13- (A)  $\text{FeO}^*/\text{MgO}$  vs  $\text{SiO}_2$  ([Miyashiro, 1974](#)) and (B) Ti vs V diagrams ([Shervais,](#)  
1083 [1982](#)) for THO rocks. Data for the Sabzevar ophiolite are from ([Moghadam et al., 2014a](#)).

1084 Fig. 14-  $\epsilon\text{Hf}$  vs  $\epsilon\text{Nd}$  for the Torbat-e-Heydarieh magmatic rocks, recalculated at 100 Ma  
1085 (modified after ([Chauvel et al., 2009](#))). In panel (A), our samples are compared to the  
1086 MORB and OIB-type lavas, whereas in panel (B), the mixing trend between depleted  
1087 mantle reservoir and different-types of sediments is shown. Data for Oman plagiogranites  
1088 are from ([Haase et al., 2015](#)) and data from Dehshir ophiolites are from ([Moghadam et](#)

1089 [al., 2012](#)). MORB and OIB data are from ([Chauvel and Blichert-Toft, 2001a](#); [Nowell et](#)  
1090 [al., 1998](#); [Pearce et al., 1999](#); [Woodhead et al., 2001](#)). Mantle array data are after  
1091 ([Vervoort and Blichert-Toft, 1999a](#)).

1092 Fig. 15- Zircon SHRIMP and LA-ICPMS U-Pb data from the Torbat-e-Heydarieh  
1093 plagiogranite and diabasic-gabbroic dikes.

1094 Fig. 16- (A) Th/Yb vs Ta/Yb ([Pearce and Peate, 1995](#)) and (B) Ce/Nb vs Th/Nb  
1095 ([Sandeman et al., 2006](#)) diagrams for the Torbat-e-Heydarieh magmatic rocks.  
1096 Hf/Nb vs Zr/Nb (C) and Th/Nb vs  $^{143}\text{Nd}/^{144}\text{Nd}$  plots (D) ([Sorbadere et al., 2013](#)) for THO  
1097 magmatic rocks, Okinawa Trough, Central Lau basin and Sabzevar ophiolitic igneous  
1098 rocks, comparing the effect of enrichment and depletion in the mantle sources of these  
1099 magmas, with respect to the N-MORB source. Pale red field shows bulk mixing between  
1100 N-MORB and sediment and between N-MORB and fluid and thus represents the slab  
1101 contribution (modified after ([Sorbadere et al., 2013](#))). Data from the Sabzevar ophiolite  
1102 are from ([Moghadam et al., 2014a](#)). Data from the Lau back-arc basin and the Okinawa  
1103 Trough are from ([Tian et al., 2011](#)) and ([Shinjo, 1999](#)) respectively.

1104 Fig. 17- Schematic model showing the generation of the Sabzevar-Torbat-e-Heydarieh  
1105 ophiolites. (A) Subduction initiation and Neotethys sinking caused strong extension in the  
1106 region above the sinking lithosphere, leading to seafloor spreading and forming the proto-  
1107 fore-arc crust. Strong extension in the Iranian continental crust lead to extensional basins  
1108 opening and nucleation of the STHO back-arc basin. (B) Beginning of true subduction  
1109 (~100 Ma), and formation of the Urumieh-Dokhtar arc and the STHO back-arc basin.

1110

1111 **TABLE CAPTION**

1112 Table 1- Provenance of the mantle-crust-lava units of THO.

1113 **SUPPLEMENTARY DATA**

1114 Supplementary Table 1- Representative compositions of minerals in the Torbat-e-  
1115 Heydarieh ophiolites.

1116 Supplementary Table 2- Trace elements composition of minerals from THO mantle  
1117 peridotites and cumulate gabbros.

1118 Supplementary Table 3- Whole rock data of the THO mantle peridotites and gabbros.

1119 Supplementary Table 4- Whole rock analysis of the THO magmatic rocks.

1120 Supplementary Table 5- Whole rock Nd-Hf isotope data for the Torbat-e-Heydarieh  
1121 ophiolitic rocks.

1122 Supplementary Table 6- SHRIMP U-Pb data for zircon from magmatic rocks of the  
1123 Torbat-e-Heydarieh ophiolites.

1124 Supplementary Table 7- LA-ICPMS U-Pb data for zircon from magmatic rocks of the  
1125 Torbat-e-Heydarieh ophiolites.

1126 Supplementary Table 8- Lu-Hf isotope data for zircon from magmatic rocks of the  
1127 Torbat-e-Heydarieh ophiolites.

1128

1129 **ELECTRONIC APPENDIX A**

1130 Major element compositions of minerals were analyzed using JEOL wavelength  
1131 dispersive electron probe X-ray micro-analyzer (JXA 8800R) at Kanazawa University.  
1132 Accelerating voltage, beam current, and beam diameter for the analyses were 20 kV, 20  
1133 nA, and 3  $\mu\text{m}$ , respectively. Representative mineral compositions are reported in  
1134 Supplementary Table 1.

1135 Trace-element contents of minerals from peridotites and gabbros were analyzed on  
1136 polished thick-sections in the Geochemical Analysis Unit (GAU) at CCFS/GEMOC,  
1137 Macquarie University; Sydney, Australia. An Agilent 7700 laser ablation system has  
1138 been used to analyze trace element abundances in minerals. The Agilent 7700 was  
1139 coupled with a New Wave UP-266 nm Nd:YAG laser microprobe. Data were collected  
1140 and processed using the GLITTER software, which allows for the cleanest part of the  
1141 time-resolved spectrum to be selected, avoiding inclusion phases and host silicate phases.  
1142 NIST-612 and BCR-2 glasses were used as an external calibration. The trace-element  
1143 compositions of minerals are reported in Supplementary Table 2.

1144 Major and trace element analyses of pillow lavas, massive lavas, plagiogranites and  
1145 dikes were carried out using ICP-AES and ICP-MS at CNRS-SARM, Nancy University  
1146 (France), using BR, DR-N, UB-N, AN-G and GH standards. For major elements, the  
1147 uncertainty (1 sigma) is better than 2% for concentrations higher than 5 wt.% and better  
1148 than 5% in the range 0.1-5 wt.%. For trace elements and REEs, the precision is 5% in the  
1149 range 1-100 ppm and 10% in the range 0.1-1 ppm. The bulk rock major and trace  
1150 elements analyses for pillow lavas, massive lavas, plagiogranites and dikes are shown in  
1151 Supplementary Table 4.

1152 Major elements of the Torbat-e-Heydarieh mantle gabbroids and peridotites were  
1153 analyzed using ICP-AES and ICP-MS at ACME Analytical Laboratories Ltd, Canada.  
1154 Concentrations of trace elements in Torbat-e-Heydarieh gabbroids and peridotites were  
1155 determined by Inductively Coupled Plasma Mass Spectroscopy (ICP-MS) using a  
1156 Thermo Scientific X-Series 2 in the Department of Earth Sciences at the University of  
1157 Durham, following a standard nitric and hydrofluoric acid digestion ([Ottley et al., 2003](#)).

1158 Sample preparation was undertaken in clean air laminar flow hoods. Briefly the  
1159 procedure is as follows; into a Teflon vial 4ml HF and 1ml HNO<sub>3</sub> (SPA, ROMIL  
1160 Cambridge) is added to 100 mg of powdered sample, the vial is sealed and left on a hot  
1161 plate at 150 °C for 48 h. The acid mixture was evaporated to near dryness, the moist  
1162 residue has 1 ml HNO<sub>3</sub> added and evaporated again to near dryness. 1 ml HNO<sub>3</sub> was  
1163 again added and evaporated to near dryness. These steps convert insoluble fluoride  
1164 species into soluble nitrate species. Finally, 2.5 ml HNO<sub>3</sub> was added and diluted to 50 ml  
1165 after the addition of an internal standard giving a final concentration of 20 ppb Re and  
1166 Rh. The internal standard was used to compensate for analytical drift and matrix  
1167 suppression effects. Calibration of the ICP-MS was via international rock standards  
1168 (BHVO-1, AGV-1, W-2, and NBS688) with the addition of an in-house standard (GP13)  
1169 ([Ottley et al., 2003](#)). These standards and analytical blanks were prepared by the same  
1170 techniques as for the THO samples. To improve the signal-to-noise threshold for low  
1171 abundances of incompatible trace elements in ultramafic rocks, instrument dwell times  
1172 were increased ([Ottley et al., 2003](#)). The composition of the reference samples (W-2,  
1173 AGV-1, BHVO-1, BE-N, NBS688) was analyzed as unknowns during the same  
1174 analytical runs. For the analyzed elements, reproducibility of these reference samples is  
1175 generally better than 2% and the measured composition compares favorably with that  
1176 published information in ([Potts et al., 1992](#)). The bulk rock major and trace elements  
1177 analyses for cumulate gabbroids and peridotites are shown in Supplementary Table 3.  
1178 Eight whole-rock samples were analyzed for their Nd and Hf isotope compositions  
1179 (Supplementary Table 5). Chemical separation of Nd and Hf used c. 100 mg of sample  
1180 powder that was spiked with mixed <sup>176</sup>Lu-<sup>180</sup>Hf and <sup>149</sup>Sm-<sup>150</sup>Nd tracers and subsequently

1181 digested on a hotplate in a 1:1 mixture of concentrated HF-HNO<sub>3</sub> (24 hours, 120°C).  
1182 Subsequently, the acid mixture was dried and the samples were digested in a 3:2 mixture  
1183 of concentrated HF-HNO<sub>3</sub> in steel-jacketed Parr pressure vessels (3 days, 180°C).  
1184 Subsequently, fluorides were decomposed by drying with 1 ml of perchloric acid and  
1185 three additional dry-down steps with concentrated HNO<sub>3</sub>. The chemical separation of Hf  
1186 and Lu from the matrix follows the procedure of ([Munker et al., 2001](#)). Samarium and Nd  
1187 were separated from the residue after Hf separation, using Bio-Rad AG50W-X8 cation  
1188 resin (200-400 mesh) and Ln-Spec resin ([Pin and Zalduogui, 1997](#)).

1189 The Nd and Hf isotope compositions as well as Lu-Hf and Sm-Nd concentrations  
1190 were determined using a Thermo-Finnigan Neptune multi-collector ICP-MS at the joint  
1191 clean lab facilities in Cologne/Bonn. Data was collected in static multi-collection mode.  
1192 Values of <sup>143</sup>Nd/<sup>144</sup>Nd and <sup>176</sup>Hf/<sup>177</sup>Hf were corrected for mass fractionation using the  
1193 exponential law and <sup>146</sup>Nd/<sup>144</sup>Nd=0.7219 and <sup>179</sup>Hf/<sup>177</sup>Hf =0.7325, respectively. Repeated  
1194 analyses of the standards La Jolla Nd and Hf AMES (isotopically identical to JMC-475)  
1195 yield mean values of <sup>143</sup>Nd/<sup>144</sup>Nd= 0.511835 (n=2) and <sup>176</sup>Hf/<sup>177</sup>Hf=0.282156 (n=18). The  
1196 external long-term reproducibility is c. ±40 ppm for Nd and Hf isotopes (2 RSD).  
1197 Reported values are given relative to 0.511859 for La Jolla and 0.282160 for Hf AMES.  
1198 Procedural blanks were typically below 60 pg for Hf and Nd. The external precision of  
1199 the Nd and Hf measurements was further assessed by multiple digestions of six samples  
1200 (see Supplementary Table 5). External precision (2 RSD) for the replicates was better  
1201 than 30 ppm for <sup>143</sup>Nd/<sup>144</sup>Nd and 40 ppm for <sup>176</sup>Hf/<sup>177</sup>Hf.

1202 In order to have precise ages for the Torbat-e-Heydarieh ophiolite, zircons from  
1203 plagiogranites (4 samples) and diabasic (1 sample)- rodingitized gabbroic dike (1 sample)

1204 within the mantle harzburgite were analyzed by SHRIMP at the Korea Basic Science  
1205 Institute, Ochang, South Korea and LA-ICPMS at Geochemical Analysis Unit (GAU),  
1206 CCFS/GEMOC, Macquarie University. For SHRIMP analysis, zircon grains were  
1207 mechanically separated using conventional mineral separation techniques that employed  
1208 crushing, grinding, sieving, and magnetic separation steps, followed by handpicking of  
1209 zircons under a binocular microscope. The internal structure of these zircon grains was  
1210 studied using transmitted and reflected light optical microscopy, and by scanning electron  
1211 microscope-cathodoluminescence (CL) imaging. Analytical procedures including  
1212 instrumental set-up, and the acquisition and treatment of data employed in this SHRIMP  
1213 U-Pb zircon dating study, are outlined in ([Compston et al., 1984](#)). For the reduction of  
1214 raw data and in making the final age calculations, we used the programs SQUID and  
1215 Isoplot/Ex ([Ludwig, 2003, 2009](#)). The SHRIMP U-Pb zircon analytical data are  
1216 summarized in Supplementary Table 6.

1217 For LA-ICPMS analysis, zircons were separated following electrostatic  
1218 disaggregation (selFrag) of the rock sample, then using standard gravimetric and  
1219 magnetic techniques; grains were picked under a binocular microscope and mounted in  
1220 epoxy discs for analysis. All grains were imaged by CL and BSE to provide maps to  
1221 guide the choice of analytical spots. Zircon U-Pb ages were obtained using a 193 nm ArF  
1222 EXCIMER laser with an Agilent 7700 ICP-MS system. Detailed method descriptions  
1223 have been given by ([Jackson et al., 2004](#)). The ablation conditions included beam size (30  
1224  $\mu\text{m}$ ), pulse rate (5Hz) and energy density ( $7.59 \text{ J/cm}^2$ ). Analytical runs comprised 16  
1225 analyses with 12 analyses of unknowns bracketed by two analyses of a standard zircon  
1226 GJ-1 at the beginning and end of each run, using the established TIMS values

1227 ( $^{207}\text{Pb}/^{206}\text{Pb}$  age= 608.5 Ma, [\(Jackson et al., 2004\)](#)). U-Pb ages were calculated from the  
1228 raw signal data using the on-line software package GLITTER [\(Griffin et al., 2008\)](#). U-Pb  
1229 age data were subjected to a common-lead correction, except for those with common-Pb  
1230 concentrations lower than detection limits. The results were processed using the  
1231 ISOPLOT program of [\(Ludwig, 2003\)](#). The external standards, zircons 91500 and Mud  
1232 Tank, gave mean  $^{206}\text{Pb}/^{238}\text{U}$  ages of  $1063.5\pm 1.8$  Ma (MSWD=1.3) and  $731.1\pm 1.2$  Ma  
1233 (MSWD=0.77), respectively, which are similar to the recommended  $^{206}\text{Pb}/^{238}\text{U}$  ages of  
1234  $1062.4\pm 0.4$  Ma and  $731.9\pm 3.4$  Ma respectively [\(Chang et al., 2006; Woodhead and](#)  
1235 [Hergt, 2005; Yuan et al., 2008\)](#). LA-ICPMS U-Pb zircon analytical data is summarized in  
1236 Supplementary Table 7.

1237 *In situ* zircon Lu-Hf isotopic analyses were performed using a Nu Plasma multi-  
1238 collector ICP-MS, coupled to a Photon Machines 193 nm ArF excimer laser system at  
1239 CCFS (Macquarie University). The analyses were carried out using the Nu Plasma time-  
1240 resolved analysis software. The methods, including calibration and correction for mass  
1241 bias, are described by [\(Griffin et al., 2004; Griffin et al., 2000\)](#). The ablation spots (55  
1242  $\mu\text{m}$ ) for the Hf isotope analyses were situated close to the U-Pb analysis positions on  
1243 each grain. The accuracy of the Yb and Lu corrections during LA-MC-ICPMS analysis of  
1244 zircon has been demonstrated by repeated analysis of standard zircons with a range in  
1245  $^{176}\text{Yb}/^{177}\text{Hf}$  and  $^{176}\text{Lu}/^{177}\text{Hf}$ . Four secondary standards (Mud Tank and Temora) were  
1246 analyzed between every ten unknowns to check instrumental stability.  $^{176}\text{Hf}/^{177}\text{Hf}$  ratios  
1247 of the Mud Tank zircon gave an average of  $0.2825355\pm 0.0000041$  (2SD; n=122); those  
1248 of Temora gave  $0.2826971\pm 0.0000078$  (2SD; n=42). These values are identical to those  
1249 recommended for Mud Tank ( $0.282507\pm 0.000003$ ) and Temora ( $0.282693\pm 0.000052$ )

1250 ([Fisher et al., 2014](#)). The isobaric interferences of  $^{176}\text{Lu}$  and  $^{176}\text{Yb}$  on  $^{176}\text{Hf}$  are very  
1251 limited, because of the extremely low ratios of Lu/Hf and Yb/Hf in the measured  
1252 standard zircons. The interference of  $^{176}\text{Yb}$  on  $^{176}\text{Hf}$  was corrected by measuring the  
1253 interference-free  $^{172}\text{Yb}$  isotope and using  $^{176}\text{Yb}/^{172}\text{Yb}$  to calculate  $^{176}\text{Yb}/^{177}\text{Hf}$ . The  
1254 appropriate value of  $^{176}\text{Yb}/^{172}\text{Yb}$  was determined by successive spiking the JMC475 Hf  
1255 standard (1 ppm solution) with Yb, and iteratively finding the value of  $^{176}\text{Yb}/^{172}\text{Yb}$   
1256 required to yield the value of  $^{176}\text{Hf}/^{177}\text{Hf}$  obtained on the pure Hf solution ([Griffin et al.,](#)  
1257 [2004](#); [Griffin et al., 2000](#)). Zircon Hf isotope data are presented in Supplementary Table  
1258 8.

1259

1260 **REFERENCES**

- 1261 Agard, P., Jolivet, L., Vrielynck, B., Burov, E., and Monie, P., 2007, Plate acceleration:  
1262 The obduction trigger?: Earth and Planetary Science Letters, v. 258, no. 3-4, p. 428-  
1263 441.
- 1264 Alaminia, Z., Karimpour, M. H., Homam, S. M., and Finger, F., 2013, The magmatic  
1265 record in the Arghash region (northeast Iran) and tectonic implications:  
1266 International Journal of Earth Sciences, v. 102, no. 6, p. 1603-1625.
- 1267 Aldanmaz, E., 2012, Trace element geochemistry of primary mantle minerals in spinel-  
1268 peridotites from polygenetic MOR-SSZ suites of SW Turkey: constraints from an  
1269 LA-ICP-MS study and implications for mantle metasomatism: Geological Journal,  
1270 v. 47, no. 1, p. 59-76.
- 1271 Anenburg, M., Katzir, Y., Rhede, D., Jons, N., and Bach, W., 2015, Rare earth element  
1272 evolution and migration in plagiogranites: a record preserved in epidote and allanite  
1273 of the Troodos ophiolite: Contributions to Mineralogy and Petrology, v. 169, no. 3.

- 1274 Arai, S., Kadoshima, K., and Morishita, T., 2006, Widespread arc-related melting in the  
1275 mantle section of the northern Oman ophiolite as inferred from detrital chromian  
1276 spinels: *Journal of the Geological Society*, v. 163, p. 869-879.
- 1277 Baes, M., Govers, R., and Wortel, R., 2011, Subduction initiation along the inherited  
1278 weakness zone at the edge of a slab: Insights from numerical models: *Geophysical*  
1279 *Journal International*, v. 184, no. 3, p. 991-1008.
- 1280 Bagci, U., Parlak, O., and Hock, V., 2005, Whole-rock and mineral chemistry of cumulates  
1281 from the Kizildag (Hatay) ophiolite (Turkey): clues for multiple magma generation  
1282 during crustal accretion in the southern Neotethyan ocean: *Mineralogical*  
1283 *Magazine*, v. 69, no. 1, p. 53-76.
- 1284 Bazylev, B. A., Popevic, A., Karamata, S., Kononkova, N. N., Simakin, S. G., Olujic, J.,  
1285 Vujnovic, L., and Memovic, E., 2009, Mantle peridotites from the Dinaridic  
1286 ophiolite belt and the Vardar zone western belt, central Balkan: A petrological  
1287 comparison: *Lithos*, v. 108, no. 1-4, p. 37-71.
- 1288 Bedard, E., Hebert, R., Guilmette, C., Lesage, G., Wang, C. S., and Dostal, J., 2009,  
1289 Petrology and geochemistry of the Saga and Sangsang ophiolitic massifs, Yarlung  
1290 Zangbo Suture Zone, Southern Tibet: Evidence for an arc-back-arc origin: *Lithos*,  
1291 v. 113, no. 1-2, p. 48-67.
- 1292 Berberian, M., 1983, The southern Caspian: a compressional depression floored by a  
1293 trapped, modified oceanic crust: *Canadian Journal of Earth Sciences*, v. 20, no. 2,  
1294 p. 163-183.
- 1295 Bizimis, M., Salters, V. J., and Bonatti, E., 2000, Trace and REE content of clinopyroxenes  
1296 from supra-subduction zone peridotites. Implications for melting and enrichment  
1297 processes in island arcs: *Chemical Geology*, v. 165, no. 1-2, p. 67-85.
- 1298 Bonev, N., and Stampfli, G., 2009, Gabbro, plagiogranite and associated dykes in the  
1299 supra-subduction zone Evros Ophiolites, NE Greece: *Geological Magazine*, v. 146,  
1300 no. 1, p. 72-91.

- 1301 Bröcker, M., Fotoohi Rad, G. F., Burgess, R., Theunissen, S., Paderin, I., Rodionov, N.,  
1302 and Salimi, Z., 2013, New age constraints for the geodynamic evolution of the  
1303 Sistan Suture Zone, eastern Iran: *Lithos*, v. 170, p. 17-34.
- 1304 Burns, L. E., 1985, The Border Ranges Ultramafic and Mafic Complex, South-Central  
1305 Alaska - Cumulate Fractionates of Island-Arc Volcanics: *Canadian Journal of Earth*  
1306 *Sciences*, v. 22, no. 7, p. 1020-1038.
- 1307 Burtman, V., 1994, Meso-Tethyan oceanic sutures and their deformation: *Tectonophysics*,  
1308 v. 234, no. 4, p. 305-327.
- 1309 Cawood, P. A., 1989, Acadian Remobilization of a Taconian Ophiolite, Hare Bay  
1310 Allochthon, Northwestern Newfoundland: *Geology*, v. 17, no. 3, p. 257-260.
- 1311 Chang, Z. S., Vervoort, J. D., McClelland, W. C., and Knaack, C., 2006, U-Pb dating of  
1312 zircon by LA-ICP-MS: *Geochemistry Geophysics Geosystems*, v. 7.
- 1313 Chauvel, C., and Blichert-Toft, J., 2001a, A hafnium isotope and trace element perspective  
1314 on melting of the depleted mantle: *Earth and Planetary Science Letters*, v. 190, no.  
1315 3, p. 137-151.
- 1316 Chauvel, C., and Blichert-Toft, J., 2001b, A hafnium isotope and trace element perspective  
1317 on melting of the depleted mantle: *Earth and Planetary Science Letters*, v. 190, no.  
1318 3-4, p. 137-151.
- 1319 Chauvel, C., Marini, J. C., Plank, T., and Ludden, J. N., 2009, Hf-Nd input flux in the Izu-  
1320 Mariana subduction zone and recycling of subducted material in the mantle:  
1321 *Geochemistry Geophysics Geosystems*, v. 10, no. 1, p. n/a-n/a.
- 1322 Chiu, H. Y., Chung, S. L., Zarrinkoub, M. H., Mohammadi, S. S., Khatib, M. M., and  
1323 Iizuka, Y., 2013, Zircon U-Pb age constraints from Iran on the magmatic evolution  
1324 related to Neotethyan subduction and Zagros orogeny: *Lithos*, v. 162, p. 70-87.
- 1325 Coleman, R. G., 1977, *Ophiolites*, New York, Springer-Verlag, 220 p.:

- 1326 Compston, W., Williams, I., and Meyer, C., 1984, U - Pb geochronology of zircons from  
1327 lunar breccia 73217 using a sensitive high mass - resolution ion microprobe:  
1328 Journal of Geophysical Research: Solid Earth, v. 89, no. S02.
- 1329 Dercourt, J., Zonenshain, L. P., Ricou, L. E., Kazmin, V. G., Lepichon, X., Knipper, A. L.,  
1330 Grandjacquet, C., Sbertshikov, I. M., Geysant, J., Lepvrier, C., Pechersky, D. H.,  
1331 Boulin, J., Sibuet, J. C., Savostin, L. A., Sorokhtin, O., Westphal, M., Bazhenov,  
1332 M. L., Lauer, J. P., and Bijuduval, B., 1986, Geological Evolution of the Tethys  
1333 Belt from the Atlantic to the Pamirs since the Lias: Tectonophysics, v. 123, no. 1-  
1334 4, p. 241-315.
- 1335 Dick, H. J. B., and Bullen, T., 1984, Chromian Spinel as a Petrogenetic Indicator in Abyssal  
1336 and Alpine-Type Peridotites and Spatially Associated Lavas: Contributions to  
1337 Mineralogy and Petrology, v. 86, no. 1, p. 54-76.
- 1338 Dilek, Y., and Flower, M. F. J., 2003, Arc-trench rollback and forearc accretion: 2. A model  
1339 template for ophiolites in Albania, Cyprus, and Oman: Ophiolites in Earth History,  
1340 v. 218, p. 43-68.
- 1341 Dilek, Y., and Furnes, H., 2009, Structure and geochemistry of Tethyan ophiolites and their  
1342 petrogenesis in subduction rollback systems: Lithos, v. 113, no. 1-2, p. 1-20.
- 1343 -, 2011, Ophiolite genesis and global tectonics: Geochemical and tectonic fingerprinting of  
1344 ancient oceanic lithosphere: Geological Society of America Bulletin, v. 123, no. 3-  
1345 4, p. 387-411.
- 1346 Dilek, Y., Furnes, H., and Shallo, M., 2007, Suprasubduction zone ophiolite formation  
1347 along the periphery of Mesozoic Gondwana: Gondwana Research, v. 11, no. 4, p.  
1348 453-475.
- 1349 Dilek, Y., and Thy, P., 2006, Age and petrogenesis of plagiogranite intrusions in the  
1350 Ankara melange, central Turkey: Island Arc, v. 15, no. 1, p. 44-57.

- 1351 Fisher, C. M., Vervoort, J. D., and DuFrane, S. A., 2014, Accurate Hf isotope  
1352 determinations of complex zircons using the "laser ablation split stream" method:  
1353 *Geochemistry Geophysics Geosystems*, v. 15, no. 1, p. 121-139.
- 1354 Furnes, H., de Wit, M., and Dilek, Y., 2014, Four billion years of ophiolites reveal secular  
1355 trends in oceanic crust formation: *Geoscience Frontiers*, v. 5, no. 4, p. 571-603.
- 1356 Gerya, T., 2011, Intra-oceanic Subduction Zones, *in* Brown D., R., P.D., ed., *Arc-Continent*  
1357 *Collision*, *Frontiers: Berlin, Springer-Verlag*, p. 23-53.
- 1358 Ghasemi, A., and Manesh, S. M. T., 2015, Geochemistry and petrogenesis of Ghohroud  
1359 Igneous Complex (Urumieh-Dokhtar zone): evidence for Neotethyan subduction  
1360 during the Neogene: *Arabian Journal of Geosciences*, v. 8, no. 11, p. 9599-9623.
- 1361 Ghazi, A., Hassanipak, A., and Wallace, K., 1997, Geochemistry, petrology and geology  
1362 of the Sabzevar ophiolite, Northeastern Iran: Implication on Tethyan tectonics:  
1363 *Geological Society of America*, v. 29.
- 1364 Ghazi, J. M., Moazzen, M., Rahgoshay, M., and Moghadam, H. S., 2010, Mineral chemical  
1365 composition and geodynamic significance of peridotites from Nain ophiolite,  
1366 central Iran: *Journal of Geodynamics*, v. 49, no. 5, p. 261-270.
- 1367 Ghorbani, M. R., Graham, I. T., and Ghaderi, M., 2014, Oligocene-Miocene geodynamic  
1368 evolution of the central part of Urumieh-Dokhtar Arc of Iran: *International Geology*  
1369 *Review*, v. 56, no. 8, p. 1039-1050.
- 1370 Gong, X. H., Shi, R. D., Griffin, W. L., Huang, Q. S., Xiong, Q., Chen, S. S., Zhang, M.,  
1371 and O'Reilly, S. Y., 2016, Recycling of ancient subduction-modified mantle  
1372 domains in the Purang ophiolite (southwestern Tibet): *Lithos*, v. 262, p. 11-26.
- 1373 Griffin, W., Powell, W., Pearson, N., and O'reilly, S., 2008, GLITTER: data reduction  
1374 software for laser ablation ICP-MS: *Laser Ablation-ICP-MS in the earth sciences*.  
1375 *Mineralogical association of Canada short course series*, v. 40, p. 204-207.

- 1376 Griffin, W. L., Belousova, E. A., Shee, S. R., Pearson, N. J., and O'Reilly, S. Y., 2004,  
1377 Archean crustal evolution in the northern Yilgam Craton: U-Pb and Hf-isotope  
1378 evidence from detrital zircons: *Precambrian Research*, v. 131, no. 3-4, p. 231-282.
- 1379 Griffin, W. L., Pearson, N. J., Belousova, E., Jackson, S. E., van Achterbergh, E., O'Reilly,  
1380 S. Y., and Shee, S. R., 2000, The Hf isotope composition of cratonic mantle: LAM-  
1381 MC-ICPMS analysis of zircon megacrysts in kimberlites: *Geochimica Et*  
1382 *Cosmochimica Acta*, v. 64, no. 1, p. 133-147.
- 1383 Guilmette, C., Smit, M. A., van Hinsbergen, D. J. J., Gürer, D., Corfu, F., Charette, B.,  
1384 Maffione, M., Rabeau, O., and Savard, D., 2018, Forced subduction initiation  
1385 recorded in the sole and crust of the Semail Ophiolite of Oman: *Nature Geoscience*,  
1386 v. 11, p. 688–695.
- 1387 Gurnis, M., Hall, C., and Lavier, L., 2004, Evolving force balance during incipient  
1388 subduction: *Geochemistry Geophysics Geosystems*, v. 5.
- 1389 Haase, K. M., Freund, S., Koepke, J., Hauff, F., and Erdmann, M., 2015, Melts of  
1390 sediments in the mantle wedge of the Oman ophiolite: *Geology*, v. 43, no. 4, p. 275-  
1391 278.
- 1392 Hall, C. E., Gurnis, M., Sdrolias, M., Lavier, L. L., and Muller, R. D., 2003, Catastrophic  
1393 initiation of subduction following forced convergence across fracture zones: *Earth*  
1394 *and Planetary Science Letters*, v. 212, no. 1-2, p. 15-30.
- 1395 Hamada, M., and Fujii, T., 2008, Experimental constraints on the effects of pressure and  
1396 H<sub>2</sub>O on the fractional crystallization of high-Mg island arc basalt: *Contributions to*  
1397 *Mineralogy and Petrology*, v. 155, no. 6, p. 767-790.
- 1398 Hébert, R., Bezaud, R., Guilmette, C., Dostal, J., Wang, C. S., and Liu, Z. F., 2012, The  
1399 Indus–Yarlung Zangbo ophiolites from Nanga Parbat to Namche Barwa syntaxes,  
1400 southern Tibet: First synthesis of petrology, geochemistry, and geochronology with  
1401 incidences on geodynamic reconstructions of Neo-Tethys: *Gondwana Research*, v.  
1402 22, no. 2, p. 377-397.

- 1403 Hickey-Vargas, R., Yogodzinski, G., Ishizuka, O., McCarthy, A., Bizimis, M., Kusano, Y.,  
1404 Savov, I., and Arculus, R., 2018, Origin of depleted basalts during subduction  
1405 initiation and early development of the Izu-Bonin-Mariana Island arc: Evidence  
1406 from IODP Expedition 351 Site U1438, Amami-Sankaku Basin: *Geochimica et*  
1407 *Cosmochimica Acta*.
- 1408 Hirahara, Y., Kimura, J. I., Senda, R., Miyazaki, T., Kawabata, H., Takahashi, T., Chang,  
1409 Q., Vaglarov, B. S., Sato, T., and Kodaira, S., 2015, Geochemical variations in  
1410 Japan Sea back - arc basin basalts formed by high - temperature adiabatic melting  
1411 of mantle metasomatized by sediment subduction components: *Geochemistry,*  
1412 *Geophysics, Geosystems*, v. 16, no. 5, p. 1324-1347.
- 1413 Honarmand, M., Omran, N. R., Neubauer, F., Emami, M. H., Nabatian, G., Liu, X. M.,  
1414 Dong, Y. P., von Quadt, A., and Chen, B., 2014, Laser-ICP-MS U-Pb zircon ages  
1415 and geochemical and Sr-Nd-Pb isotopic compositions of the Niyasar plutonic  
1416 complex, Iran: constraints on petrogenesis and tectonic evolution: *International*  
1417 *Geology Review*, v. 56, no. 1, p. 104-132.
- 1418 Hosseini, M. R., Hassanzadeh, J., Alirezaei, S., Sun, W. D., and Li, C. Y., 2017, Age  
1419 revision of the Neotethyan arc migration into the southeast Urumieh-Dokhtar belt  
1420 of Iran: *Geochemistry and U-Pb zircon geochronology: Lithos*, v. 284, p. 296-309.
- 1421 Ishikawa, T., Nagaishi, K., and Umino, S., 2002, Boninitic volcanism in the Oman  
1422 ophiolite: Implications for thermal condition during transition from spreading ridge  
1423 to arc: *Geology*, v. 30, no. 10, p. 899-902.
- 1424 Ishizuka, O., Tani, K., and Reagan, M. K., 2014, Izu-Bonin-Mariana forearc crust as a  
1425 modern ophiolite analogue: *Elements*, v. 10, no. 2, p. 115-120.
- 1426 Jackson, S. E., Pearson, N. J., Griffin, W. L., and Belousova, E. A., 2004, The application  
1427 of laser ablation-inductively coupled plasma-mass spectrometry to in situ U-Pb  
1428 zircon geochronology: *Chemical Geology*, v. 211, no. 1-2, p. 47-69.

- 1429 Johnson, K., Dick, H. J., and Shimizu, N., 1990, Melting in the oceanic upper mantle: an  
1430 ion microprobe study of diopsides in abyssal peridotites: *Journal of Geophysical*  
1431 *Research: Solid Earth*, v. 95, no. B3, p. 2661-2678.
- 1432 Kazemi, Z., Ghasemi, H., Tilhac, R., Griffin, W., Moghadam, H. S., O'Reilly, S., and  
1433 Mousivand, F., 2019, Late Cretaceous subduction-related magmatism on the  
1434 southern edge of Sabzevar basin, NE Iran: *Journal of the Geological Society*, p.  
1435 jgs2018-2076.
- 1436 Kazmin, V. G., Sbornshikov, I. M., Ricou, L. E., Zonenshain, L. P., Boulin, J., and Knipper,  
1437 A. L., 1986, Volcanic Belts as Markers of the Mesozoic-Cenozoic Active Margin  
1438 of Eurasia: *Tectonophysics*, v. 123, no. 1-4, p. 123-152.
- 1439 Kelley, K. A., Kingsley, R., and Schilling, J. G., 2013, Composition of plume - influenced  
1440 mid - ocean ridge lavas and glasses from the Mid - Atlantic Ridge, East Pacific  
1441 Rise, Galápagos Spreading Center, and Gulf of Aden: *Geochemistry, Geophysics,*  
1442 *Geosystems*, v. 14, no. 1, p. 223-242.
- 1443 Kessel, R., Schmidt, M. W., Ulmer, P., and Pettke, T., 2005, Trace element signature of  
1444 subduction-zone fluids, melts and supercritical liquids at 120-180 km depth:  
1445 *Nature*, v. 437, no. 7059, p. 724-727.
- 1446 Khalatbari-Jafari, M., Juteau, T., Bellon, H., Whitechurch, H., Cotten, J., and Emami, H.,  
1447 2004, New geological, geochronological and geochemical investigations on the  
1448 Khoy ophiolites and related formations, NW Iran: *Journal of Asian Earth Sciences*,  
1449 v. 23, no. 4, p. 507-535.
- 1450 Khedr, M. Z., and Arai, S., 2009, Geochemistry of metasomatized peridotites above  
1451 subducting slab: a case study of hydrous metaperidotites from Happo-O'ne  
1452 complex, central Japan: *Journal of Mineralogical and Petrological Sciences*, v. 104,  
1453 no. 5, p. 313-318.

- 1454 Kimura, J.-I., and Sano, S., 2012, Reactive melt flow as the origin of residual mantle  
1455 lithologies and basalt chemistries in mid-ocean ridges: Implications from the Red  
1456 Hills peridotite, New Zealand: *Journal of Petrology*, v. 53, no. 8, p. 1637-1671.
- 1457 Kimura, J.-I., Stern, R. J., and Yoshida, T., 2005, Reinitiation of subduction and magmatic  
1458 responses in SW Japan during Neogene time: *Geological Society of America*  
1459 *Bulletin*, v. 117, no. 7-8, p. 969-986.
- 1460 Lagabriele, Y., Guivel, C., Maury, R. C., Bourgois, J., Fourcade, S., and Martin, H., 2000,  
1461 Magmatic-tectonic effects of high thermal regime at the site of active ridge  
1462 subduction: the Chile Triple Junction model: *Tectonophysics*, v. 326, no. 3-4, p.  
1463 255-268.
- 1464 Leake, B. E., Woolley, A. R., Arps, C. E. S., Birch, W. D., Gilbert, M. C., Grice, J. D.,  
1465 Hawthorne, F. C., Kato, A., Kisch, H. J., Krivovichev, V. G., Linthout, K., Laird,  
1466 J., Mandarino, J., Maresch, W. V., Nickel, E. H., Rock, N. M. S., Schumacher, J.  
1467 C., Smith, D. C., Stephenson, N. C. N., Ungaretti, L., Whittaker, E. J. W., and  
1468 Youzhi, G., 1997, Nomenclature of amphiboles: Report of the Subcommittee on  
1469 Amphiboles of the International Mineralogical Association Commission on New  
1470 Minerals and Mineral Names: *Mineralogical Magazine*, v. 61, no. 2, p. 295-321.
- 1471 Long, M. D., and Wirth, E. A., 2013, Mantle flow in subduction systems: The mantle  
1472 wedge flow field and implications for wedge processes: *Journal of Geophysical*  
1473 *Research: Solid Earth*, v. 118, no. 2, p. 583-606.
- 1474 Ludwig, K. R., 2003, User's Manual for Isoplot 3.00: A Geochronological Toolkit for  
1475 Microsoft Excel.
- 1476 -, 2009, SQUID 2: A User's manual: Berkeley Geochronology Center Special Publications  
1477 4.
- 1478 Maffione, M., van Hinsbergen, D. J. J., de Gelder, G. I. N. O., van der Goes, F. C., and  
1479 Morris, A., 2017, Kinematics of Late Cretaceous subduction initiation in the Neo-

- 1480 Tethys Ocean reconstructed from ophiolites of Turkey, Cyprus, and Syria: *Journal*  
1481 *of Geophysical Research-Solid Earth*, v. 122, no. 5, p. 3953-3976.
- 1482 Maghfouri, S., Rastad, E., Mousivand, F., Lin, Y., and Zaw, K., 2016, Geology, ore facies  
1483 and sulfur isotopes geochemistry of the Nudeh Besshi-type volcanogenic massive  
1484 sulfide deposit, southwest Sabzevar basin, Iran: *Journal of Asian Earth Sciences*, v.  
1485 125, p. 1-21.
- 1486 Malekpour-Alamdari, A., Axen, G., Heizler, M., and Hassanzadeh, J., 2017, Large-  
1487 magnitude continental extension in the northeastern Iranian Plateau: Insight from  
1488 K-feldspar  $^{40}\text{Ar}/^{39}\text{Ar}$  thermochronology from the Shotor Kuh–Biarjmand  
1489 metamorphic core complex: *Geosphere*, v. 13, no. 4, p. 1207-1233.
- 1490 Mcdonough, W. F., and Sun, S. S., 1995, The Composition of the Earth: *Chemical*  
1491 *Geology*, v. 120, no. 3-4, p. 223-253.
- 1492 Miyashiro, A., 1974, Volcanic rock series in island arcs and active continental margins:  
1493 *American journal of science*, v. 274, no. 4, p. 321-355.
- 1494 Moghadam, H. S., Brocker, M., Griffin, W. L., Li, X. H., Chen, R. X., and O'Reilly, S. Y.,  
1495 2017a, Subduction, high-P metamorphism, and collision fingerprints in South Iran:  
1496 Constraints from zircon U-Pb and mica Rb-Sr geochronology: *Geochemistry*  
1497 *Geophysics Geosystems*, v. 18, no. 1, p. 306-332.
- 1498 Moghadam, H. S., Corfu, F., Chiaradia, M., Stern, R. J., and Ghorbani, G., 2014a, Sabzevar  
1499 Ophiolite, NE Iran: Progress from embryonic oceanic lithosphere into magmatic  
1500 arc constrained by new isotopic and geochemical data: *Lithos*.
- 1501 Moghadam, H. S., Corfu, F., Chiaradia, M., Stern, R. J., and Ghorbani, G., 2014b, Sabzevar  
1502 Ophiolite, NE Iran: Progress from embryonic oceanic lithosphere into magmatic  
1503 arc constrained by new isotopic and geochemical data: *Lithos*, v. 210, p. 224-241.
- 1504 Moghadam, H. S., Corfu, F., and Stern, R. J., 2013, U-Pb zircon ages of Late Cretaceous  
1505 Nain-Dehshir ophiolites, central Iran: *Journal of the Geological Society*, v. 170, no.  
1506 1, p. 175-184.

- 1507 Moghadam, H. S., Khedr, M. Z., Arai, S., Stern, R. J., Ghorbani, G., Tamura, A., and  
1508 Ottley, C. J., 2015, Arc-related harzburgite-dunite-chromitite complexes in the  
1509 mantle section of the Sabzevar ophiolite, Iran: A model for formation of podiform  
1510 chromitites: *Gondwana Research*, v. 27, no. 2, p. 575-593.
- 1511 Moghadam, H. S., Li, X.-H., Santos, J. F., Stern, R. J., Griffin, W. L., Ghorbani, G., and  
1512 Sarebani, N., 2017b, Neoproterozoic magmatic flare-up along the N. margin of  
1513 Gondwana: The Taknar complex, NE Iran: *Earth and Planetary Science Letters*, v.  
1514 474, p. 83-96.
- 1515 Moghadam, H. S., and Stern, R. J., 2011, Geodynamic evolution of Upper Cretaceous  
1516 Zagros ophiolites: formation of oceanic lithosphere above a nascent subduction  
1517 zone: *Geological Magazine*, v. 148, no. 5-6, p. 762-801.
- 1518 -, 2015, Ophiolites of Iran: Keys to understanding the tectonic evolution of SW Asia: (II)  
1519 Mesozoic ophiolites: *Journal of Asian Earth Sciences*, v. 100, p. 31-59.
- 1520 Moghadam, H. S., Stern, R. J., Kimura, J. I., Hirahara, Y., Senda, R., and Miyazaki, T.,  
1521 2012, Hf-Nd isotope constraints on the origin of Dehshir Ophiolite, Central Iran:  
1522 *Island Arc*, v. 21, no. 3, p. 202-214.
- 1523 Moghadam, H. S., Stern, R. J., and Rahgoshay, M., 2010, The Dehshir ophiolite (central  
1524 Iran): Geochemical constraints on the origin and evolution of the Inner Zagros  
1525 ophiolite belt: *Geological Society of America Bulletin*, v. 122, no. 9-10, p. 1516-  
1526 1547.
- 1527 Monsef, I., Monsef, R., Mata, J., Zhang, Z., Pirouz, M., Rezaeian, M., Esmaeili, R., and  
1528 Xiao, W., 2018, Evidence for an early-MORB to fore-arc evolution within the  
1529 Zagros suture zone: Constraints from zircon U-Pb geochronology and  
1530 geochemistry of the Neyriz ophiolite (South Iran): *Gondwana Research*.
- 1531 Monsef, I., Rahgoshay, M., Mohajjel, M., and Moghadam, H. S., 2010, Peridotites from  
1532 the Khoy Ophiolitic Complex, NW Iran: Evidence of mantle dynamics in a supra-

- 1533 subduction-zone context: *Journal of Asian Earth Sciences*, v. 38, no. 3-4, p. 105-  
1534 120.
- 1535 Moritz, R., and Ghazban, F., 1996, Geological and fluid inclusion studies in the Muteh  
1536 gold district, Sanandaj-Sirjan zone, Isfahan Province, Iran: *Schweizerische*  
1537 *Mineralogische Und Petrographische Mitteilungen*, v. 76, no. 1, p. 85-89.
- 1538 Moritz, R., Ghazban, F., and Singer, B. S., 2006, Eocene gold ore formation at Muteh,  
1539 Sanandaj-Sirjan tectonic zone, western Iran: A result of late-stage extension and  
1540 exhumation of metamorphic basement rocks within the Zagros orogen: *Economic*  
1541 *Geology*, v. 101, no. 8, p. 1497-1524.
- 1542 Munker, C., Weyer, S., Scherer, E., and Mezger, K., 2001, Separation of high field strength  
1543 elements (Nb, Ta, Zr, Hf) and Lu from rock samples for MC-ICPMS  
1544 measurements: *Geochemistry, Geophysics, Geosystems*, v. 2.
- 1545 Nasrabad, M., Rossetti, F., Theye, T., and Vignaroli, G., 2011, Metamorphic history and  
1546 geodynamic significance of the Early Cretaceous Sabzevar granulites (Sabzevar  
1547 structural zone, NE Iran): *Solid Earth*, v. 2, no. 2, p. 219-243.
- 1548 Nicolas, A., 1989, *Structure of Ophiolites and Dynamics of Oceanic Lithosphere*,  
1549 Dordrecht, the Netherlands, Kluwer Academic Publishers, 367 p.:
- 1550 Nowell, G., Kempton, P., Noble, S., Fitton, J., Saunders, A., Mahoney, J., and Taylor, R.,  
1551 1998, High precision Hf isotope measurements of MORB and OIB by thermal  
1552 ionisation mass spectrometry: insights into the depleted mantle: *Chemical Geology*,  
1553 v. 149, no. 3, p. 211-233.
- 1554 Ohara, Y., Stern, R. J., Ishii, T., Yurimoto, H., and Yamazaki, T., 2002, Peridotites from  
1555 the Mariana Trough: first look at the mantle beneath an active back-arc basin:  
1556 *Contributions to Mineralogy and Petrology*, v. 143, no. 1, p. 1-18.
- 1557 Omidvar, M., Safari, A., Vaziri-Moghaddam, H., and Ghalavand, H., 2018, Foraminiferal  
1558 biostratigraphy of Upper Cretaceous (Campanian–Maastrichtian) sequences in the

- 1559 Peri-Tethys basin; Moghan area, NW Iran: *Journal of African Earth Sciences*, v.  
1560 140, p. 94-113.
- 1561 Omrani, H., Moazzen, M., Oberhansli, R., Altenberger, U., and Lange, M., 2013, The  
1562 Sabzevar blueschists of the North-Central Iranian micro-continent as remnants of  
1563 the Neotethys-related oceanic crust subduction: *International Journal of Earth  
1564 Sciences*, v. 102, no. 5, p. 1491-1512.
- 1565 Osozawa, S., Shinjo, R., Lo, C. H., Jahn, B. M., Hoang, N., Sasaki, M., Ishikawa, K., Kano,  
1566 H., Hoshi, H., Xenophontos, C., and Wakabayashi, J., 2012, Geochemistry and  
1567 geochronology of the Troodos ophiolite: An SSZ ophiolite generated by subduction  
1568 initiation and an extended episode of ridge subduction?: *Lithosphere*, v. 4, no. 6, p.  
1569 497-510.
- 1570 Ottley, C., Pearson, D., and Irvine, G., 2003, A routine method for the dissolution of  
1571 geological samples for the analysis of REE and trace elements via ICP-MS: *Plasma  
1572 source mass spectrometry: Applications and emerging technologies*, no. 288, p.  
1573 221.
- 1574 Pearce, J., Kempton, P., Nowell, G., and Noble, S., 1999, Hf-Nd element and isotope  
1575 perspective on the nature and provenance of mantle and subduction components in  
1576 Western Pacific arc-basin systems: *Journal of Petrology*, v. 40, no. 11, p. 1579-  
1577 1611.
- 1578 Pearce, J. A., 2008, Geochemical fingerprinting of oceanic basalts with applications to  
1579 ophiolite classification and the search for Archean oceanic crust: *Lithos*, v. 100, no.  
1580 1-4, p. 14-48.
- 1581 Pearce, J. A., Barker, P. F., Edwards, S. J., Parkinson, I. J., and Leat, P. T., 2000a,  
1582 Geochemistry and tectonic significance of peridotites from the South Sandwich arc-  
1583 basin system, South Atlantic: *Contributions to Mineralogy and Petrology*, v. 139,  
1584 no. 1, p. 36-53.

- 1585 Pearce, J. A., Barker, P. F., Edwards, S. J., Parkinson, I. J., and Leat, P. T., 2000b,  
1586 Geochemistry and tectonic significance of peridotites from the South Sandwich arc-  
1587 basin system, South Atlantic: *Contributions to Mineralogy and Petrology*, v. 139,  
1588 p. 36-53.
- 1589 Pearce, J. A., Harris, N. B. W., and Tindle, A. G., 1984, Trace-Element Discrimination  
1590 Diagrams for the Tectonic Interpretation of Granitic-Rocks: *Journal of Petrology*,  
1591 v. 25, no. 4, p. 956-983.
- 1592 Pearce, J. A., and Peate, D. W., 1995, Tectonic Implications of the Composition of  
1593 Volcanic Arc Magmas: *Annual Review of Earth and Planetary Sciences*, v. 23, p.  
1594 251-285.
- 1595 Pearce, J. A., and Robinson, P. T., 2010, The Troodos ophiolitic complex probably formed  
1596 in a subduction initiation, slab edge setting: *Gondwana Research*, v. 18, no. 1, p.  
1597 60-81.
- 1598 Peate, D. W., and Pearce, J. A., 1998, Causes of spatial compositional variations in Mariana  
1599 arc lavas: Trace element evidence: *Island Arc*, v. 7, no. 3, p. 479-495.
- 1600 Pin, C., and Zalduegui, J. F. S., 1997, Sequential separation of light rare-earth elements,  
1601 thorium and uranium by miniaturized extraction chromatography: Application to  
1602 isotopic analyses of silicate rocks: *Analytica Chimica Acta*, v. 339, p. 79-89.
- 1603 Pirnia, T., Arai, S., Tamura, A., Ishimaru, S., and Torabi, G., 2014, Sr enrichment in mantle  
1604 pyroxenes as a result of plagioclase alteration in lherzolite: *Lithos*, v. 196, p. 198-  
1605 212.
- 1606 Potts, P. J., Tindle, A. G., and Webb, P., 1992, Geochemical reference material  
1607 compositions: rocks, minerals, sediments, soils, carbonates, refractories & ores  
1608 used in research & industry, Taylor & Francis.
- 1609 Reagan, M. K., Ishizuka, O., Stern, R. J., Kelley, K. A., Ohara, Y., Blichert-Toft, J.,  
1610 Bloomer, S. H., Cash, J., Fryer, P., Hanan, B. B., Hickey-Vargas, R., Ishii, T.,  
1611 Kimura, J. I., Peate, D. W., Rowe, M. C., and Woods, M., 2010, Fore-arc basalts

- 1612 and subduction initiation in the Izu-Bonin-Mariana system: *Geochemistry*  
1613 *Geophysics Geosystems*, v. 11.
- 1614 Robinson, P. T., Trumbull, R. B., Schmitt, A., Yang, J. S., Li, J. W., Zhou, M. F., Erzinger,  
1615 J., Dare, S., and Xiong, F. H., 2015, The origin and significance of crustal minerals  
1616 in ophiolitic chromitites and peridotites: *Gondwana Research*, v. 27, no. 2, p. 486-  
1617 506.
- 1618 Ross, K., and Elthon, D., 1993, Cumulates from strongly depleted mid-ocean-ridge basalt:  
1619 *Nature*, v. 365, no. 6449, p. 826.
- 1620 Rossetti, F., Nasrabady, M., Theye, T., Gerdes, A., Monie, P., Lucci, F., and Vignaroli, G.,  
1621 2014, Adakite differentiation and emplacement in a subduction channel: The late  
1622 Paleocene Sabzevar magmatism (NE Iran): *Geological Society of America*  
1623 *Bulletin*, v. 126, no. 3-4, p. 317-343.
- 1624 Rossetti, F., Nasrabady, M., Vignaroli, G., Theye, T., Gerdes, A., Razavi, M. H., and  
1625 Vaziri, H. M., 2010, Early Cretaceous migmatitic mafic granulites from the  
1626 Sabzevar range (NE Iran): implications for the closure of the Mesozoic peri-  
1627 Tethyan oceans in central Iran: *Terra Nova*, v. 22, no. 1, p. 26-34.
- 1628 Saccani, E., Allahyari, K., Beccaluva, L., and Bianchini, G., 2013, *Geochemistry and*  
1629 *petrology of the Kermanshah ophiolites (Iran): Implication for the interaction*  
1630 *between passive rifting, oceanic accretion, and OIB-type components in the*  
1631 *Southern Neo-Tethys Ocean: Gondwana Research*, v. 24, no. 1, p. 392-411.
- 1632 Saccani, E., Bortolotti, V., Marroni, M., Pandolfi, L., Photiades, A., and Principi, G., 2008,  
1633 *The Jurassic Association of Backarc Basin Ophiolites and Calc-Alkaline Volcanics*  
1634 *in the Guevgueli Complex (Northern Greece): Implication for the Evolution of the*  
1635 *Vardar Zone: Ofioliti*, v. 33, no. 2, p. 209-227.
- 1636 Sandeman, H. A., Hanmer, S., Tella, S., Armitage, A. A., Davis, W. J., and Ryan, J. J.,  
1637 2006, *Petrogenesis of Neoproterozoic volcanic rocks of the MacQuoid supracrustal*

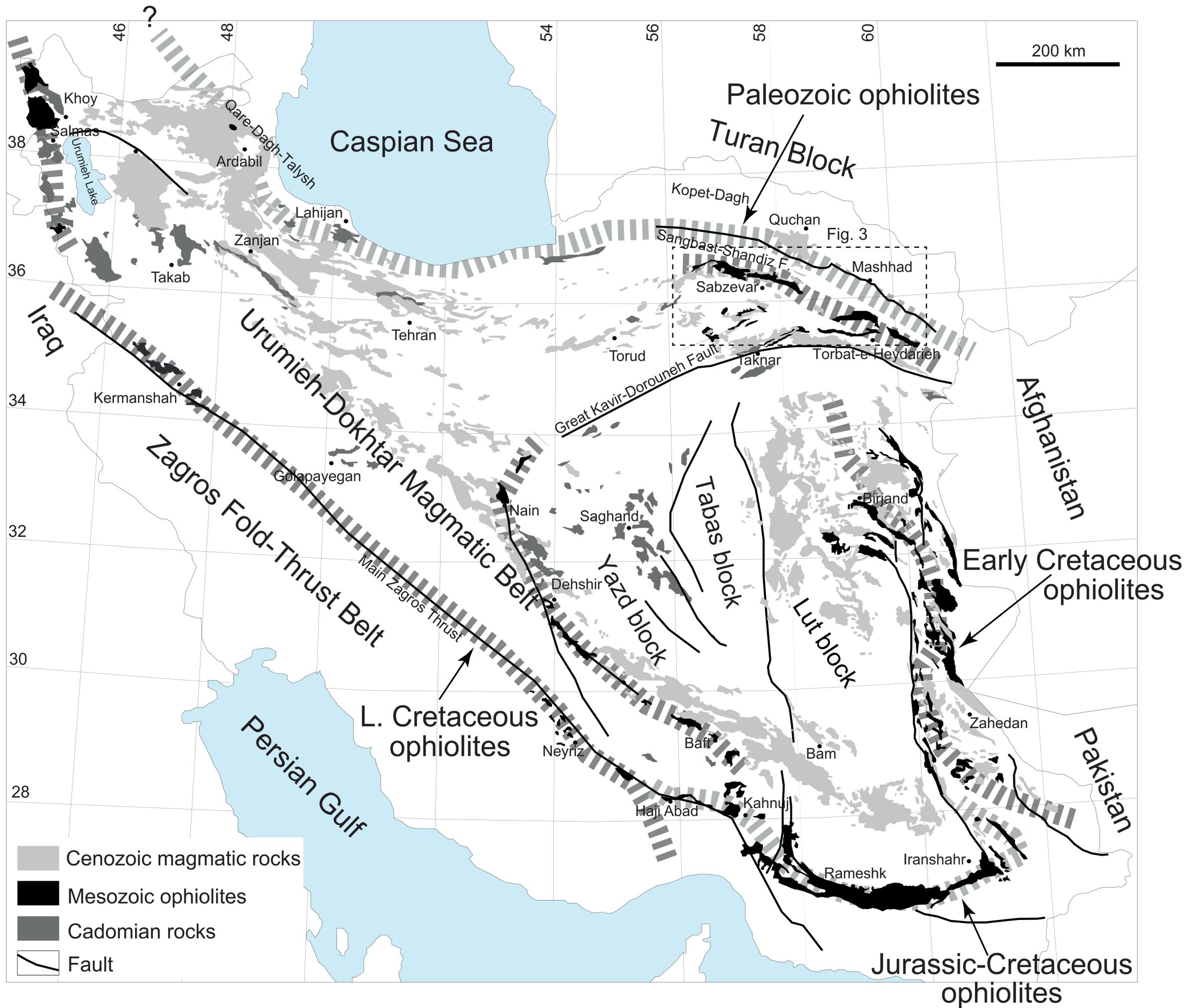
- 1638 belt: A back-arc setting for the northwestern Hearne subdomain, western Churchill  
1639 Province, Canada: *Precambrian Research*, v. 144, no. 1-2, p. 140-165.
- 1640 Sanfilippo, A., Dick, H. J. B., and Ohara, Y., 2013, Melt-Rock Reaction in the Mantle:  
1641 Mantle Troctolites from the Parece Vela Ancient Back-Arc Spreading Center:  
1642 *Journal of Petrology*, v. 54, no. 5, p. 861-885.
- 1643 Sarifakioglu, E., Ozen, H., and Winchester, J. A., 2009, Petrogenesis of the Refahiye  
1644 Ophiolite and its Tectonic Significance for Neotethyan Ophiolites Along the Izmir-  
1645 Ankara-Erzincan Suture Zone: *Turkish Journal of Earth Sciences*, v. 18, no. 2, p.  
1646 187-207.
- 1647 Shafaii Moghadam, H., Zaki Khedr, M., Arai, S., Stern, R. J., Ghorbani, G., Tamura, A.,  
1648 and Ottley, C. J., 2015, Arc-related harzburgite–dunite–chromitite complexes in the  
1649 mantle section of the Sabzevar ophiolite, Iran: A model for formation of podiform  
1650 chromitites: *Gondwana Research*, v. 27, no. 2, p. 575-593.
- 1651 Shaw, S. E., and Flood, R. H., 2009, Zircon Hf Isotopic Evidence for Mixing of Crustal  
1652 and Silicic Mantle-derived Magmas in a Zoned Granite Pluton, Eastern Australia:  
1653 *Journal of Petrology*, v. 50, no. 1, p. 147-168.
- 1654 Shervais, J. W., 1982, Ti-V plots and the petrogenesis of modern and ophiolitic lavas: *Earth  
1655 and planetary science letters*, v. 59, no. 1, p. 101-118.
- 1656 Shinjo, R., 1999, Geochemistry of high Mg andesites and the tectonic evolution of the  
1657 Okinawa Trough Ryukyu arc system: *Chemical Geology*, v. 157, no. 1-2, p. 69-88.
- 1658 Shinjo, R., Chung, S. L., Kato, Y., and Kimura, M., 1999, Geochemical and Sr - Nd  
1659 isotopic characteristics of volcanic rocks from the Okinawa Trough and Ryukyu  
1660 Arc: Implications for the evolution of a young, intracontinental back arc basin:  
1661 *Journal of Geophysical Research: Solid Earth*, v. 104, no. B5, p. 10591-10608.

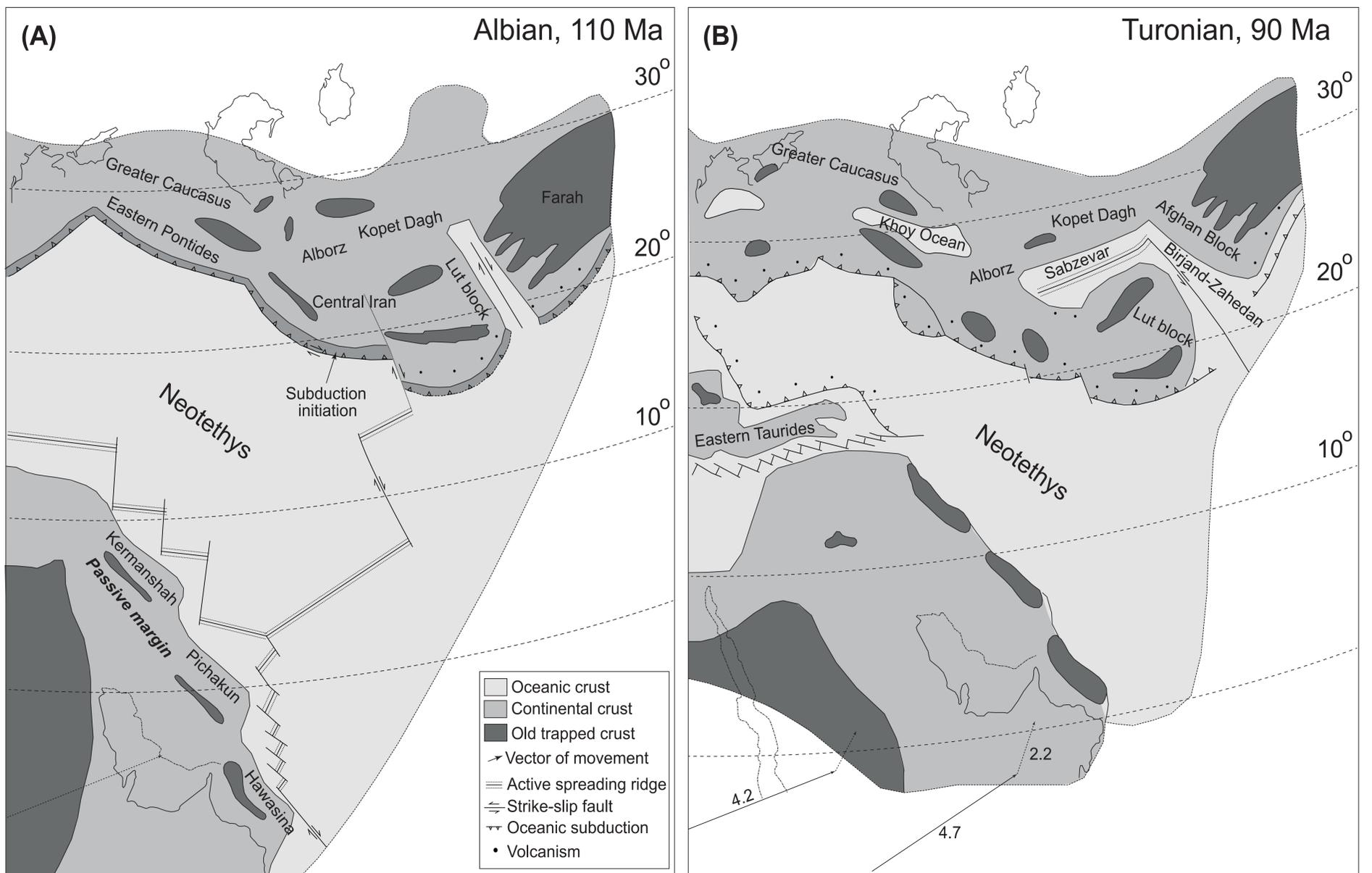
- 1662 Shojaat, B., Hassanipak, A. A., Mobasher, K., and Ghazi, A. M., 2003, Petrology,  
1663 geochemistry and tectonics of the Sabzevar ophiolite, North Central Iran: *Journal*  
1664 *of Asian Earth Sciences*, v. 21, no. 9, p. 1053-1067.
- 1665 Sorbadere, F., Schiano, P., Metrich, N., and Bertagnini, A., 2013, Small-scale coexistence  
1666 of island-arc- and enriched-MORB-type basalts in the central Vanuatu arc:  
1667 *Contributions to Mineralogy and Petrology*, v. 166, no. 5, p. 1305-1321.
- 1668 Stern, R. J., 2002, Subduction zones: *Reviews of Geophysics*, v. 40, no. 4.
- 1669 Stern, R. J., 2004, Subduction initiation: spontaneous and induced: *Earth and Planetary*  
1670 *Science Letters*, v. 226, no. 3-4, p. 275-292.
- 1671 Stern, R. J., and Dickinson, W. R., 2010, The Gulf of Mexico is a Jurassic backarc basin:  
1672 *Geosphere*, v. 6, no. 6, p. 739-754.
- 1673 Stern, R. J., and Gerya, T., 2017, Subduction initiation in nature and models: A review:  
1674 *Tectonophysics*.
- 1675 Stracke, A., Hofmann, A. W., and Hart, S. R., 2005, FOZO, HIMU, and the rest of the  
1676 mantle zoo: *Geochemistry Geophysics Geosystems*, v. 6.
- 1677 Tadayon, M., Rossetti, F., Zattin, M., Calzolari, G., Nozaem, R., Salvini, F., Faccenna, C.,  
1678 and Khodabakhshi, P., 2018, The long - term evolution of the Doruneh Fault region  
1679 (Central Iran): A key to understanding the spatio - temporal tectonic evolution in  
1680 the hinterland of the Zagros convergence zone: *Geological Journal*, p. 1-26.
- 1681 Tadayon, M., Rossetti, F., Zattin, M., Nozaem, R., Calzolari, G., Madanipour, S., and  
1682 Salvini, F., 2017, The Post-Eocene Evolution of the Doruneh Fault Region (Central  
1683 Iran): The Intraplate Response to the Reorganization of the Arabia-Eurasia  
1684 Collision Zone: *Tectonics*, v. 36, p. 3038-3064.
- 1685 Taylor, B., and Martinez, F., 2003, Back-arc basin basalt systematics: *Earth and Planetary*  
1686 *Science Letters*, v. 210, no. 3-4, p. 481-497.

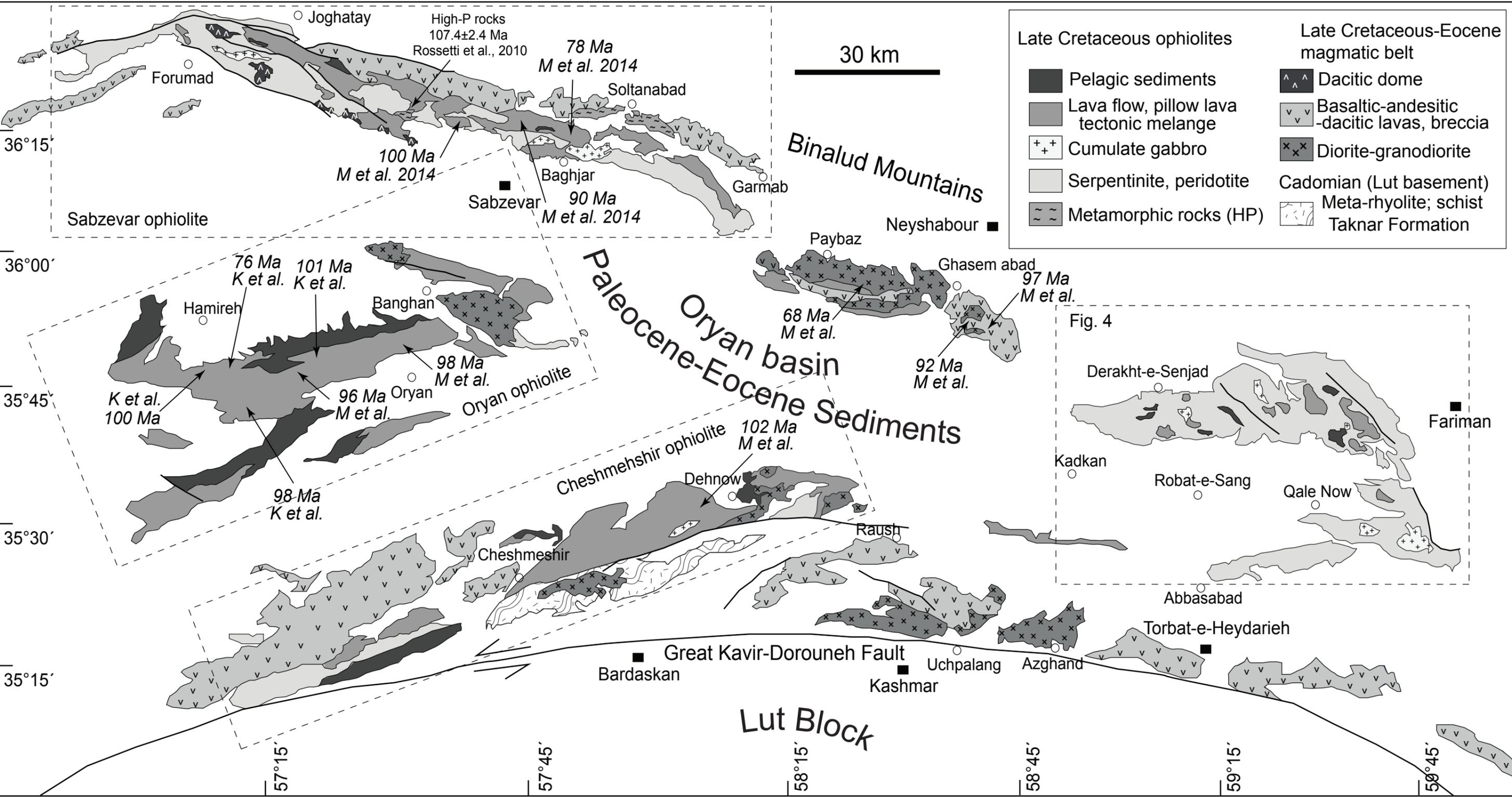
- 1687 Thomas, J.-C., Grasso, J.-R., Bossu, R., Martinod, J., and Nurtaev, B., 1999, Recent  
1688 deformation in the Turan and South Kazakh platforms, western central Asia, and  
1689 its relation to Arabia-Asia and India-Asia collisions: *Tectonics*, v. 18, no. 2, p. 201-  
1690 214.
- 1691 Tian, L. Y., Castillo, P. R., Hilton, D. R., Hawkins, J. W., Hanan, B. B., and Pietruszka, A.  
1692 J., 2011, Major and trace element and Sr-Nd isotope signatures of the northern Lau  
1693 Basin lavas: Implications for the composition and dynamics of the back-arc basin  
1694 mantle: *Journal of Geophysical Research-Solid Earth*, v. 116.
- 1695 Tiepolo, M., Oberti, R., Zanetti, A., Vannucci, R., and Foley, S. F., 2007, Trace-element  
1696 partitioning between amphibole and silicate melt: *Reviews in mineralogy and  
1697 geochemistry*, v. 67, no. 1, p. 417-452.
- 1698 Todd, E., Gill, J. B., Wysoczanski, R. J., Hergt, J., Wright, I. C., Leybourne, M. I., and  
1699 Mortimer, N., 2011, Hf isotopic evidence for small-scale heterogeneity in the mode  
1700 of mantle wedge enrichment: Southern Havre Trough and South Fiji Basin back  
1701 arcs: *Geochemistry Geophysics Geosystems*, v. 12.
- 1702 Uner, T., Cakir, U., Ozdemir, Y., and Arat, I., 2014, Geochemistry and origin of  
1703 plagiogranites from the Eldivan Ophiolite, Cankiri (Central Anatolia, Turkey):  
1704 *Geologica Carpathica*, v. 65, no. 3, p. 195-205.
- 1705 Vaezi Pour, M. J., Alavi Tehrani, N., Behrouzi, A., and Kholghi, M. H., 1992, Geological  
1706 Map of the Torbat-e-Heydarieh: Geological Survey of Iran.
- 1707 van Hinsbergen, D. J. J., Peters, K., Maffione, M., Spakman, W., Guilmette, C., Thieulot,  
1708 C., Plumper, O., Gurer, D., Brouwer, F. M., Aldanmaz, E., and Kaymakci, N., 2015,  
1709 Dynamics of intraoceanic subduction initiation: 2. Suprasubduction zone ophiolite  
1710 formation and metamorphic sole exhumation in context of absolute plate motions:  
1711 *Geochemistry Geophysics Geosystems*, v. 16, no. 6, p. 1771-1785.
- 1712 Verdel, C., Wernicke, B. P., Hassanzadeh, J., and Guest, B., 2011, A Paleogene extensional  
1713 arc flare-up in Iran: *Tectonics*, v. 30.

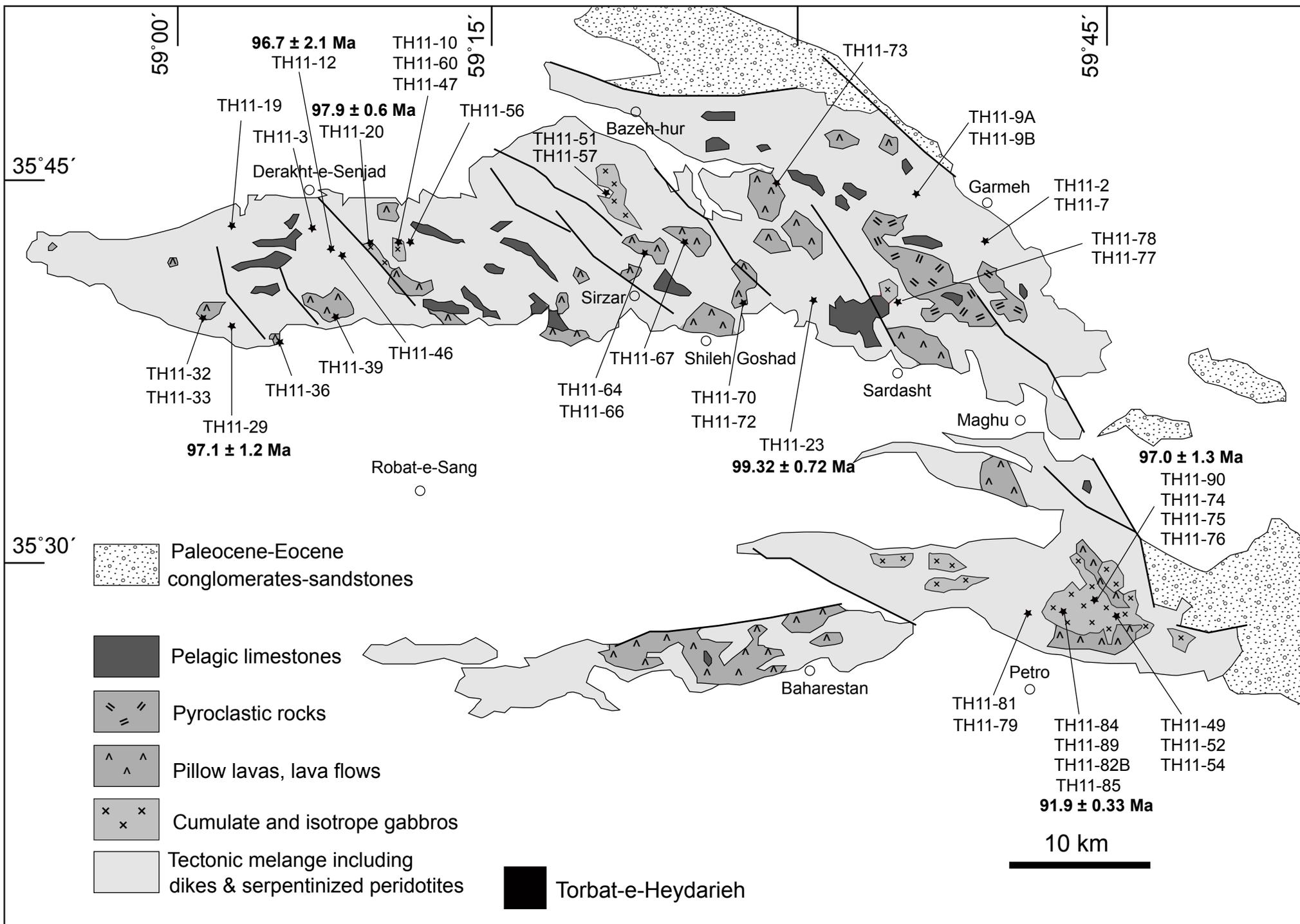
- 1714 Verdel, C., Wernicke, B. P., Ramezani, J., Hassanzadeh, J., Renne, P. R., and Spell, T. L.,  
1715 2007, Geology and thermochronology of Tertiary Cordilleran-style metamorphic  
1716 core complexes in the Saghand region of central Iran: Geological Society of  
1717 America Bulletin, v. 119, no. 7-8, p. 961-977.
- 1718 Vervoort, J. D., and Blichert-Toft, J., 1999a, Evolution of the depleted mantle: Hf isotope  
1719 evidence from juvenile rocks through time: *Geochimica et Cosmochimica Acta*, v.  
1720 63, no. 3, p. 533-556.
- 1721 Vervoort, J. D., and Blichert-Toft, J., 1999b, Evolution of the depleted mantle: Hf isotope  
1722 evidence from juvenile rocks through time: *Geochimica Et Cosmochimica Acta*, v.  
1723 63, no. 3-4, p. 533-556.
- 1724 Vervoort, J. D., Patchett, P. J., Blichert-Toft, J., and Albarede, F., 1999, Relationships  
1725 between Lu-Hf and Sm-Nd isotopic systems in the global sedimentary system:  
1726 *Earth and Planetary Science Letters*, v. 168, no. 1-2, p. 79-99.
- 1727 Whattam, S. A., and Stern, R. J., 2011, The 'subduction initiation rule': a key for linking  
1728 ophiolites, intra-oceanic forearcs, and subduction initiation: *Contributions to*  
1729 *Mineralogy and Petrology*, v. 162, no. 5, p. 1031-1045.
- 1730 Woodhead, J., Hergt, J., Davidson, J., and Eggins, S., 2001, Hafnium isotope evidence for  
1731 'conservative' element mobility during subduction zone processes: *Earth and*  
1732 *Planetary Science Letters*, v. 192, no. 3, p. 331-346.
- 1733 Woodhead, J., Stern, R. J., Pearce, J., Hergt, J., and Vervoort, J., 2012, Hf-Nd isotope  
1734 variation in Mariana Trough basalts: The importance of "ambient mantle" in the  
1735 interpretation of subduction zone magmas: *Geology*, v. 40, no. 6, p. 539-542.
- 1736 Woodhead, J. D., and Devey, C. W., 1993, Geochemistry of the Pitcairn Seamounts .1.  
1737 Source Character and Temporal Trends: *Earth and Planetary Science Letters*, v.  
1738 116, no. 1-4, p. 81-99.

- 1739 Woodhead, J. D., and Hergt, J. M., 2005, A preliminary appraisal of seven natural zircon  
1740 reference materials for in situ Hf isotope determination: *Geostandards and*  
1741 *Geoanalytical Research*, v. 29, no. 2, p. 183-195.
- 1742 Yogodzinski, G. M., Vervoort, J. D., Brown, S. T., and Gersen, M., 2010, Subduction  
1743 controls of Hf and Nd isotopes in lavas of the Aleutian island arc: *Earth and*  
1744 *Planetary Science Letters*, v. 300, no. 3-4, p. 226-238.
- 1745 Yuan, H. L., Gao, S., Dai, M. N., Zong, C. L., Gunther, D., Fontaine, G. H., Liu, X. M.,  
1746 and Diwu, C., 2008, Simultaneous determinations of U-Pb age, Hf isotopes and  
1747 trace element compositions of zircon by excimer laser-ablation quadrupole and  
1748 multiple-collector ICP-MS: *Chemical Geology*, v. 247, no. 1-2, p. 100-118.
- 1749 Zarrinkoub, M. H., Pang, K. N., Chung, S. L., Khatib, M. M., Mohammadi, S. S., Chiu, H.  
1750 Y., and Lee, H. Y., 2012, Zircon U-Pb age and geochemical constraints on the  
1751 origin of the Birjand ophiolite, Sistan suture zone, eastern Iran: *Lithos*, v. 154, p.  
1752 392-405.  
1753

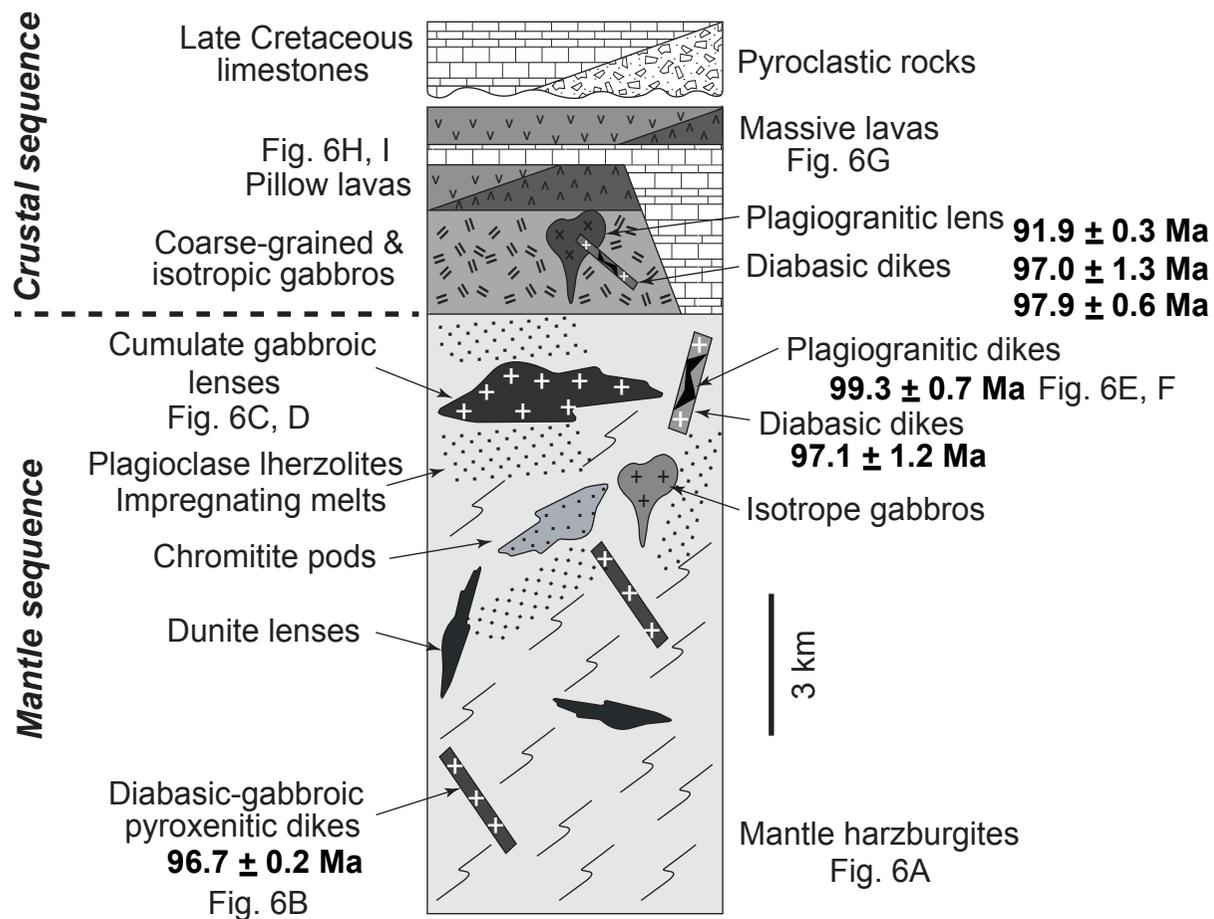


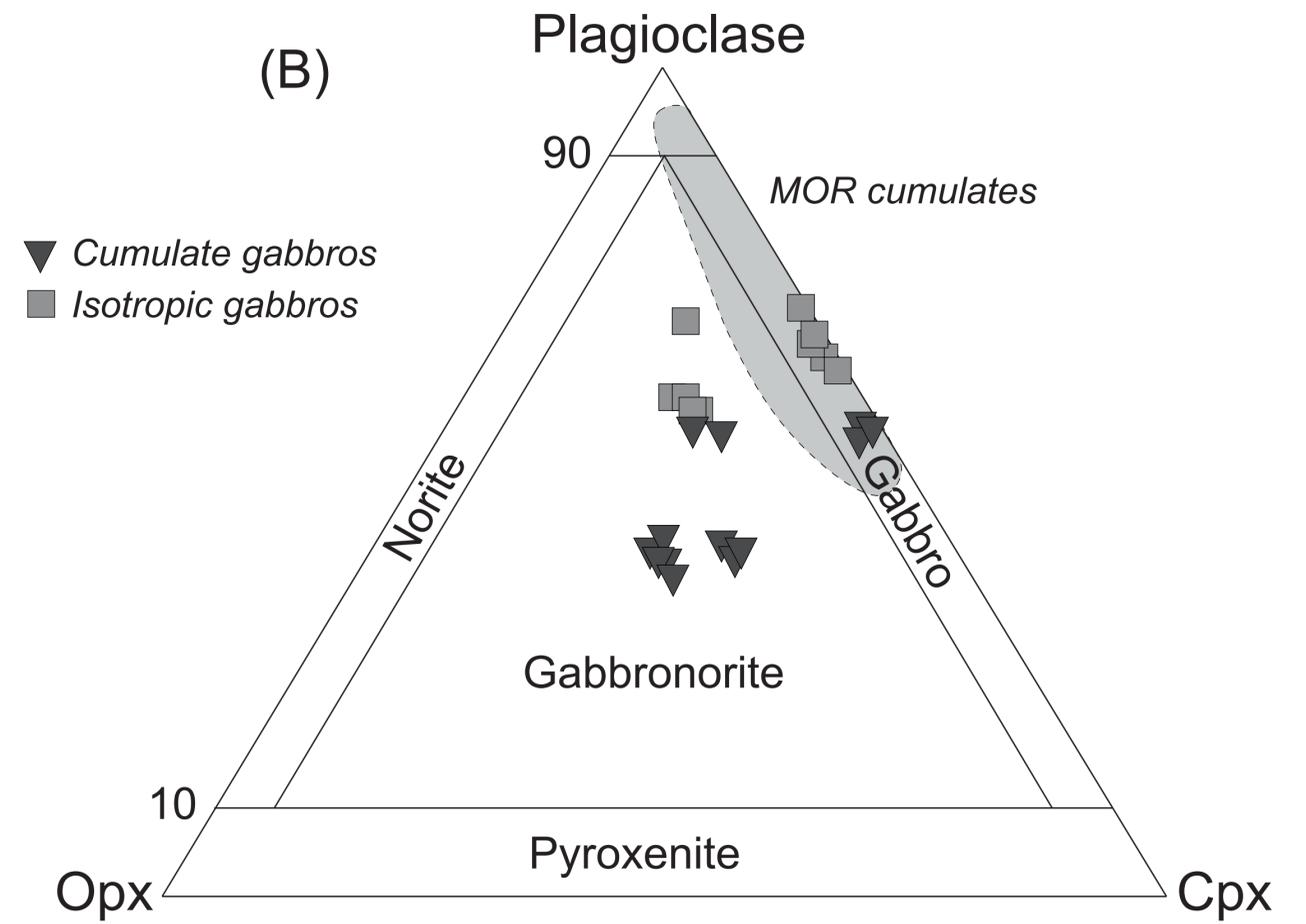
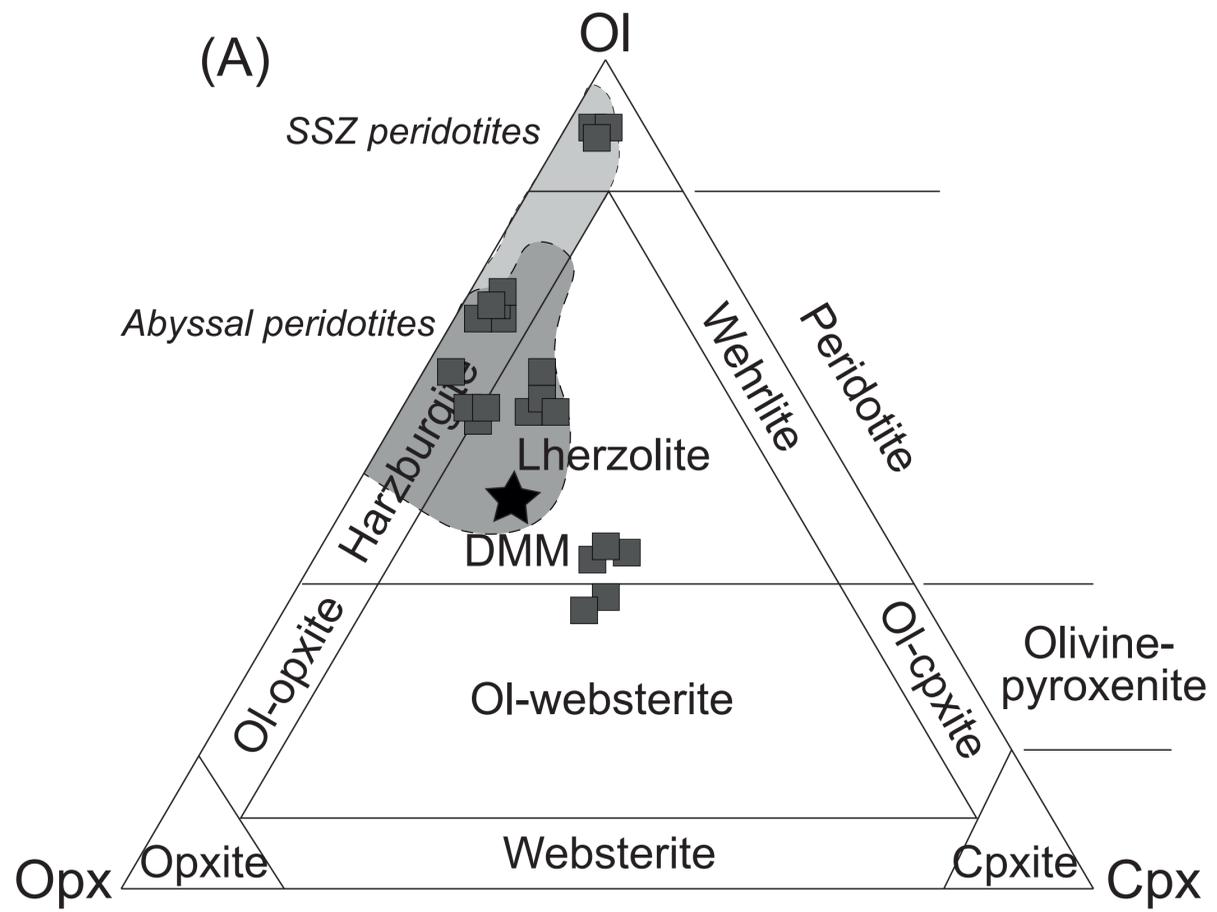


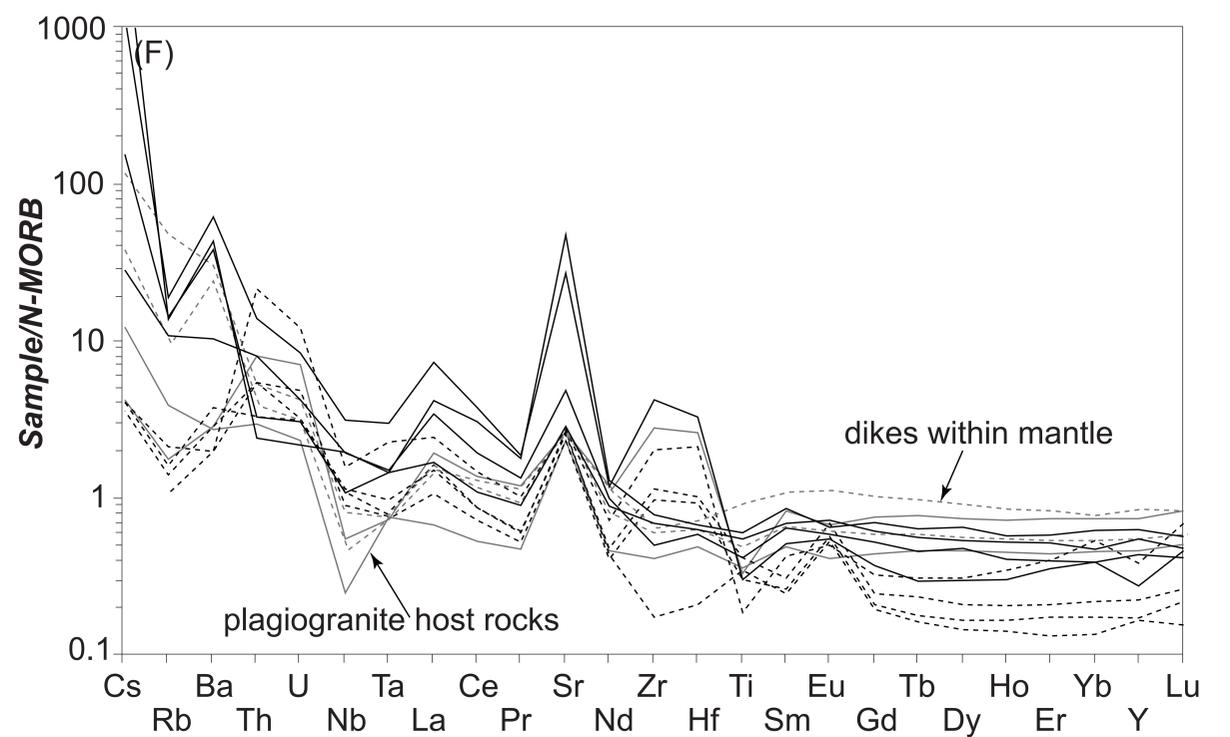
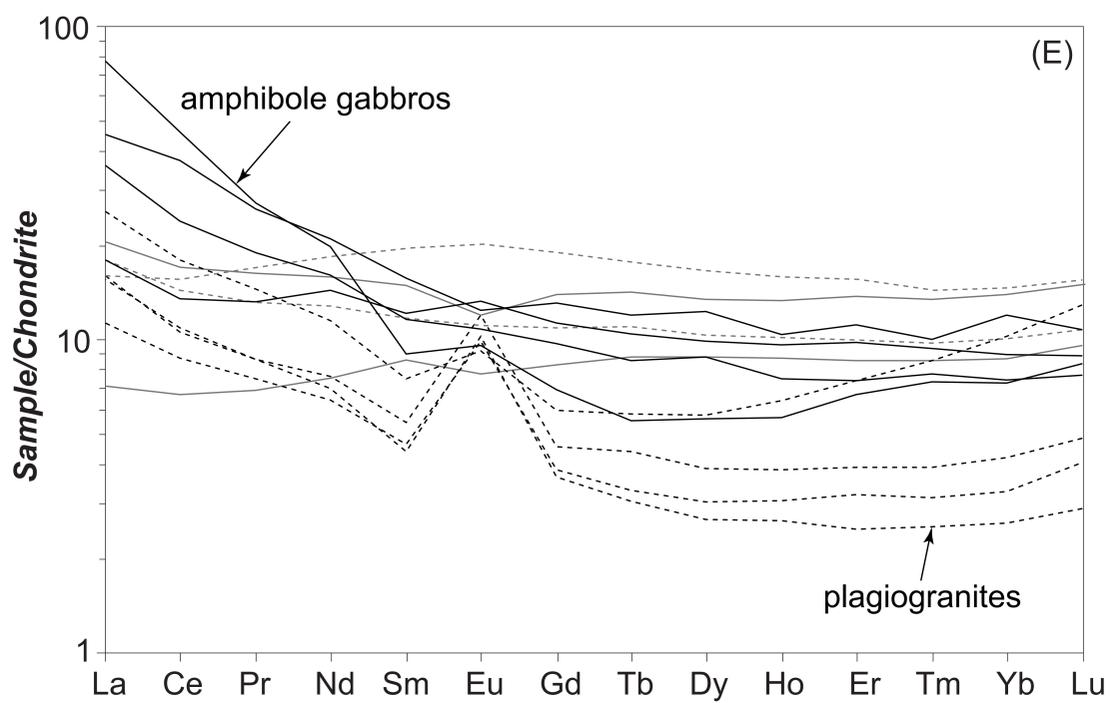
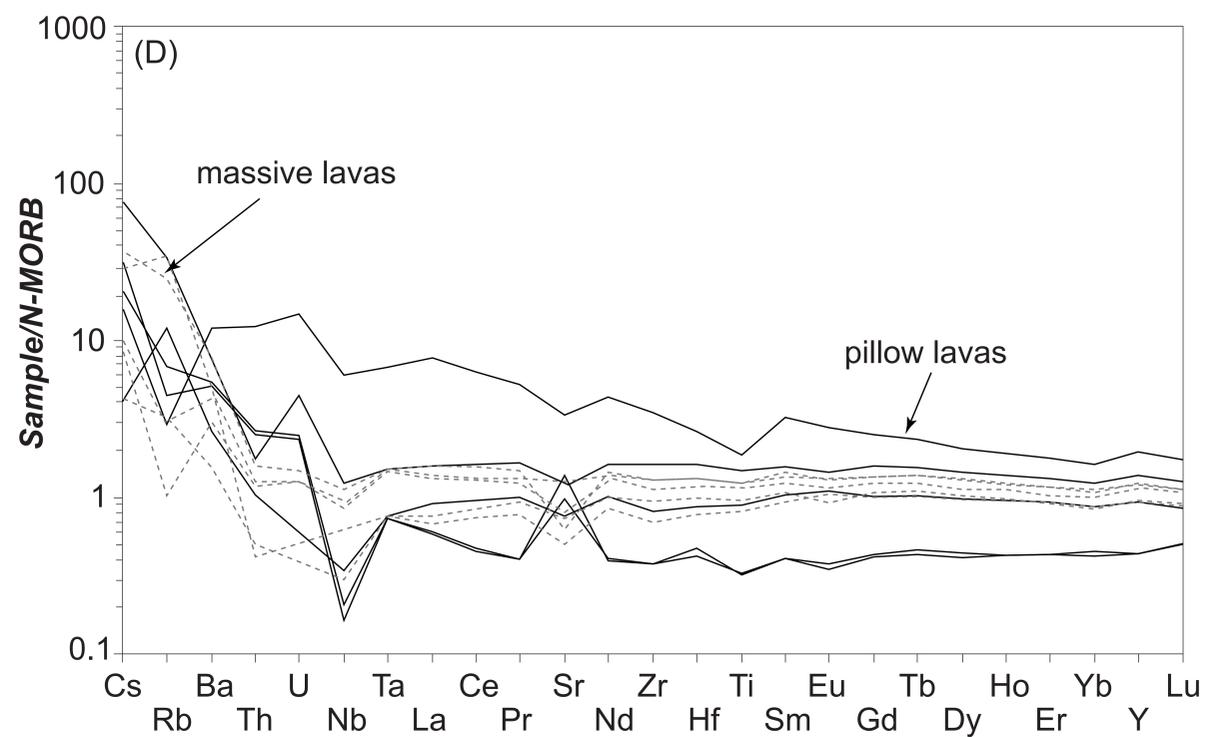
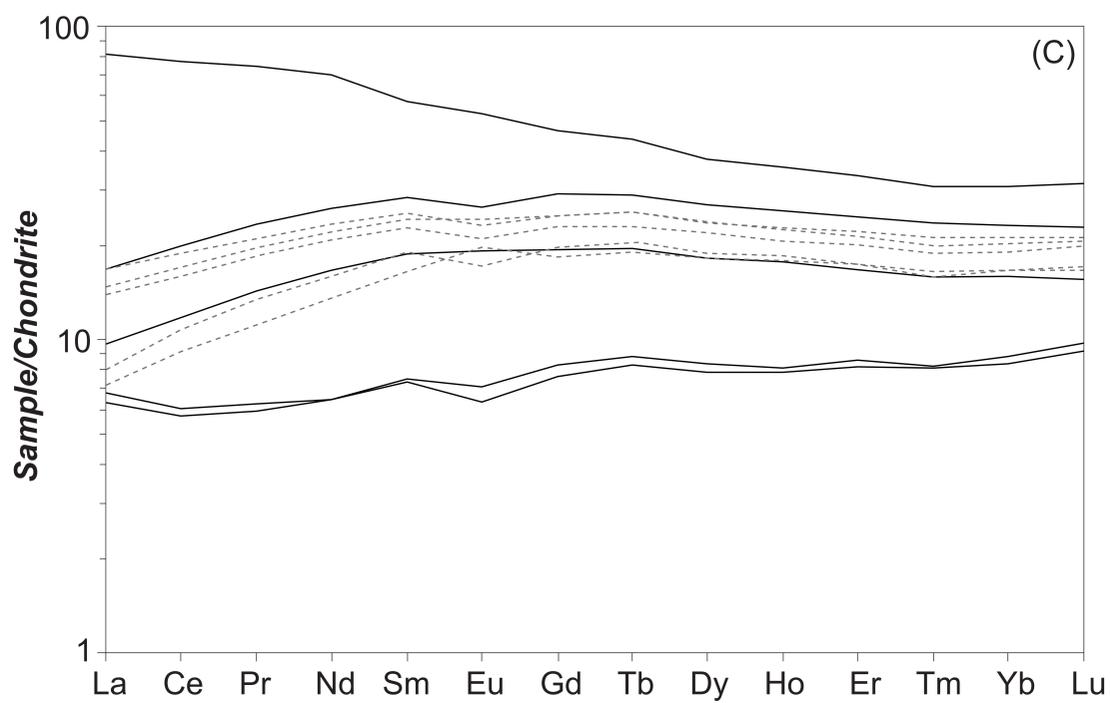
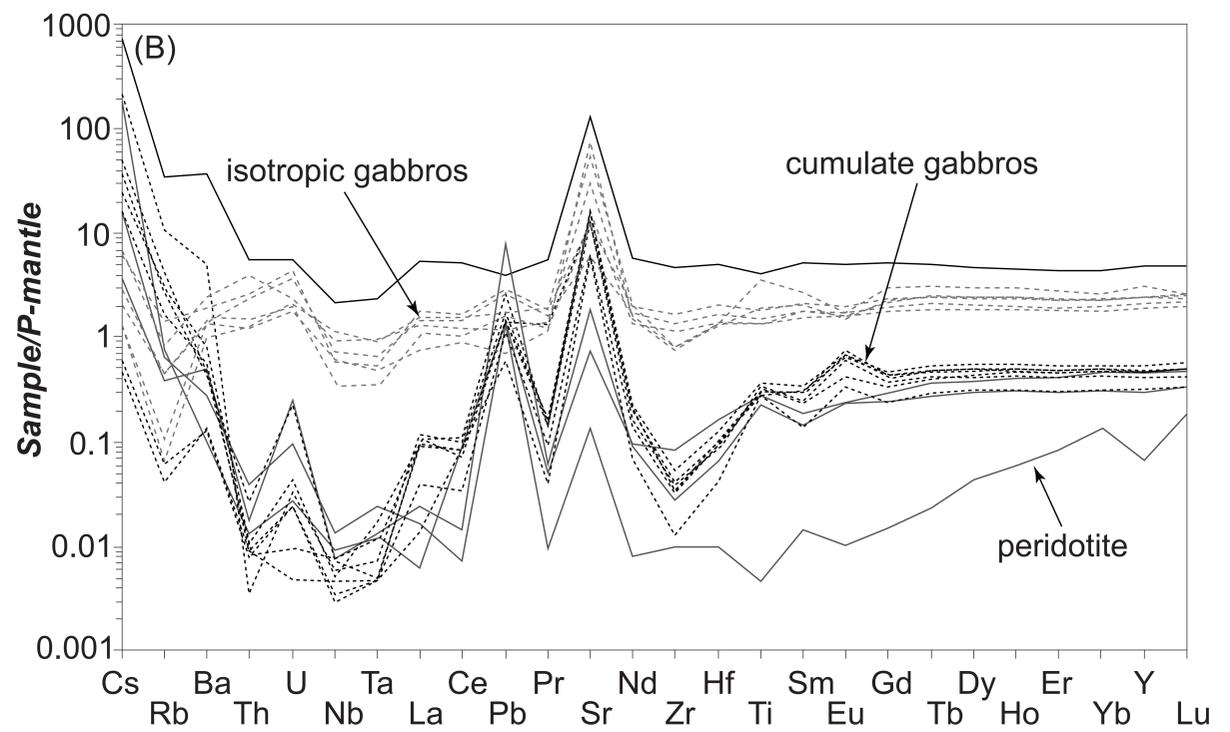
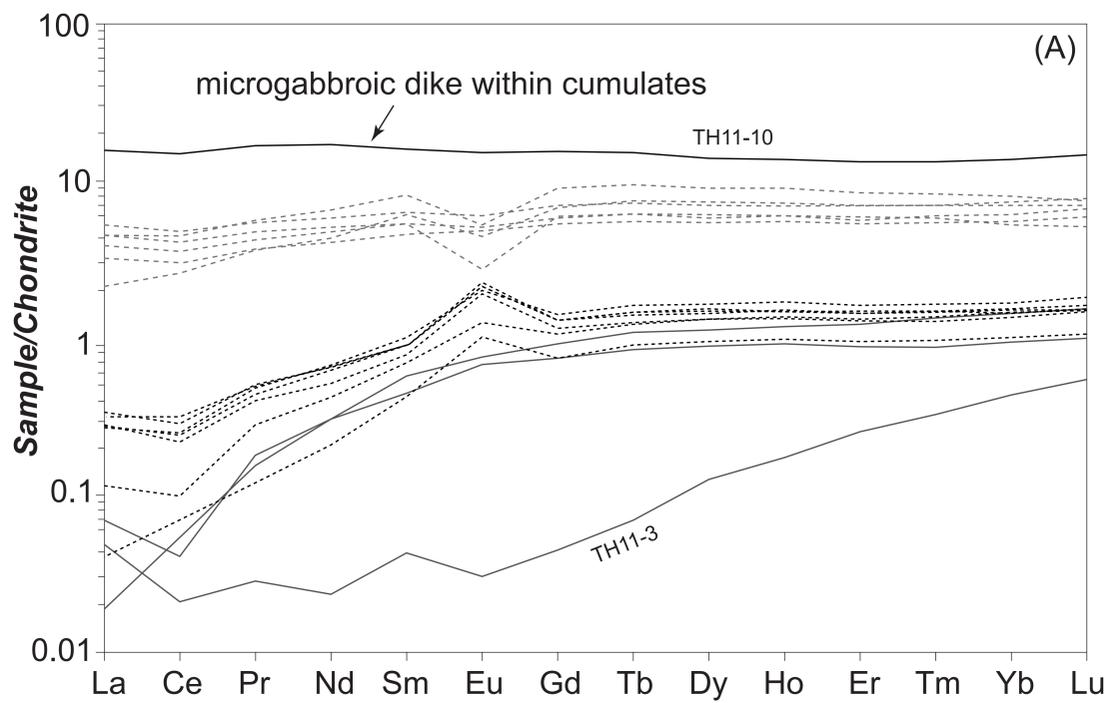


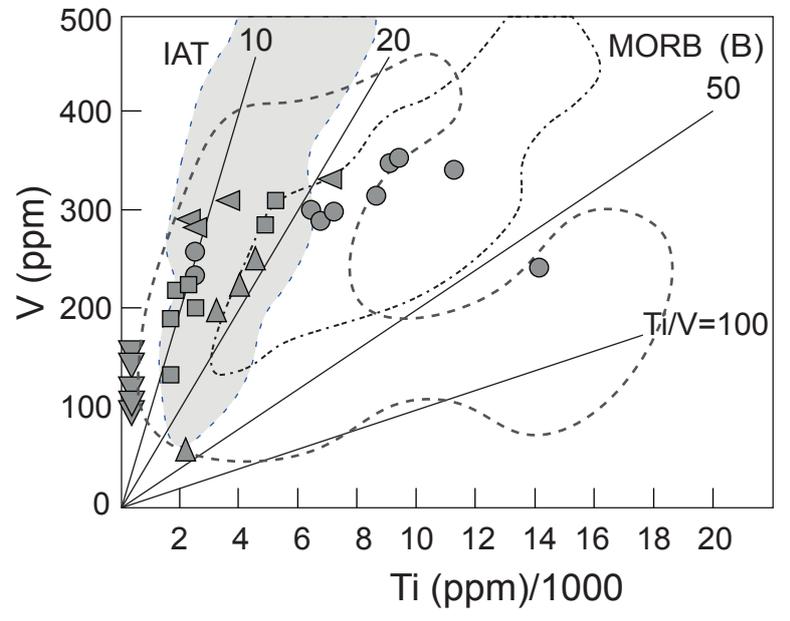
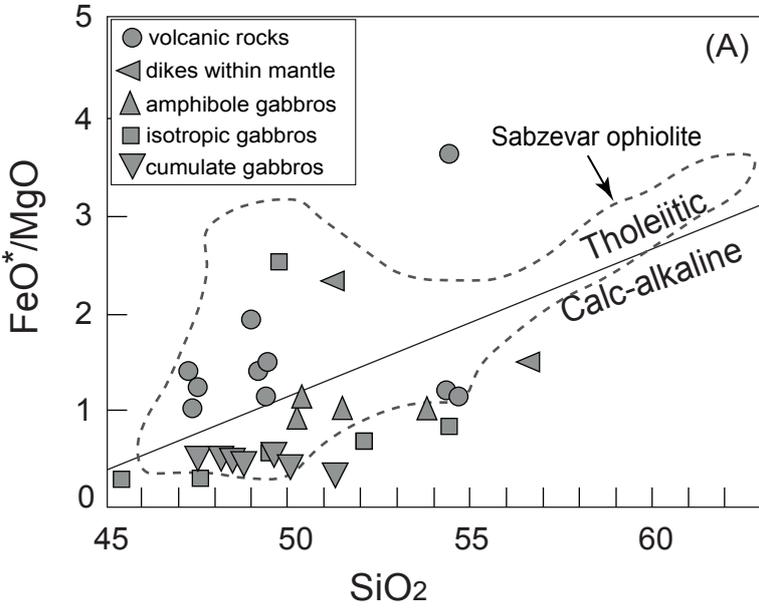


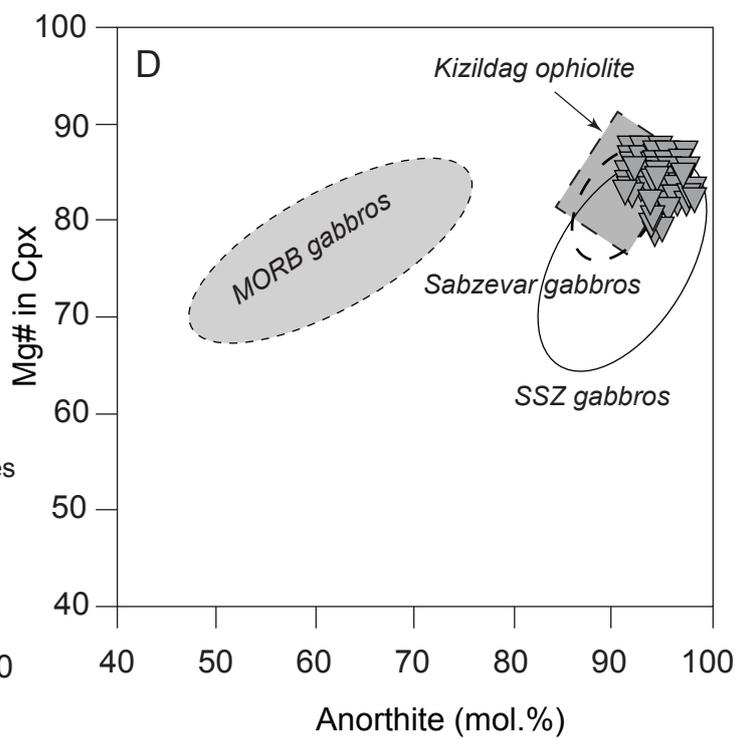
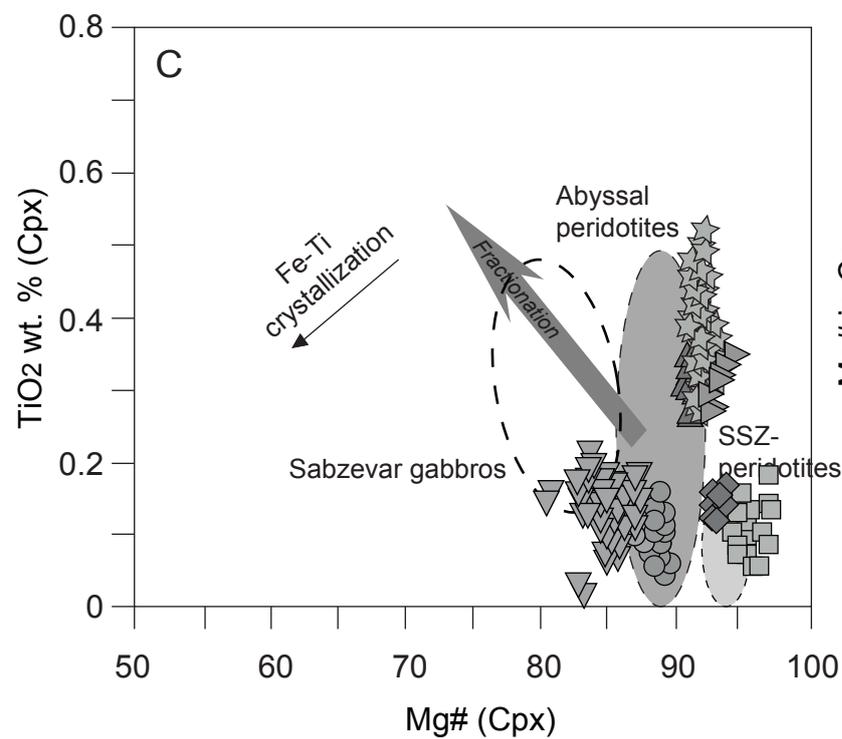
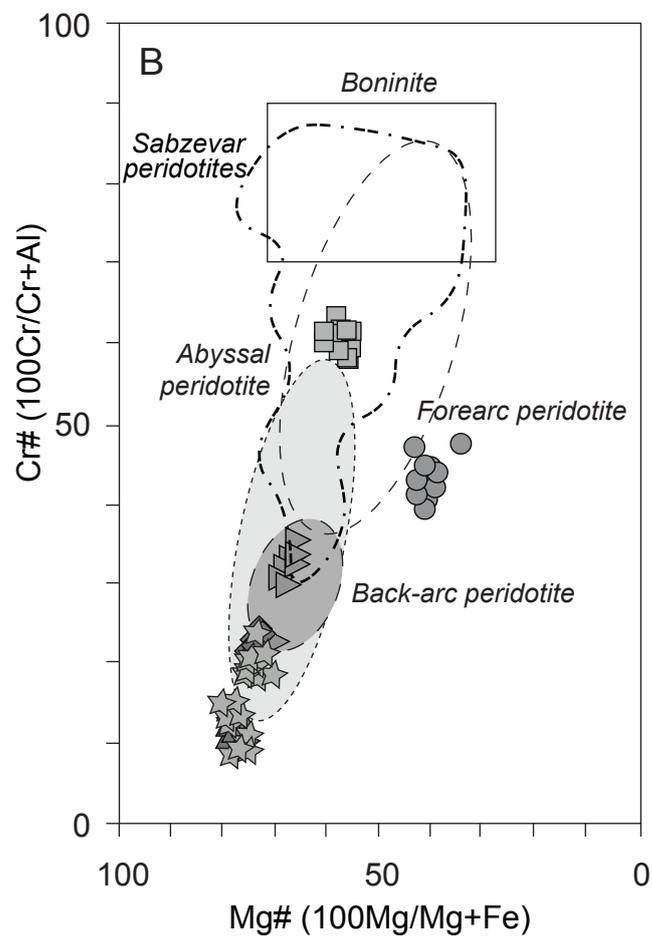
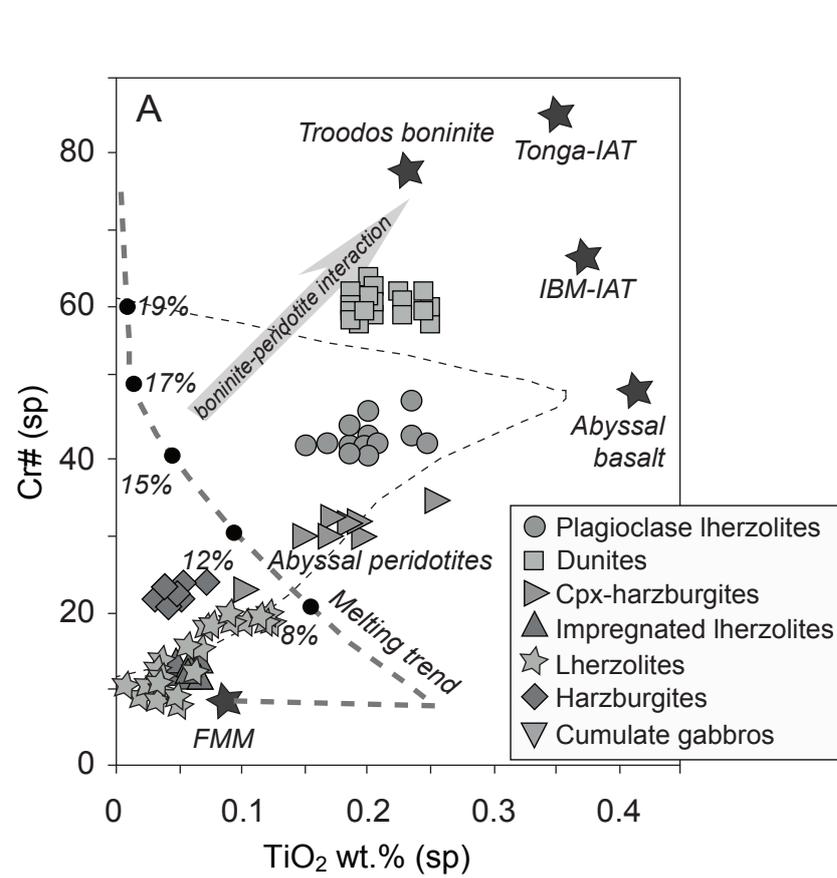
## Torbat-e-Heydarieh ophiolite

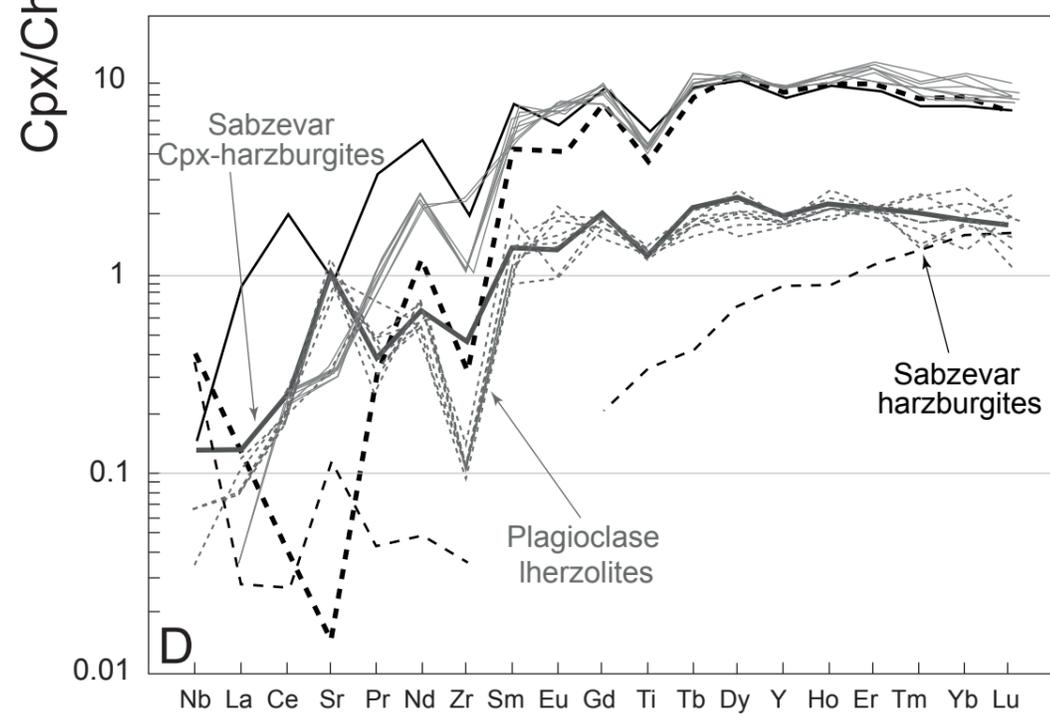
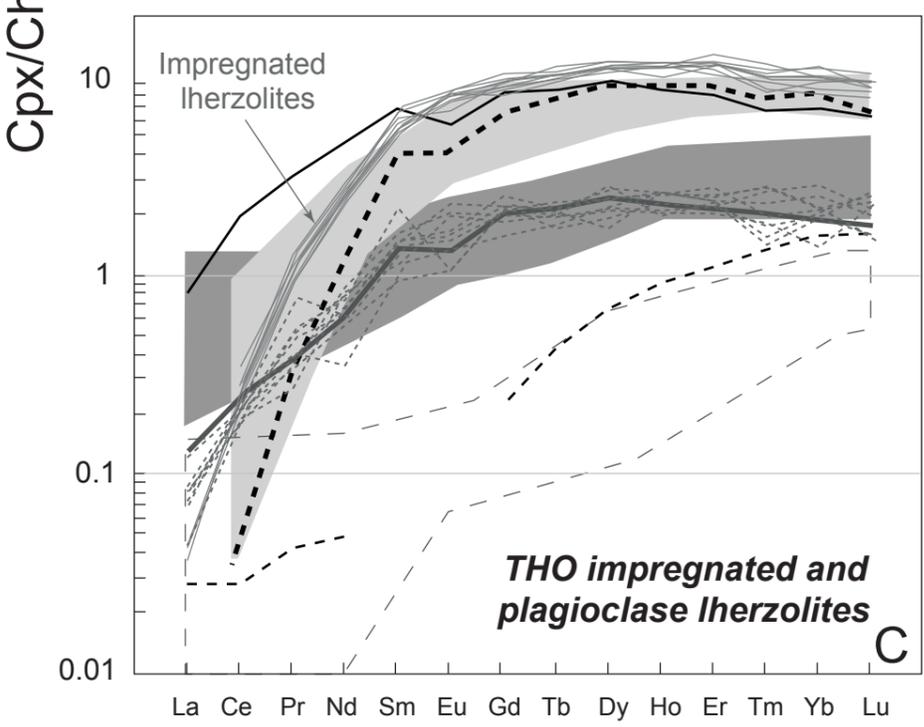
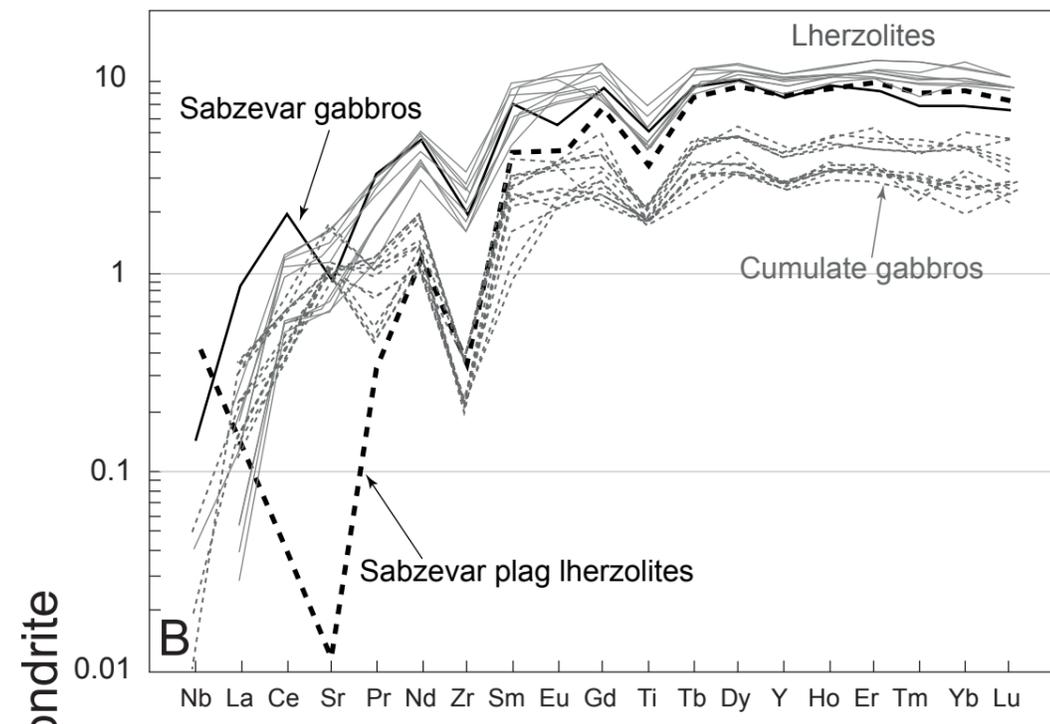
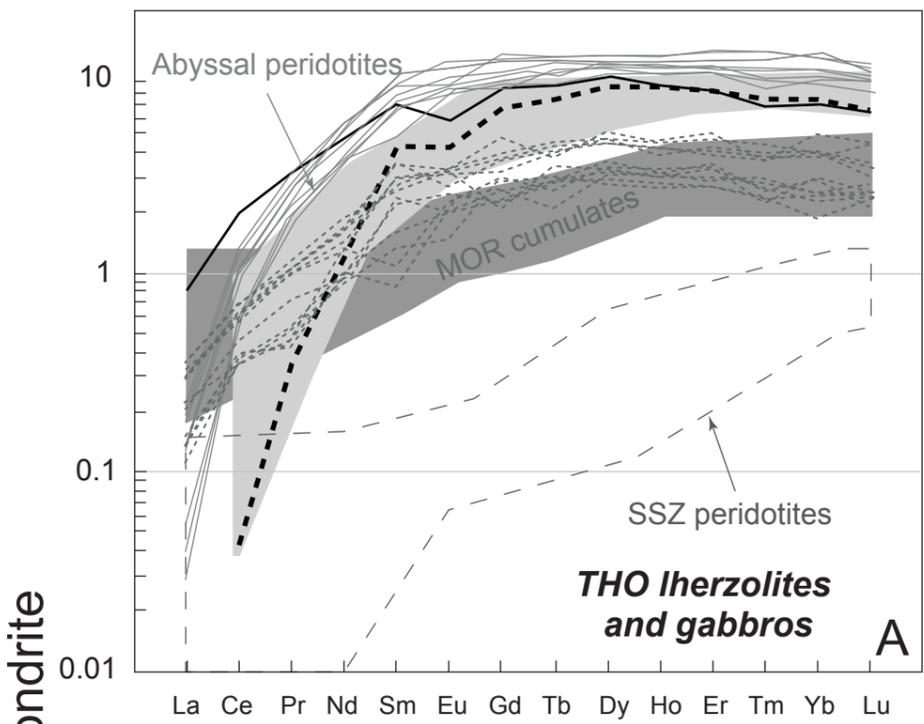


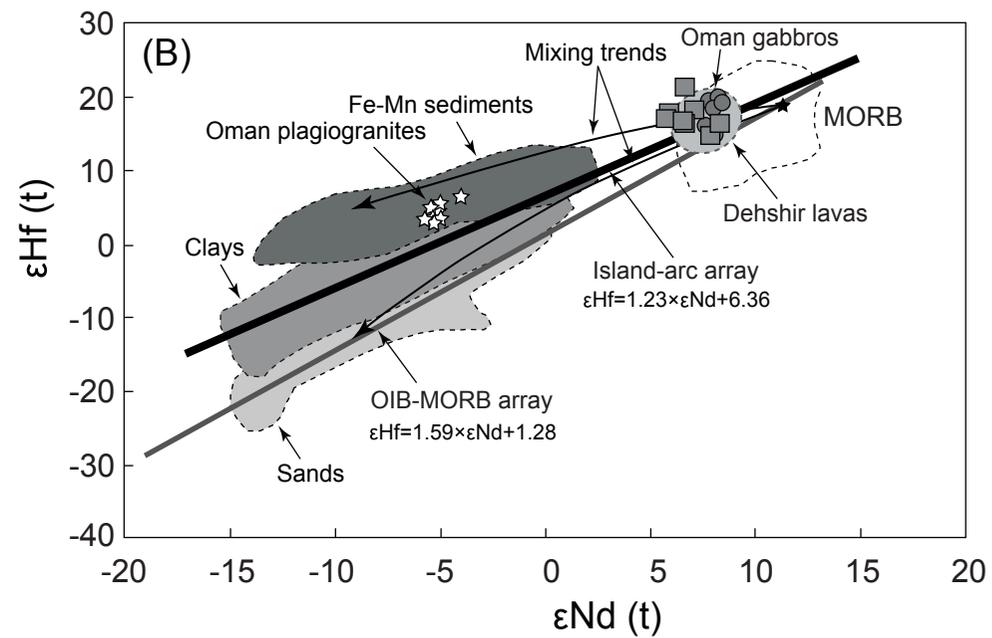
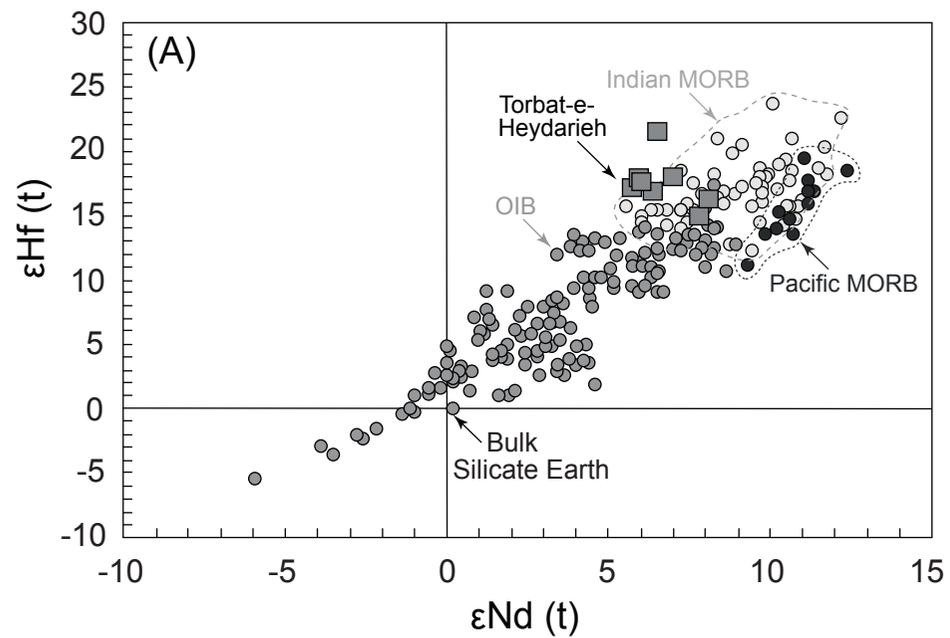


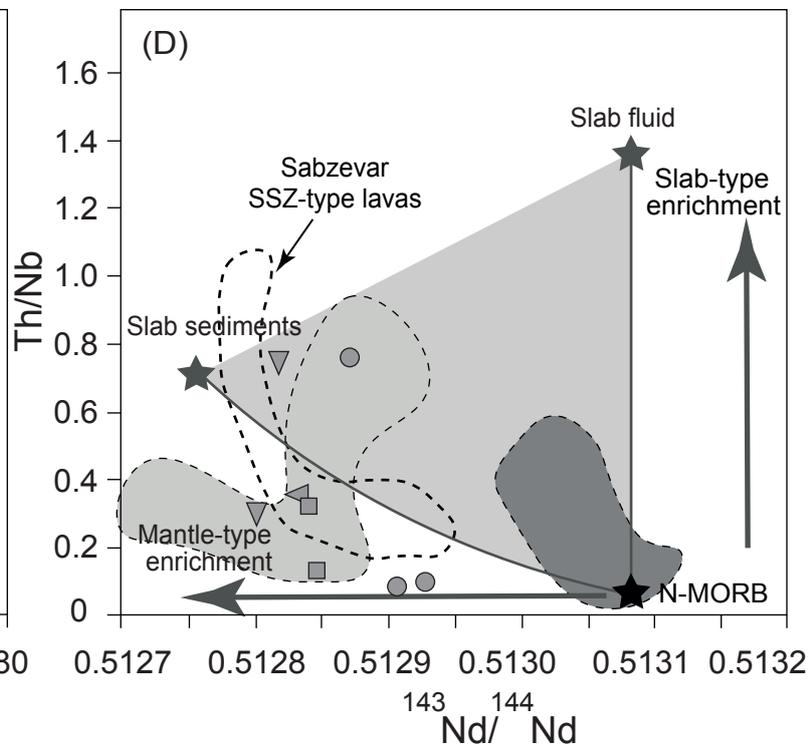
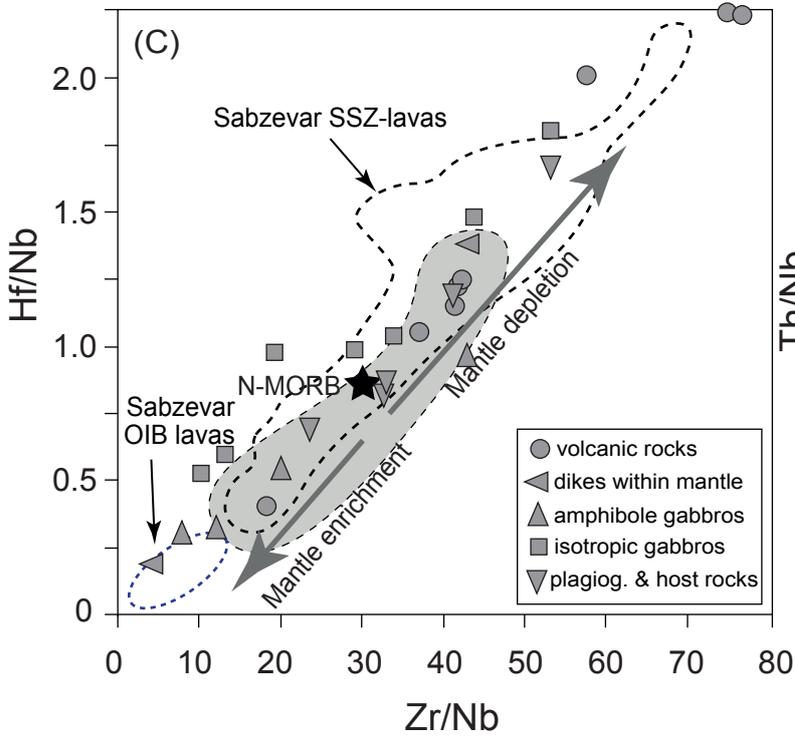
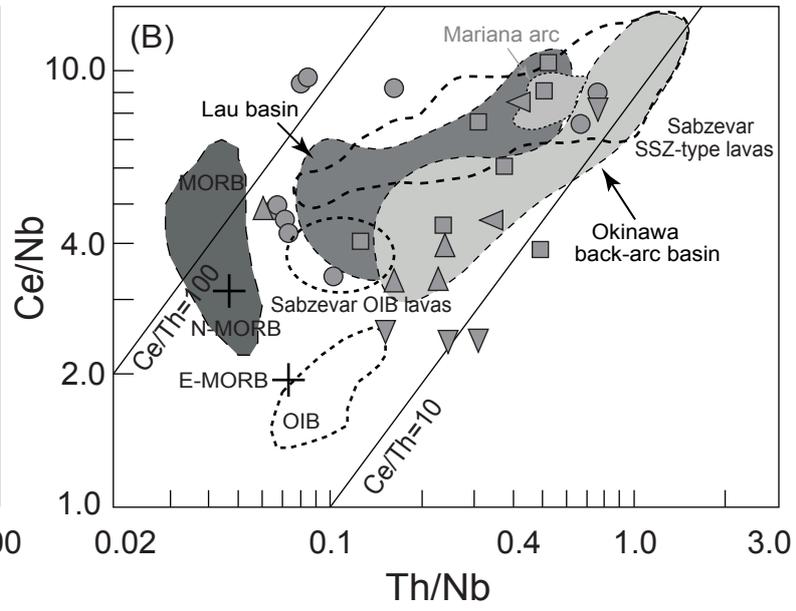
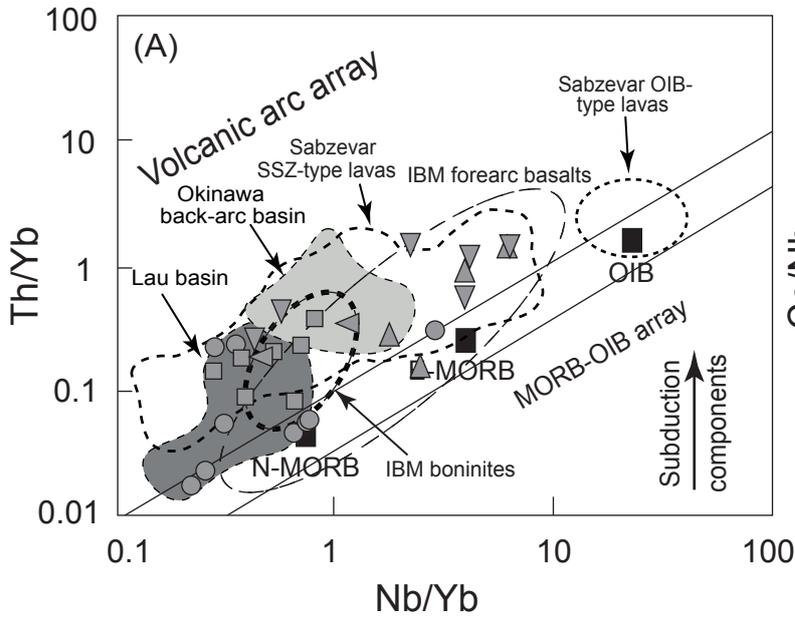






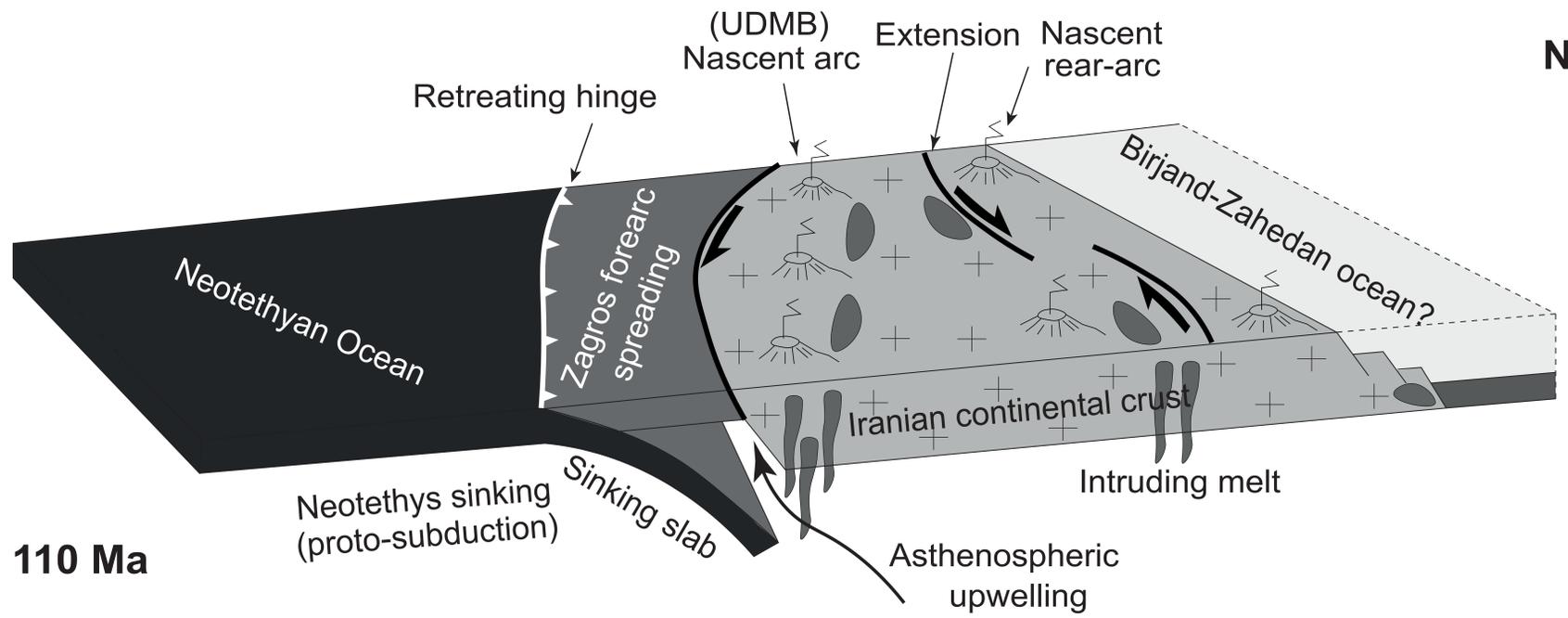




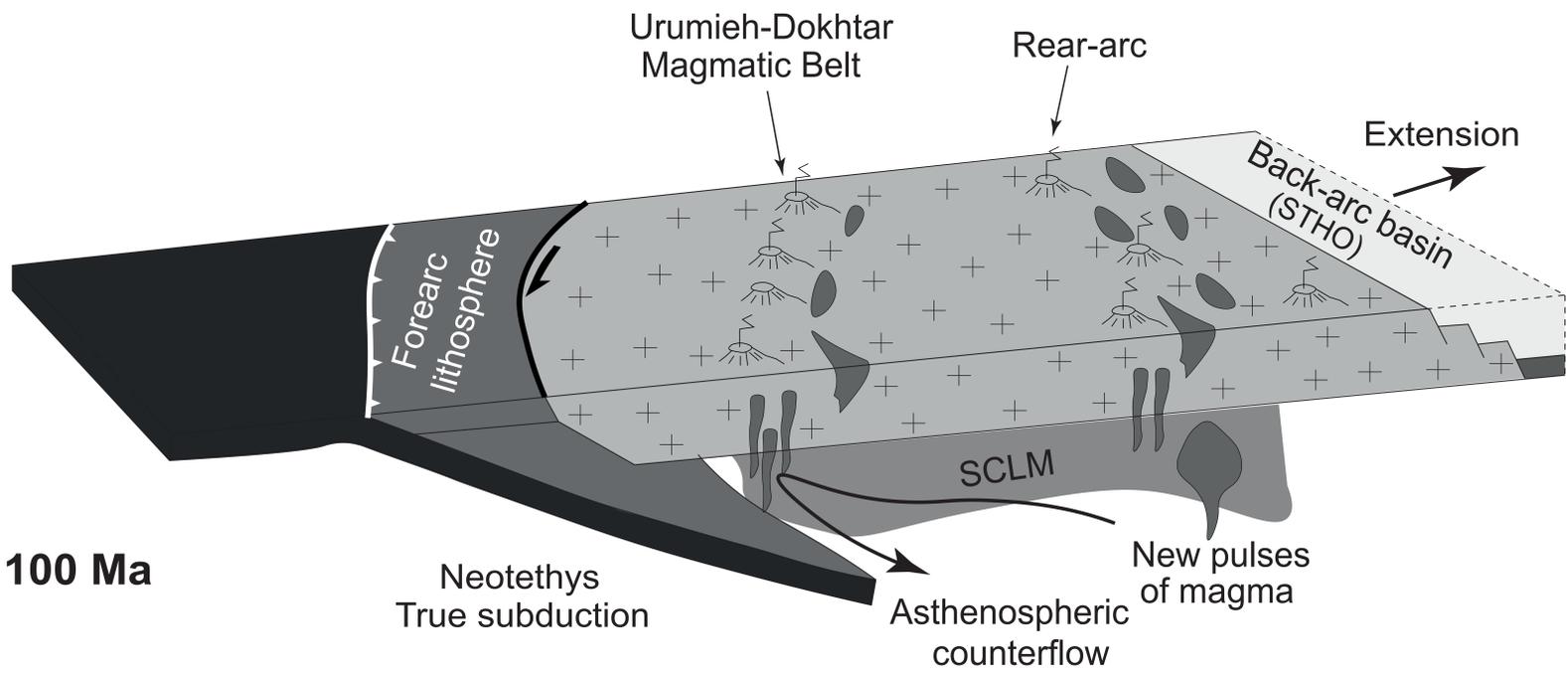


SW

NE



A) 110 Ma



B) 100 Ma